

# Application of relativistic density functionals in the modeling of nuclear weak-interaction processes

---

Marketin, Tomislav

Doctoral thesis / Disertacija

2010

Degree Grantor / Ustanova koja je dodijelila akademski / stručni stupanj: **University of Zagreb, Faculty of Science / Sveučilište u Zagrebu, Prirodoslovno-matematički fakultet**

Permanent link / Trajna poveznica: <https://um.nsk.hr/um:nbn:hr:217:658125>

Rights / Prava: [In copyright](#) / [Zaštićeno autorskim pravom.](#)

Download date / Datum preuzimanja: **2024-07-17**



Repository / Repozitorij:

[Repository of the Faculty of Science - University of Zagreb](#)



UNIVERSITY OF ZAGREB  
FACULTY OF SCIENCE  
DEPARTMENT OF PHYSICS

Tomislav Marketin

**Application of relativistic density functionals  
in the modeling of nuclear weak-interaction  
processes**

Doctoral Thesis submitted to the Department of Physics  
Faculty of Science, University of Zagreb  
for the academic degree of  
Doctor of Natural Sciences (Physics)

Zagreb, 2010.



SVEUČILIŠTE U ZAGREBU  
PRIRODOSLOVNO-MATEMATIČKI FAKULTET  
FIZIČKI ODSJEK

Tomislav Marketin

**Primjena relativističkih funkcionala gustoće u  
procesima slabog međudjelovanja u atomskim  
jezgrama**

Doktorska disertacija  
predložena Fizičkom odsjeku  
Prirodoslovno-matematičkog fakulteta Sveučilišta u Zagrebu  
radi stjecanja akademskog stupnja  
doktora prirodnih znanosti fizike

Zagreb, 2010.



University of Zagreb  
Faculty of Science  
Department of Physics

Doctoral Thesis

## **Application of relativistic density functionals in the modeling of nuclear weak-interaction processes**

TOMISLAV MARKETIN

Faculty of Science, University of Zagreb

Relativistic density functionals are employed in a study of weak-interaction processes in atomic nuclei. The approach is based on the relativistic Hartree-Bogoliubov (RHB) model that is used to compute the self-consistent nuclear ground state, and collective excited states are modeled with the relativistic quasiparticle random phase approximation (RQRPA). The focus of the study is the calculation of  $\beta$ -decay half-lives of neutron-rich nuclei that are predicted to play a role in r-process nucleosynthesis, and their comparison to available experimental values. The model is also applied to the description of charged lepton capture and neutrino capture. This study provides a microscopic description of weak-interaction processes in nuclei, based on modern nuclear energy density functional concepts, and results contribute to a better understanding of the origin of elements heavier than iron.

(105 pages, 101 references, original in English)

Supervisor: Prof. dr. sc. D. Vretenar

Reviewers: Prof. dr. sc. N. Paar  
Prof. dr. sc. D. Vretenar  
Dr. sc. S. Szilner, senior research associate  
Prof. dr. sc. P. Ring  
Prof. dr. sc. M. Milin

Thesis accepted: 19. October 2010.



# TEMELJNA DOKUMENTACIJSKA KARTICA

Sveučilište u Zagrebu  
Prirodoslovno-matematički fakultet  
Fizički odsjek

Doktorska disertacija

## **Primjena relativističkih funkcionala gustoće u procesima slabog međudjelovanja u atomskim jezgrama**

TOMISLAV MARKETIN

Prirodoslovno-matematički fakultet, Sveučilište u Zagrebu

Relativistički funkcionali gustoće upotrijebljeni su za proučavanje procesa slabog međudjelovanja u atomskim jezgrama. Pristup se temelji na relativističkom Hartree-Bogoljubov (RHB) modelu koji daje samosuglasno osnovno stanje jezgre, a kolektivna pobuđenja modelirana su sa relativističkom kvazičestičnom aproksimacijom slučajnih faza (RQRPA). Središnja tema rada je proračun vremena polučivota pri  $\beta$  raspadu jezgara bogatih neutronima za koje je predviđeno da sudjeluju u r-procesu nukleosinteze, te njihova usporedba sa dostupnim eksperimentalnim vrijednostima. Model je također primjenjen na opis uhvata nabijenog leptona i uhvata neutrina. Ova radnja predstavlja mikroskopski opis procesa slabog međudjelovanja u jezgrama, temeljen na modernim konceptima funkcionala gustoće energije, a rezultati doprinose boljem razumijevanju porijekla elemenata težih od željeza.

(105 stranica, 101 literaturni navod, jezik izvornika engleski)

Mentor: Prof. dr. sc. D. Vretenar

Ocjenjivači: Prof. dr. sc. N. Paar  
Prof. dr. sc. D. Vretenar  
Dr. sc. S. Szilner, viši znanstveni suradnik  
Prof. dr. sc. P. Ring  
Prof. dr. sc. M. Milin

Radnja prihvaćena: 19. listopada 2010.





# Acknowledgements

This thesis was made under the supervision of Prof. Dr. Dario Vretenar. His insight, comments and directions, concerning both the research and writing, have proven to be of great value. For all of them, I am grateful.

I have also had the pleasure of working with Prof. Dr. Peter Ring during my stay at the Technische Universität München. His experience and hospitality have made my visit enjoyable and stimulating. Also, I need to acknowledge the support of the Alexander von Humboldt-Stiftung during my stay in Germany.

Dr. Tamara Nikšić and Prof. Dr. Nils Paar have indebted me with their patience and understanding during the entire process. Their advice and thoughts have been invaluable. I would also like to thank all my colleagues and friends for their support during these years.

Finally, I would like to thank my family and Iva for everything.



# Contents

|  |           |
|--|-----------|
| <b>Acknowledgements</b>  | <b>9</b>  |
| <b>Contents</b>  | <b>11</b> |
| <b>1 Introduction</b>  | <b>13</b> |
| <b>2 Relativistic mean-field theory</b>  | <b>19</b> |
| 2.1 Relativistic Lagrangian density . . . . .                                  | 20        |
| 2.2 Covariant density functional theory . . . . .                              | 24        |
| 2.3 Stationary solutions of the equations of motion . . . . .                  | 26        |
| 2.4 Relativistic Hartree-Bogoliubov model . . . . .                            | 29        |
| 2.5 Effective mass in relativistic models . . . . .                            | 34        |
| 2.5.1 Inclusion of a tensor term in $\omega$ -meson-nucleon coupling .         | 35        |
| 2.5.2 Inclusion of momentum dependent terms in nucleon self-energies . . . . . | 37        |
| <b>3 Relativistic quasiparticle random phase approximation</b>                 | <b>43</b> |
| 3.1 Relativistic random phase approximation . . . . .                          | 44        |
| 3.2 Relativistic quasiparticle random phase approximation . . . . .            | 47        |
| 3.3 Proton-neutron RQRPA . . . . .   | 50        |
| 3.4 Treatment of allowed transitions in neutron-rich nuclei . . . . .          | 53        |
| 3.5 Half-lives of neutron rich nuclei around closed shells . . . . .           | 55        |
| 3.5.1 $N \approx 50$ region . . . . .  | 56        |
| 3.5.2 $N \approx 82$ region . . . . .  | 60        |
| <b>4 Nuclear semi-leptonic weak-interaction processes</b>                      | <b>67</b> |
| 4.1 Formalism of weak interaction processes . . . . .                          | 68        |
| 4.2 Multipole analysis of the leptonic matrix element . . . . .                | 71        |
| 4.3 Muon capture . . . . .   | 75        |
| 4.4 Neutrino capture . . . . .   | 81        |
| <b>5 Conclusion</b>  | <b>93</b> |
| <b>A Relativistic model with momentum-dependent self-energies</b>              | <b>97</b> |

|                                |            |
|--------------------------------|------------|
| <b>B Finite element method</b> | <b>101</b> |
| <b>Bibliography</b>            | <b>103</b> |
| <b>List of Figures</b>         | <b>109</b> |
| <b>List of Tables</b>          | <b>113</b> |
| <b>Curriculum Vitae</b>        | <b>115</b> |

# Chapter 1

## Introduction

The topic of semi-leptonic interactions in nuclei is of interest for several reasons. Most of the fundamental tests of weak-interaction theory have involved nuclei, and if nuclei are to serve as laboratories with which to conduct experiments on weak interactions, it is essential that the nuclear physics of these processes be well understood. Knowing the nature of weak-interaction processes, they can be used for testing current theoretical description of nuclear phenomena. Following the conserved-vector-current (CVC) theory, weak-interaction matrix elements coming from the vector current are identical to those measured in electron scattering. It follows that weak probes can complement electromagnetic probes in examining nuclear structure. However, weak-interaction processes are even more informative as they are also sensitive to the axial-vector, as well as vector current, providing a better experimental tool. Finally, weak interactions play a critical role in astrophysical applications such as r-process nucleosynthesis, core-collapse supernova explosions and others.

The weak-interaction coupling constant is small enough to allow for a perturbative treatment of problems, reducing the calculations to a nuclear structure problem. However, inability to accurately treat nuclear systems has introduced large uncertainties in theoretical examinations of weak-interaction processes. Nevertheless, a lot of progress has been made in this field recently based on a self-consistent mean-field approach leading to an improved ground-state description of nuclei, both close to and removed from the valley of stability [1]. Building on these developments, models describing collective motion of nuclei have been developed, applicable to exotic modes of excitation in nuclei far from stability [2]. Continuing this line of research, the focus of this thesis is on application of relativistic Hartree-Bogoliubov + proton-neutron relativistic quasiparticle random phase approximation framework on semi-leptonic weak-interaction processes in neutron-rich nuclei:  $\beta$ -decay, muon capture and neutrino-nucleus reactions.

Semi-leptonic weak-interaction processes are usually considered in the wider context of nuclear astrophysics [3]. Within this field of research, one of the

most active topics is the question of nucleosynthesis of heavy elements during the r-process, a quantitative description of which requires precise data on involved nuclei, including but not limited to masses,  $\beta$ -decay half-lives, energies of excited states, beta delayed neutron emission rates,  $(n, \gamma)$  reaction rates, etc. for thousands of nuclei, most of which are experimentally unreachable. Therefore, astrophysical models must rely on nuclear structure and reaction theory to provide all relevant input which can be used to determine astrophysical conditions in which creation of neutron-rich stable isotopes takes place. However, models that provide most accurate description of stable nuclei do not necessarily extrapolate well to neutron-rich regions. Unexpectedly large neutron skins appear in medium-heavy and heavier nuclei where additional neutrons are weakly bound and neutron density becomes extended in space beyond the proton density. In light nuclei this effect is brought to its extreme with halo nuclei. Another unique feature of neutron-rich regions is the reforming of shell structure with changed shell closures. In stable nuclei magic numbers  $N, Z = 8, 20, 28, 50, 82, 126$  are well known and explained, but with high neutron to proton number ratios shell closures change, significantly influencing transition properties. Nuclear structure models aiming to provide astrophysical models with relevant input data must be able to simultaneously describe both stable and unstable nuclei within a universal theoretical framework.

Models based on the shell model are known to be very precise. Using realistic interactions and including as many correlations as possible they provide accurate results and can serve as a benchmark for all other models. Very large configuration space places computational limitations and restricts application to lightest nuclei only. Significant research has been done with the aim of overcoming these obstacles, resulting with Monte Carlo techniques, various ways of reducing the configuration space without eliminating important correlations, and methods of including short range correlations directly into operators. However, applications to heavy nuclei are still impossible and mean-field theory has been developed to systematically treat all nuclei. Best known nonrelativistic phenomenological effective interactions developed over the last several decades are the Skyrme and Gogny energy functionals.

Even though nonrelativistic models provide a good description of nuclei with reasonable accuracy, natural description of nuclear systems is relativistic. Nuclear potential is a result of cancellation of two strong potentials, the attractive scalar potential and the repulsive vector potential. Strong spin-orbit coupling is described by the spin-orbit potential equal to the sum of the scalar and vector potentials. Therefore, relativistic effects are important even at low energies. Relativistic mean-field models assume that nuclear interaction is based on the exchange of mesons which build the single-particle potentials that nucleons move in. The source of mesons is the nucleon density, coupling nucleon and meson wave equations and making the system self-consistent. To obtain

a quantitative description of finite nuclei, the basic model is extended by including nonlinear meson self-interaction terms, however further improvement of such models is difficult due to new parameters, as available experimental data only allows unique determination of a limited number of parameters. Modern versions of relativistic mean-field models include density-dependence of meson-nucleon coupling constants as a more flexible replacement of nonlinear terms. Properties of nuclear matter and finite nuclei, hypernuclei and neutron stars have all been successfully described within the relativistic mean-field (RMF) theory. Relativistic interactions adjusted to properties of nuclear matter and bulk properties of finite nuclei will be used to describe semi-leptonic weak-interaction processes in neutron-rich nuclei. Pairing correlations will be treated in the relativistic Hartree-Bogoliubov (RHB) framework which is a relativistic extension of the conventional Hartree-Bogoliubov models and provides a unified description of mean-field and pairing correlations.

A known characteristic of relativistic models is a relatively low effective nucleon mass, which is connected to low density of states around the Fermi surface. A measure of non-locality in space and time in nonrelativistic models, effective mass leads to momentum and energy dependence of the single-particle potential. The standard density-dependent framework will be extended in two separate attempts in order to improve the description of density of states around the Fermi level. In the first attempt, tensor coupling of the  $\omega$ -meson will be introduced to preserve good spin-orbit properties while increasing effective nucleon mass. In the other approach, momentum-dependent terms will be directly included in the Lagrangian density leading to energy-dependent scalar and vector self-energies in the stationary solutions of nuclear equations of motion. With both approaches the effective mass will be enhanced close to nonrelativistic values, improving the description of the ground-state single-particle structure of neutron-rich nuclei.

These two models will be used to study  $\beta$ -decay rates of neutron-rich nuclei, for isotopic chains around closed proton shells at  $Z = 28$  and  $Z = 50$ . Even with relatively large Q-values in these mass regions, momentum transfer in  $\beta$ -decay is small allowing for the use of the long-wavelength approximation. Gamow-Teller strength will be calculated using the proton-neutron relativistic quasiparticle random phase approximation (pn-RQRPA) with the same interactions as was used at the mean-field level. When considering  $\beta$ -decay, the important part of the spectrum is at low energies below the Q-value where strength is particularly sensitive to single-particle structure of the nucleus. Of critical importance for a quantitative description, models commonly rely on experimental nuclear masses or highly specialized mass models like microscopic-macroscopic finite range droplet model (FRDM), extended Thomas-Fermi with Strutinsky integral (ETFSI) approach or Duflo-Zuker mass table inspired by shell model results, to obtain Q-values. In this thesis, the Q-value is approximated using proton and neutron chemical potentials derived from a Taylor



expansion of the binding energy of the daughter nucleus, eliminating the need for any external input.  $\beta$ -decay half-lives are obtained by integrating the volume of phase space available to outgoing leptons and compared to experimental values. Improved level density around the Fermi level has proved to be crucial for improving predicted half-lives, but additional proton-neutron residual interaction had to be introduced to reproduce experimental values.

Even though  $\beta$ -decay is dominated by allowed Gamow-Teller transitions, there has been a lot of speculation in recent years on the importance of forbidden transitions for precise predictions of half-lives and the effect on nucleosynthesis. Their contribution may be significant in nuclei near closed shells, and their effect in nuclei with a large neutron excess and in nuclei around  $N = 126$  is yet unknown [4]. Additionally, other weak-interaction processes have very large momentum transfer and cannot be treated within the long-wavelength approximation. A more general framework will be implemented at the pn-RQRPA level where all multipole transitions are treated equally, making no approximations and having full momentum transfer dependence included in transition operators [5]. Within this formalism, muon capture and neutrino-nucleus reactions will be examined.

Muon capture on stable nuclei has been studied in detail since many years, both experimentally and theoretically [6]. In this process the momentum transfer is of the order of the muon mass and, therefore, the calculation of total muon capture rates presents an excellent test of models that are also used in studies of low-energy neutrino-nucleus reactions. Neutrino-nucleus reactions at low energies play an important role in many phenomena in nuclear and particle physics, as well as astrophysics. These reactions present extremely subtle physical processes, not only because they involve the weak interaction but also because they are very sensitive to the structure of nuclear ground states and excitations, i.e., to the solution of the nuclear many-body problem that includes the strong and electromagnetic interactions. The use of microscopic nuclear structure models in a consistent theoretical framework is therefore essential for a quantitative description of neutrino-nucleus reactions [7]. Detailed predictions of neutrino-nucleus cross sections are crucial for the interpretation of neutrino experiments and the detection of neutrinos produced in supernova explosions. Neutrino-nucleus reactions that occur in a type II supernova could also contribute to the nucleosynthesis [3], but more data on cross sections are necessary for a more complete understanding of this process, as well as the supernova dynamics.

Chapter 2 will give a short review of the relativistic mean-field theory used to obtain the ground-state of a spherical, even-even nucleus. Two extensions of the model aimed at increasing nucleon effective mass will be presented in Section 2.5. Chapter 3 will provide a description of a fully self-consistent proton-neutron relativistic quasiparticle RPA. Details of  $\beta$ -decay half-lives will also be given, and comparison with experimental values provided in Sections 3.4

and 3.5, respectively. Chapter 4 will cover the necessary formalism of the weak interaction, focusing on aspects of this particular implementation. Application of the theoretical framework to total muon capture rates and neutrino-nucleus reaction cross sections will be presented and comparison with experiment and other theoretical studies given. Finally, a short summary with possible future applications is given in Chapter 5.



# Chapter 2

## Relativistic mean-field theory

Modern nuclear structure theory has evolved from macroscopic and microscopic studies of phenomena in stable nuclei towards regions of exotic, short-lived nuclei far from the valley of stability, and nuclear astrophysics applications. The principal challenge is to build a consistent microscopic theoretical framework that will provide a unified description of bulk properties, nuclear excitations and reactions. Self-consistent mean-field models based on the relativistic mean-field theory (RMF) [8] have been very successfully employed in analyses of a variety of nuclear structure phenomena, not only in nuclei along the valley of  $\beta$ -stability, but also in exotic nuclei with extreme isospin values and close to the particle drip-lines. RMF-based models have reached a level of sophistication and accuracy comparable to the non-relativistic Hartree-Fock-Bogoliubov framework based on Skyrme and Gogny effective interactions [1].

In addition to the self-consistent mean-field single-nucleon potential, the inclusion of pairing correlations is essential for a quantitative description of structure phenomena in open-shell spherical and deformed nuclei. In weakly bound systems far from stability, in particular, the Fermi surface for one type of nucleons is found close to the particle continuum. The single-nucleon separation energies become comparable to the pairing gaps, and this results in the lowest particle hole (ph) and particle particle (pp) modes being embedded in the continuum. A unified and self-consistent treatment of both the mean-field and pairing correlations becomes necessary, and the coupling between bound and continuum states has to be taken into account explicitly. The Hartree-Fock-Bogoliubov (HFB) theory [9] provides a unified description of ph- and pp-correlations in nuclei and, when the self-consistent HFB equations are formulated in coordinate space, allows for a treatment of continuum effects in the presence of pairing.

To be able to reproduce the data on  $\beta$ -decay half-lives, the description of single-particle energies around the Fermi surface must be improved. A simple approach to increase the density of single-nucleon states without going beyond mean-field level will be taken. An increase of the effective mass necessitates

a reduction of the vector self-energy. However, to retain the empirical value of the nuclear matter binding energy, the scalar self-energy should be reduced correspondingly. A serious problem arises because such an effective interaction would systematically underestimate the spin-orbit splittings in finite nuclei. A solution to this problem has been known for a long time, namely the tensor coupling of the  $\omega$ -meson to the nucleon. This interaction enhances the effective spin-orbit potential in finite nuclei but is not included in the most commonly used relativistic mean-field models.

Another solution is provided by the recently introduced relativistic mean-field model with momentum-dependent nucleon self-energies [10]. In this model the standard effective Lagrangian with density-dependent meson-nucleon coupling vertices is extended by including a particular form of the couplings between the isoscalar meson fields and the derivatives of the nucleon fields. This leads to a linear momentum dependence of the scalar and vector self-energies in the Dirac equation for the in-medium nucleon. Even though the extension of the standard mean-field framework is phenomenological, it is nevertheless based on Dirac-Brueckner calculations of in-medium nucleon self-energies, and consistent with the relativistic optical potential in nuclear matter, extracted from elastic proton-nucleus scattering data. In the extended model it is possible to increase the effective nucleon mass, while keeping a small Dirac mass which is required to reproduce the empirical strength of the effective spin-orbit potential.

## 2.1 Relativistic Lagrangian density

In the standard representation of quantum hadrodynamics the nucleus is described as a system of Dirac nucleons coupled to the exchange mesons and the electromagnetic field through an effective Lagrangian. The isoscalar scalar  $\sigma$ -meson, the isoscalar vector  $\omega$ -meson, and the isovector vector  $\rho$ -meson build the minimal set of meson fields that together with the electromagnetic field is necessary for a quantitative description of bulk and single-particle nuclear properties [8, 11]. The model is defined by the Lagrangian density

$$\mathcal{L} = \mathcal{L}_N + \mathcal{L}_M + \mathcal{L}_{int}. \quad (2.1)$$

$\mathcal{L}_N$  denotes the Lagrangian of the free nucleon

$$\mathcal{L}_N = \bar{\psi} (i\gamma^\mu \partial_\mu - m) \psi, \quad (2.2)$$

where  $m$  is the bare nucleon mass and  $\psi$  denotes the Dirac spinor.  $\mathcal{L}_M$  is the Lagrangian of the free meson fields and the electromagnetic field

$$\begin{aligned} \mathcal{L}_M = & \frac{1}{2} (\partial_\mu \sigma \partial^\mu \sigma - m_\sigma^2 \sigma^2) - \frac{1}{2} \left( \frac{1}{2} \Omega_{\mu\nu} \Omega^{\mu\nu} - m_\omega^2 \omega_\mu \omega^\mu \right) \\ & - \frac{1}{2} \left( \frac{1}{2} \vec{R}_{\mu\nu} \vec{R}^{\mu\nu} - m_\rho^2 \vec{\rho}_\mu \vec{\rho}^\mu \right) - \frac{1}{4} F_{\mu\nu} F^{\mu\nu}, \end{aligned} \quad (2.3)$$

with the corresponding masses  $m_\sigma$ ,  $m_\omega$ ,  $m_\rho$  and  $\Omega_{\mu\nu}$ ,  $\vec{R}_{\mu\nu}$ ,  $F_{\mu\nu}$  are field tensors

$$\Omega_{\mu\nu} = \partial_\mu\omega_\nu - \partial_\nu\omega_\mu \quad (2.4)$$

$$\vec{R}_{\mu\nu} = \partial_\mu\vec{\rho}_\nu - \partial_\nu\vec{\rho}_\mu \quad (2.5)$$

$$F_{\mu\nu} = \partial_\mu A_\nu - \partial_\nu A_\mu, \quad (2.6)$$

where arrows denote isovectors. Boldface symbols will be used to denote vectors in coordinate space. The minimal set of interaction terms is contained in  $\mathcal{L}_{int}$

$$\mathcal{L}_{int} = -g_\sigma\bar{\psi}\sigma\psi - g_\omega\bar{\psi}\gamma_\mu\omega^\mu\psi - g_\rho\bar{\psi}\gamma_\mu\vec{\rho}^\mu\vec{\tau}\psi - e\bar{\psi}\gamma_\mu A^\mu\frac{1-\tau_3}{2}\psi. \quad (2.7)$$

with coupling constants  $g_\sigma$ ,  $g_\omega$ ,  $g_\rho$  and  $e$ . The phenomenological  $\sigma$ -meson approximates a large attractive scalar field that results from complicated microscopic processes, such as uncorrelated and correlated two-pion exchange. The  $\omega$ -meson describes the short-range repulsion between the nucleons, and the  $\rho$ -meson carries the isospin quantum number. The latter is required by the large empirical asymmetry potential in finite nuclear systems. Because of parity conservation there is no direct contribution from the pion field. The self-consistent RMF approach represents a particular realization of the relativistic Kohn-Sham density functional theory [12], in which one attempts to effectively include in the nuclear energy density functional effects which go beyond the Hartree approximation (Fock terms, short-range correlations, vacuum-polarization effects). The many-body correlations of the energy density functional can be represented by a medium dependence of the corresponding effective nuclear interaction. An effective density dependence can be included, for instance, through meson self-interaction terms. Over the years a number of non-linear meson-exchange interactions have been adjusted to the nuclear matter equation of state and bulk properties of a set of spherical closed-shell nuclei, and applied in the description of nuclear properties along the  $\beta$ -stability line. One of the most successful phenomenological interactions of this type is the non-linear parameter set NL3 [13], which has been employed in many studies of ground-state properties and collective excitations both in stable nuclei and in exotic systems far from the line of  $\beta$ -stability.

Another class of medium-dependent effective interactions is characterized by an explicit baryon-density dependence of the meson-nucleon vertices. Such an approach retains the basic structure of the relativistic mean-field framework, but can be more directly related to the underlying microscopic description of nuclear interactions. The functional form of the meson-nucleon vertices can be deduced from in-medium Dirac-Brueckner interactions, obtained from realistic free-space NN interactions, or a phenomenological approach can be adopted, with the density dependence for the  $\sigma$ ,  $\omega$  and  $\rho$  meson-nucleon couplings adjusted to properties of nuclear matter and a set of spherical nuclei. The former

represents an *ab-initio* description of nuclear matter and finite nuclei, and the corresponding density-dependent relativistic mean-field model has also been applied to asymmetric nuclear matter and exotic nuclei [14]. In the latter approach very accurate phenomenological density-dependent relativistic effective interactions have recently been adjusted [15, 16, 17], and employed in analyses of both bulk nuclear properties and collective excitations. A number of recent studies have shown that, in comparison with non-linear meson self-interactions, relativistic models with an explicit density dependence of the meson-nucleon couplings provide an improved description of asymmetric nuclear matter, neutron matter and nuclei far from stability.

The single-nucleon Dirac equation is derived by variation of Lagrangian (2.1) with respect to  $\bar{\psi}$

$$[\gamma^\mu (i\partial_\mu - \Sigma_\mu - \Sigma_\mu^R) - (m + \Sigma)] \psi = 0 \quad (2.8)$$

With the nucleon self-energies defined by the following relations:

$$\Sigma = g_\sigma \sigma, \quad (2.9)$$

$$\Sigma_\mu = g_\omega \omega_\mu + g_\rho \vec{\tau} \cdot \vec{\rho}_\mu + e \frac{1 - \tau_3}{2} A_\mu. \quad (2.10)$$

The density dependence of the vertex functions  $g_\sigma$ ,  $g_\omega$  and  $g_\rho$  produces the *rearrangement* contribution  $\Sigma_\mu^R$  to the vector self-energy

$$\Sigma_\mu^R = \frac{j_\mu}{\rho_v} \left( \frac{\partial g_\omega}{\partial \rho_v} \bar{\psi} \gamma^\nu \psi \omega_\nu + \frac{\partial g_\rho}{\partial \rho_v} \bar{\psi} \gamma^\nu \vec{\tau} \psi \cdot \vec{\rho}_\nu + \frac{\partial g_\sigma}{\partial \rho_v} \bar{\psi} \psi \sigma \right). \quad (2.11)$$

The inclusion of the rearrangement self-energies is essential for the energy-momentum conservation and the thermodynamical consistency of the model (the equality of the pressure obtained from the thermodynamical definition and from the energy-momentum tensor) [15].

The density-dependence of the meson-nucleon couplings can be parametrized in a phenomenological way by the following functionals [15, 16]. The coupling of the  $\sigma$ -meson and  $\omega$ -meson to the nucleon field reads

$$g_i(\rho) = g_i(\rho_{sat}) f_i(x) \quad \text{za} \quad i = \sigma, \omega, \quad (2.12)$$

where

$$f_i(x) = a_i \frac{1 + b_i (x + d_i)^2}{1 + c_i (x + d_i)^2} \quad x = \frac{\rho}{\rho_{sat}}. \quad (2.13)$$

is a function of  $x = \rho/\rho_{sat}$ , and  $\rho_{sat}$  denotes the baryon density at saturation in symmetric nuclear matter. The eight real parameters in Eq. (2.13) are not independent. The five constraints

- $f_i(1) = 1$

- $f''_\sigma(1) = f''_\omega(1)$
- $f''_i(0) = 0$

reduce the number of independent parameters to three. Three additional parameters in the isoscalar channel are  $g_\sigma(\rho_{sat})$ ,  $g_\omega(\rho_{sat})$  and  $m_\sigma$  - the mass of the phenomenological  $\sigma$ -meson. For the  $\rho$ -meson coupling the functional form of the density dependence is suggested by Dirac-Brueckner calculations of asymmetric nuclear matter [18]

$$g_\rho(\rho) = g_\rho(\rho_{sat})e^{-a_\rho(x-1)}. \quad (2.14)$$

The isovector channel is parametrized by  $g_\rho(\rho_{sat})$  and  $a_\rho$ . For the masses of the  $\omega$  and  $\rho$  mesons the free values are used:  $m_\omega = 783$  MeV and  $m_\rho = 763$  MeV.

The eight independent parameters, seven coupling parameters and the mass of the  $\sigma$ -meson, are adjusted to reproduce properties of symmetric and asymmetric nuclear matter, binding energies, charge radii and neutron radii of spherical nuclei. In particular, the density-dependent meson-exchange effective interaction DD-ME1 was constructed in Ref. [16]. The seven coupling parameters and the  $\sigma$ -meson mass have been simultaneously adjusted to properties of symmetric and asymmetric nuclear matter, and to ground-state properties (binding energies, charge radii and differences between neutron and proton radii) of 12 spherical nuclei. For the open shell nuclei pairing correlations have been treated in the BCS approximations with empirical pairing gaps (five-point formula).

Neglecting retardation effects for the meson fields, a self-consistent solution is obtained when the time-dependent mean-field potentials are calculated at each step in time from the solution of the stationary Klein-Gordon equations

$$(\square + m_\sigma^2) \sigma = -g_\sigma \langle \bar{\psi} \psi \rangle, \quad (2.15)$$

$$(\square + m_\omega^2) \omega^\mu = g_\omega \langle \bar{\psi} \gamma^\mu \psi \rangle, \quad (2.16)$$

$$(\square + m_\rho^2) \bar{\rho}^\mu = g_\rho \langle \bar{\psi} \gamma^\mu \vec{\tau} \psi \rangle, \quad (2.17)$$

$$\square A^\mu = e^2 \langle \bar{\psi} \gamma^\mu \frac{1 - \tau_3}{2} \psi \rangle. \quad (2.18)$$

For energies relevant for nuclear structure the stationary approximation is justified by the large meson masses. The corresponding meson exchange forces are of short range and therefore retardation effects can be neglected. In applications to nuclear matter and finite nuclei, the relativistic models are used in the *no-sea* approximation: the Dirac sea of states with negative energies does not contribute to the densities and currents. For a nucleus with  $A$  nucleons

$$\langle \bar{\psi} \Gamma_m \psi \rangle = \sum_{i=1}^A \bar{\psi}_i \Gamma_m \psi_i, \quad (2.19)$$



where the summation is performed only over occupied orbits in the Fermi sea of positive energy states.

The lowest order of the quantum field theory is the mean-field approximation: the meson-field operators are replaced by their expectation values in the nuclear ground state. The  $A$  nucleons, described by a Slater determinant  $|\Phi\rangle$  of single-particle spinors  $\psi_i$ , ( $i = 1, 2, \dots, A$ ), move independently in the classical meson fields. The sources of the meson fields are defined by the nucleon densities and currents. The ground state of a nucleus is described by the stationary self-consistent solution of the coupled system of Dirac and Klein-Gordon equations. The couplings of the meson fields to the nucleon are adjusted to reproduce the properties of nuclear matter and finite nuclei. Because of parity conservation there is no direct contribution from the pion field on the Hartree level. The pion has been included in the relativistic Hartree-Fock model [19]. Many effects that go beyond the mean-field level are apparently neglected in the RMF models: Fock terms, vacuum polarization effects and the short-range Brueckner-type correlations. The experimental data to which the meson-nucleon couplings are adjusted, however, contain all these effects and much more. It follows that effects beyond the mean-field level are implicitly included in the RMF approach by adjusting the model parameters to reproduce a selected empirical data set. Vacuum effects, chiral symmetry, nucleon substructure, exchange terms, long- and short-range correlation effects are, therefore, effectively included in this approach although neither of them can be assessed separately.

## 2.2 Covariant density functional theory

The mean-field approach to nuclear structure represents an approximate implementation of Kohn-Sham density functional theory (DFT) [12, 20, 21], which is successfully employed in the treatment of the quantum many-problem in atomic, molecular and condensed matter physics. At the basis of the DFT approach are energy density functionals of the ground-state density. In relativistic mean-field models, these become functionals of the ground-state scalar density and of the baryon currents.

The nonrelativistic DFT is based on the Hohenberg-Kohn theorem [20]. For a many-fermion system under consideration, the theorem states that the ground-state expectation value of any observable  $\hat{O}$  is a unique functional of the exact ground-state density  $\rho_0$ . As a second important statement, the theorem establishes the variational character of the energy functional  $E[\rho]$ . For any non-negative trial density that gives the correct number of fermions in the system, the true ground state energy  $E_0$  for the exact density  $\rho_0$  satisfies the relation

$$E[\rho_0] \leq E[\rho]. \quad (2.20)$$

Nuclear mean-field models approximate the energy functional, which includes all higher-order correlations, with powers and gradients of ground-state nucleon densities and currents. Within the covariant DFT theory, ground state  $|\Phi_0\rangle$  of a nucleus is uniquely determined by proton and neutron ground-state four-currents  $j_p^\mu$  and  $j_n^\mu$ , and ground-state scalar density  $\rho_s$ . Ground-state energy reads

$$E_0 [\rho_s, j_p^\mu, j_n^\mu] = \langle \Phi_0 | \hat{H} | \Psi_0 \rangle. \quad (2.21)$$

Currents and the density are

$$\rho_s = \sum_{q=p,n} \sum_i \bar{\psi}_{i,q}(\mathbf{r}) \psi_{i,q}(\mathbf{r}), \quad (2.22)$$

$$J_q^\mu = \sum_i \bar{\psi}_{i,q}(\mathbf{r}) \gamma^\mu \psi_{i,q}(\mathbf{r}), \quad (2.23)$$

where the sum is over all occupied positive energy states. The ground-state energy functional

$$E_0 = T_s + E_h + E_{xc} \quad (2.24)$$

consists of the single-particle kinetic term

$$T_s = \int d^3r \sum \psi_{i,q}^+(\mathbf{r}) (-i\boldsymbol{\alpha}\nabla + \beta m) \psi_{i,q}(\mathbf{r}), \quad (2.25)$$

the Hartree energy

$$\begin{aligned} E_h = & -\frac{1}{2} \int d^3r d^3r' D_\sigma(\mathbf{r}, \mathbf{r}') g_\sigma(\mathbf{r}) g_\sigma(\mathbf{r}') \rho_s(\mathbf{r}) \rho_s(\mathbf{r}') \\ & + \frac{1}{2} \int d^3r d^3r' D_\omega(\mathbf{r}, \mathbf{r}') g_\omega(\mathbf{r}) g_\omega(\mathbf{r}') (j_p^\mu(\mathbf{r}) + j_n^\mu(\mathbf{r})) (j_{\mu p}(\mathbf{r}') + j_{\mu n}(\mathbf{r}')) \\ & + \frac{1}{2} \int d^3r d^3r' D_\rho(\mathbf{r}, \mathbf{r}') g_\rho(\mathbf{r}) g_\rho(\mathbf{r}') (j_p^\mu(\mathbf{r}) - j_n^\mu(\mathbf{r})) (j_{\mu p}(\mathbf{r}') - j_{\mu n}(\mathbf{r}')) \\ & + \frac{1}{2} \int d^3r d^3r' e^2 D_C(\mathbf{r}, \mathbf{r}') j_p^\mu(\mathbf{r}) j_{\mu n}(\mathbf{r}'), \end{aligned} \quad (2.26)$$

and the exchange-correlation term. The latter is defined by (2.24), and minimization of the ground state energy  $E_0$  leads to Kohn-Sham equations

$$\left\{ -i\boldsymbol{\alpha}\nabla + \beta \left[ m + \Sigma_{s,h} + \Sigma_{s,xc} + \gamma_\mu \left( \Sigma_{q,h}^\mu + \Sigma_{q,R}^\mu + \Sigma_{q,xc}^\mu \right) \right] \right\} \psi_{i,q} = \epsilon_{i,q} \psi_{i,q}. \quad (2.27)$$

$\Sigma_{s,h}$  and  $\Sigma_{q,h}^\mu$  are the usual scalar and vector self-energies, and  $\Sigma_{q,R}^\mu$  is the rearrangement contribution. Local exchange-correlation potentials are defined as

$$E_{s,xc}(\mathbf{r}) = \frac{\delta}{\delta \rho_s(\mathbf{r})} E_{xc}, \quad (2.28)$$

$$E_{q,xc}^\mu(\mathbf{r}) = \frac{\delta}{\delta j_q^\mu(\mathbf{r})} E_{xc}. \quad (2.29)$$

## 2.3 Stationary solutions of the equations of motion

The ground state of the nucleus is obtained as a solution of the stationary equations of motion. In this case, the nucleon spinors are eigenvectors of the stationary Dirac equation, which yields the single-particle energies  $\epsilon_i$  as eigenvalues

$$[\boldsymbol{\alpha}(-i\nabla - \mathbf{V}(\mathbf{r})) + \beta m_D(\mathbf{r}) + V(\mathbf{r}) + \Sigma^R(\mathbf{r})] \psi_i(\mathbf{r}) = \epsilon_i \psi_i(\mathbf{r}). \quad (2.30)$$

where  $\mathbf{V}(\mathbf{r})$  is the space-like, and  $V(\mathbf{r})$  the time-like component of the vector self-energy.  $\Sigma^R$  is the rearrangement self-energy (2.11). The Dirac mass is defined by the scalar field

$$m_D(\mathbf{r}) = m + g_\sigma \sigma(\mathbf{r}), \quad (2.31)$$

with  $m$  being the bare nucleon mass. Due to charge conservation, only the neutral component of the isovector  $\rho$  meson contributes.

The equations can be further simplified by only considering systems with time-reversal invariance, such as even-even nuclei in the ground state. In that case there are no net currents, and the corresponding space-like components of the vector potential vanish. Final form of the Dirac equation reads

$$[-i\boldsymbol{\alpha}\nabla + \beta m_D(\mathbf{r}) + V(\mathbf{r}) + \Sigma^R(\mathbf{r})] \psi_i(\mathbf{r}) = \epsilon_i \psi_i(\mathbf{r}), \quad (2.32)$$

and is coupled with a system of Klein-Gordon equations for the mesons

$$(-\Delta + m_\sigma^2) \sigma(\mathbf{r}) = -g_\sigma \rho_s(\mathbf{r}), \quad (2.33)$$

$$(-\Delta + m_\omega^2) \omega^0(\mathbf{r}) = g_\omega \rho_v(\mathbf{r}), \quad (2.34)$$

$$(-\Delta + m_\rho^2) \rho_3^0(\mathbf{r}) = g_\rho \rho_{tv}(\mathbf{r}), \quad (2.35)$$

$$-\Delta A^0(\mathbf{r}) = e \rho_C(\mathbf{r}). \quad (2.36)$$

The meson equations can be solved analytically using the Green's functions method

$$\sigma(\mathbf{r}) = - \int g_\sigma (\rho_v(\mathbf{r}')) D_\sigma(\mathbf{r}, \mathbf{r}') \rho_s(\mathbf{r}') d^3 r', \quad (2.37)$$

$$\omega^0(\mathbf{r}) = - \int g_\omega (\rho_v(\mathbf{r}')) D_\omega(\mathbf{r}, \mathbf{r}') \rho_v(\mathbf{r}') d^3 r', \quad (2.38)$$

$$\rho_3^0(\mathbf{r}) = - \int g_\rho (\rho_v(\mathbf{r}')) D_\rho(\mathbf{r}, \mathbf{r}') \rho_{tv}(\mathbf{r}') d^3 r', \quad (2.39)$$

$$A^0(\mathbf{r}) = e \int D_C(\mathbf{r}, \mathbf{r}') \rho_C(\mathbf{r}') d^3 r' \quad (2.40)$$

with the meson propagators

$$D_\phi(\mathbf{r}, \mathbf{r}') = \frac{1}{4\pi} \frac{e^{-m_\phi |\mathbf{r} - \mathbf{r}'|}}{|\mathbf{r} - \mathbf{r}'|}, \quad (2.41)$$

and the photon propagator

$$D_C(\mathbf{r}, \mathbf{r}') = \frac{1}{4\pi} \frac{1}{|\mathbf{r} - \mathbf{r}'|}. \quad (2.42)$$

The set of coupled equations is solved iteratively. Starting from an initial guess of the scalar and vector potentials, densities

$$\rho_s(\mathbf{r}) = \sum_{i=1}^A \psi_i^\dagger(\mathbf{r}) \beta \psi_i(\mathbf{r}), \quad (2.43)$$

$$\rho_v(\mathbf{r}) = \sum_{i=1}^A \psi_i^\dagger(\mathbf{r}) \psi_i(\mathbf{r}), \quad (2.44)$$

$$\rho_{tv}(\mathbf{r}) = \sum_{i=1}^A \psi_i^\dagger(\mathbf{r}) \tau_3 \psi_i(\mathbf{r}), \quad (2.45)$$

$$\rho_C(\mathbf{r}) = \sum_{i=1}^A \psi_i^\dagger(\mathbf{r}) \frac{1 - \tau_3}{2} \psi_i(\mathbf{r}), \quad (2.46)$$

are calculated from nucleon wave functions, and are then used as sources in the Klein-Gordon equations. Meson fields are solutions of the Klein-Gordon equations, and enter the scalar and vector potentials in (2.32). Final solution is reached when the system achieves convergence.

Integrating the  $T^{00}$  component of the stress-energy tensor over the entire nucleus total energy of the system is obtained

$$E_{RMF} = \sum_{i=1}^A \int \psi_i^\dagger (-i\boldsymbol{\alpha}\nabla + \beta m) \psi_i d^3r + \frac{1}{2} \int (g_\sigma \rho_s \sigma + g_\omega \omega^0 \rho_v + g_\rho \rho_3^0 \rho_{tv}) d^3r. \quad (2.47)$$

Total binding energy is corrected for the center-of-mass motion by

$$E_{cm} = -\frac{\langle P_{cm}^2 \rangle}{2Am}, \quad (2.48)$$

where  $P_{cm}$  is the total momentum of a nucleus with  $A$  nucleons [22].

By considering only spherical nuclei, the set of coupled equations describing the nucleus is further simplified easing the computational cost. In spherical systems densities and fields depend solely on the radial coordinate  $r$ . The

nucleon spinor is determined by the quantum numbers of angular momentum  $j$  and  $m$ , parity  $\pi$  and isospin projection  $m_t = \pm\frac{1}{2}$  for neutron and proton, respectively

$$\psi(\mathbf{r}, s, t) = \begin{pmatrix} f(r)\Phi_{j,l,m}(\theta, \varphi, s) \\ ig(r)\Phi_{j,\tilde{l},m}(\theta, \varphi, s) \end{pmatrix} \chi_t(t), \quad (2.49)$$

with the isospin wave function  $\chi_t(t)$ . Angular and spin components of the wave function are coupled to total angular momentum  $j$

$$\Phi_{ljm}(\theta, \varphi, s) = \sum_{m_s, m_l} \langle \frac{1}{2}m_s l m_l | j m \rangle \chi_{m_s}(s) Y_{lm_l}(\theta, \varphi). \quad (2.50)$$

The orbital angular momentum  $l$  for the large, and  $\tilde{l}$  for the small component of the Dirac spinor are determined from the total angular momentum and parity

$$l = j + \frac{1}{2}, \quad \tilde{l} = j - \frac{1}{2} \quad \text{for } \pi = (-1)^{j+\frac{1}{2}}, \quad (2.51)$$

$$l = j - \frac{1}{2}, \quad \tilde{l} = j + \frac{1}{2} \quad \text{for } \pi = (-1)^{j-\frac{1}{2}}. \quad (2.52)$$

The Dirac equation reduces to a coupled set of two ordinary differential equations for radial functions  $f(r)$  and  $g(r)$

$$[m^*(r) + V(r)]f(r) + \left( \partial_r - \frac{\kappa - 1}{r} \right) g(r) = \epsilon f(r), \quad (2.53)$$

$$- \left( \partial_r + \frac{\kappa + 1}{r} \right) f(r) - [m^*(r) - V(r)]g(r) = \epsilon g(r), \quad (2.54)$$

where  $\kappa = \pm(j + \frac{1}{2})$  for  $j = l \mp \frac{1}{2}$ . Densities can be expressed using nucleon radial functions

$$\rho_s(r) = \sum_i (2j_i + 1) [|f_i(r)|^2 - |g_i(r)|^2], \quad (2.55)$$

$$\rho_v(r) = \sum_i (2j_i + 1) [|f_i(r)|^2 + |g_i(r)|^2], \quad (2.56)$$

$$\rho_{tv}(r) = \sum_i t_i (2j_i + 1) [|f_i(r)|^2 - |g_i(r)|^2], \quad (2.57)$$

$$\rho_C(r) = \sum_i (2j_i + 1)(1 - t_i) [|f_i(r)|^2 - |g_i(r)|^2], \quad (2.58)$$

where  $t_i = 1$  corresponds to neutrons and  $t_i = -1$  to protons. Expressing Klein-Gordon equations via these densities results with the following form:

$$\left( -\frac{\partial^2}{\partial r^2} - \frac{2}{r} \frac{\partial}{\partial r} + m_\phi^2 \right) = g_\phi(\rho_v(r))\phi(r). \quad (2.59)$$

## 2.4 Relativistic Hartree-Bogoliubov model

The inclusion of pairing correlations is essential for a correct description of structure phenomena in spherical open-shell nuclei and in deformed nuclei. For nuclei close to the  $\beta$ -stability line, pairing has been included in the relativistic mean-field model in the form of the simple BCS approximation [23]. However, for nuclei far from stability the BCS model presents only a poor approximation. In particular, in drip-line nuclei the Fermi level is found close to the particle continuum. The lowest particle-hole (ph) or particle-particle (pp) modes are often embedded in the continuum, and the coupling between bound and continuum states has to be taken into account explicitly. The BCS model does not provide a correct description of the scattering of nucleonic pairs from bound states to the positive energy continuum; levels high in the continuum become partially occupied. Including the system in a box of finite size leads to unreliable predictions for nuclear radii depending on the size of this box. In the non-relativistic case it has been shown that the Hartree-Fock-Bogoliubov (HFB) theory in the continuum provides a very elegant solution to this problem [24, 25].

The HFB theory [9] provides a unified description of  $ph$ - and  $pp$ -correlations on a mean-field level by using two average potentials: the self-consistent Hartree-Fock field  $\hat{\Gamma}$  which encloses all the long-range  $ph$ -correlations, and a pairing field  $\hat{\Delta}$  which sums up the  $pp$ -correlations. The ground state of a nucleus is described by a generalized Slater determinant  $|\Phi\rangle$  which represents the vacuum with respect to independent quasiparticles. The quasiparticle operators are defined by the unitary Bogoliubov transformation of the single-nucleoncreation and annihilation operators

$$\alpha_k^+ = \sum_l U_{lk} c_l^+ + V_{lk} c_l, \quad (2.60)$$

where  $U_{lk}$  and  $V_{lk}$  are the Hartree-Fock-Bogoliubov wave functions. The index  $l$  denotes an arbitrary basis, for instance the harmonic oscillator states. In the coordinate space representation  $l = (\mathbf{r}, \sigma, \tau)$ , with the spin index  $\sigma$  and the isospin index  $\tau$ . The HFB wave functions determine the hermitian single-particle density matrix

$$\rho_{lv} = \langle \Psi | c_v^+ c_l | \Psi \rangle = (V^* V^T)_{lv} \quad (2.61)$$

and the antisymmetric pairing tensor

$$\kappa_{lv} = \langle \Psi | c_v c_l | \Psi \rangle = (V^* U^T)_{lv}. \quad (2.62)$$

According to Valatin [26] these two densities can be combined into the generalized density matrix

$$\mathcal{R} = \begin{pmatrix} \rho & \kappa \\ -\kappa^* & 1 - \rho^* \end{pmatrix}, \quad (2.63)$$

which is both Hermitian ( $\mathcal{R}^\dagger = \mathcal{R}$ ) and idempotent ( $\mathcal{R}^2 = \mathcal{R}$ ).

The relativistic Hartree-Bogoliubov (RHB) model can be easily derived within the framework of covariant density functional theory. When pairing correlations are included, the energy functional depends not only on the density matrix  $\hat{\rho}$  and the meson fields  $\phi_m$  but in addition also on the pairing tensor:

$$E_{RHB}[\hat{\rho}, \hat{\kappa}, \phi_m] = E_{RMF}[\hat{\rho}, \phi_m] + E_{pair}[\hat{\kappa}], \quad (2.64)$$

where the pairing energy  $E_{pair}[\hat{\kappa}]$  is given by

$$E_{pair}[\hat{\kappa}] = \frac{1}{4} \text{Tr}[\hat{\kappa}^* V^{pp} \hat{\kappa}]. \quad (2.65)$$

$V^{pp}$  denotes a general two-body pairing interaction. The equation of motion for the generalized density matrix reads

$$i\partial_t \mathcal{R} = [\mathcal{H}(\mathcal{R}), \mathcal{R}], \quad (2.66)$$

and the generalized Hamiltonian is obtained as a functional derivative of the energy with respect to the generalized density

$$\mathcal{H} = \frac{\delta E_{RHB}}{\delta \mathcal{R}} = \begin{pmatrix} \hat{h}_D - m - \lambda & \hat{\Delta} \\ -\hat{\Delta}^* & -\hat{h}_D + m + \lambda \end{pmatrix}. \quad (2.67)$$

Variation of the energy functional with respect to single-particle density provides the single-particle Hamiltonian

$$\hat{h}_D = \frac{\delta E}{\delta \hat{\rho}} = \boldsymbol{\alpha}(\mathbf{p} + \mathbf{V}) + V + \beta(m - S), \quad (2.68)$$

while variation with respect to the pairing tensor provides the pairing field

$$\Delta = \frac{\delta E}{\delta \hat{\kappa}}, \quad \Delta_{ab}(\mathbf{r}, \mathbf{r}') = \frac{1}{2} \sum_{c,d} V_{abcd}^{pp}(\mathbf{r}, \mathbf{r}') \kappa_{cd}(\mathbf{r}, \mathbf{r}'), \quad (2.69)$$

where  $a, b, c$  and  $d$  denote the quantum numbers of Dirac spinors, and  $V_{abcd}^{pp}$  are the matrix elements of the pairing interaction. The pairing field can be written as

$$\begin{pmatrix} \hat{\Delta}_{++} & \hat{\Delta}_{+-} \\ \hat{\Delta}_{-+} & \hat{\Delta}_{--} \end{pmatrix}, \quad (2.70)$$

where  $+$  and  $-$  refer to the large and small components of the Dirac quasiparticle spinors  $U_k$  and  $V_k$

The stationary limit of Eq. (2.66) describes the ground state of an open-shell nucleus [27]. It is determined by the solutions of the Hartree-Bogoliubov equations

$$\begin{pmatrix} \hat{h}_D - m - \lambda & \hat{\Delta} \\ -\hat{\Delta}^* & -\hat{h}_D + m + \lambda \end{pmatrix} \begin{pmatrix} U_k(\mathbf{r}) \\ V_k(\mathbf{r}) \end{pmatrix} = E_k \begin{pmatrix} U_k(\mathbf{r}) \\ V_k(\mathbf{r}) \end{pmatrix}. \quad (2.71)$$

The chemical potential  $\lambda$  is determined by the particle number subsidiary condition in order that the expectation value of the particle number operator in the ground state equals the number of nucleons. The column vectors denote the quasiparticle wave functions, and  $E_k$  are the quasiparticle energies. The dimension of the RHB matrix equation is two times the dimension of the corresponding Dirac equation. For each eigenvector  $(U_k, V_k)$  with positive quasiparticle energy  $E_k > 0$  there exists an eigenvector  $(V_k^*, U_k^*)$  with quasiparticle energy  $-E_k$ . Since the baryon quasiparticle operators satisfy fermion commutation relations, the levels  $E_k$  and  $-E_k$  cannot be occupied simultaneously. For the solution that corresponds to a ground state of a nucleus with an even particle number, one usually chooses the eigenvectors with positive eigenvalues  $E_k$ .

The RHB equations are solved self-consistently with the potential determined within the mean-field approximation from the solutions of the Klein-Gordon equations

$$(-\Delta + m_\sigma^2) \sigma(\mathbf{r}) = -g_\sigma \rho_s(\mathbf{r}), \quad (2.72)$$

$$(-\Delta + m_\omega^2) \omega^0(\mathbf{r}) = g_\omega \rho_v(\mathbf{r}), \quad (2.73)$$

$$(-\Delta + m_\rho^2) \rho_3^0(\mathbf{r}) = g_\rho \rho_{tv}(\mathbf{r}), \quad (2.74)$$

$$-\Delta A^0(\mathbf{r}) = e \rho_C(\mathbf{r}). \quad (2.75)$$

for the  $\sigma$ -meson, the  $\omega$ -meson, the  $\rho$ -meson and photon field, respectively. The source terms in Eqs. (2.72)-(2.75) are sums of bilinear products of baryon amplitudes

$$\rho_s(\mathbf{r}) = \sum_{E_k > 0} V_k^+(\mathbf{r}) \gamma^0 V_k(\mathbf{r}), \quad (2.76)$$

$$\rho_v(\mathbf{r}) = \sum_{E_k > 0} V_k^+(\mathbf{r}) V_k(\mathbf{r}), \quad (2.77)$$

$$\rho_3(\mathbf{r}) = \sum_{E_k > 0} V_k^+(\mathbf{r}) \tau_3 V_k(\mathbf{r}), \quad (2.78)$$

$$\rho_{em}(\mathbf{r}) = \sum_{E_k > 0} V_k^+(\mathbf{r}) \frac{1 - \tau_3}{2} V_k(\mathbf{r}). \quad (2.79)$$

where the sum over positive-energy states  $E_k > 0$  corresponds to the no-sea approximation. The self-consistent solution of the Dirac-Hartree-Bogoliubov integro-differential equations and Klein-Gordon equations for the meson fields determines the ground state of a nucleus. For systems with spherical symmetry, i.e. closed-shell nuclei, the coupled system of equations has been solved using finite element method in coordinate space [28, 29], and by expansion in a basis of spherical harmonic oscillator [27].

The eigensolutions of Eq. (2.66) form a set of orthogonal (normalized) single quasiparticle states. The corresponding eigenvalues are the single quasiparticle



energies  $E_k$ . The self-consistent iteration procedure is performed in the basis of quasiparticle states. In order to obtain a better understanding of the structure of the Hartree-Bogoliubov wave function  $|\Psi\rangle$ , the self-consistent quasiparticle eigenspectrum is then transformed into the canonical basis of single-nucleon states. By definition the canonical basis  $\{|\psi_\mu(\mathbf{r})\rangle\}$  diagonalizes the single-nucleon density matrix  $\hat{\rho}$  in Eq. (2.61)

$$\hat{\rho}|\phi_\mu\rangle = v_\mu^2|\phi_\mu\rangle. \quad (2.80)$$

The transformation to the canonical basis determines the energies and pairing matrix elements

$$\epsilon_\mu = \langle\phi_\mu|\hat{h}_D - m|\phi_\mu\rangle \quad \text{and} \quad \Delta_\mu = \langle\phi_\mu|\hat{\Delta}|\phi_\mu\rangle, \quad (2.81)$$

and the occupation probabilities of single-nucleon states

$$v_\mu^2 = \frac{1}{2} \left( 1 - \frac{\epsilon_\mu - m - \lambda}{\sqrt{(\epsilon_\mu - m - \lambda)^2 + \Delta_\mu^2}} \right). \quad (2.82)$$

The self-consistent solution  $|\Psi\rangle$  for the ground-state of a nucleus has the structure of a BCS-state with those occupation probabilities (for details see Ref. [9]).

In early applications to nuclear matter [30], the same effective Lagrangian, i.e. identical meson-nucleon coupling parameters were used both in the  $ph$ -channel and in the  $pp$ -channel. It was found, however, that the standard RMF effective interactions that were adjusted to ground-state properties of spherical nuclei, produce pairing correlations that are much too strong when compared with empirical pairing gaps. The reason is that the meson-exchange forces have no momentum cut-off and, therefore, exhibit unphysical behavior at large momenta or, equivalently, at small distances. The strong repulsive force of the  $\omega$ -meson exchange generates a pairing field in nuclear matter that is more than a factor of three larger than the one calculated with the phenomenological Gogny force [31, 32]. This short-distance behavior of the effective interactions does not affect ordinary relativistic mean-field calculations in the  $ph$ -channel, where momenta above the Fermi momentum do not contribute. In calculations of pairing correlations, on the other hand, the occupation numbers decrease very slowly in momentum space, and the convergence of the momentum integral is achieved only by relativistic kinematic factors. However, in an effective theory there is no physical reason to use the same interactions both in the  $ph$ -channel and in the  $pp$ -channel. In non-relativistic self-consistent mean-field models, for instance, a number of different effective pairing forces have been used, often with no direct relation to the interaction in the  $ph$ -channel.

One possibility is a  $\delta$ -force in the  $pp$ -channel. This choice, however, introduces an additional cut-off parameter in energy and neither this parameter,

nor the strength of the interaction, can be determined in a unique way. In Ref. [27] it was therefore suggested that the pairing part of the well-known and very successful Gogny force [33] should be employed in the  $pp$ -channel

$$V^{pp}(1,2) = \sum_{i=1,2} e^{-\left(\frac{r_1-r_2}{\mu_i}\right)^2} (W_i + B_i P^\sigma - H_i P^\tau - M_i P^\sigma P^\tau), \quad (2.83)$$

with the set D1S for the parameters  $\mu_i$ ,  $W_i$ ,  $B_i$ ,  $H_i$  and  $M_i$  ( $i = 1, 2$ ). Values of the parameters are given in Table 2.1. This force has been very carefully adjusted to the pairing properties of finite nuclei all over the periodic table. In particular, the basic advantage of the Gogny force is the finite range, which automatically guarantees a proper cut-off in momentum space.

Table 2.1: Values of the parameters of the D1S Gogny pairing interaction.

| $i$ | $\mu_i$ [fm] | $W_i$   | $B_i$    | $H_i$    | $M_i$ [MeV] |
|-----|--------------|---------|----------|----------|-------------|
| 1   | 0.7          | -1720.3 | 1300.0   | -1813.53 | 1397.60     |
| 2   | 1.2          | 103.69  | -163.483 | 162.812  | -223.934    |

Since the Gogny force is a non-relativistic interaction, there is no unique way to implement this force in a relativistic calculation. For a general two-body interaction, the matrix elements of the relativistic pairing field read

$$\hat{\Delta}_{a_1 p_1, a_2 p_2} = \frac{1}{2} \sum_{a_3 p_3, a_4 p_4} \langle a_1 p_1, a_2 p_2 | V^{pp} | a_3 p_3, a_4 p_4 \rangle_{a^\kappa a_3 p_3, a_4 p_4}, \quad (2.84)$$

where the indices ( $p_1, p_2, p_3, p_4 = +, -$ ) refer to the large and small components of the quasiparticle Dirac spinors. In most applications of the RHB model, only the large components of the spinors  $U_k(\mathbf{r})$  and  $V_k(\mathbf{r})$  were included in the non-relativistic pairing tensor  $\hat{\kappa}$ . At this stage normalization is not taken into account. The resulting pairing field that has been used in calculation of finite nuclei reads

$$\hat{\Delta}_{a_1+, a_2+} = \frac{1}{2} \sum_{a_3+, a_4+} \langle a_1+, a_2+ | V^{pp} | a_3+, a_4+ \rangle_{a^\kappa a_3+, a_4+}. \quad (2.85)$$

The other components:  $\hat{\Delta}_{+-}$ ,  $\hat{\Delta}_{-+}$  and  $\hat{\Delta}_{--}$  are neglected, in accordance with the results that are obtained with the relativistic zero-range force [34]. Normalization is taken into account in a global way by multiplying the pairing field with an overall factor 1.15, adjusted to increase the strength of the Gogny force in such a way that the pairing energy calculated for the nucleus  $^{116}\text{Sn}$  is identical to the value obtained in the non-relativistic HFB calculation with the Gogny force D1S.

Concerning the use of phenomenological pairing forces in relativistic self-consistent structure models, it must be emphasized that pairing in nuclei is a fully non-relativistic phenomenon. Pairing effects are restricted to an energy window of a few MeV around the Fermi level, and their scale is well separated from the scale of binding energies, which are in the range of several hundred, and for heavy nuclei even more than a thousand MeV. So far there is no experimental evidence for any relativistic effect in the nuclear pairing field  $\hat{\Delta}$ . This is clearly different from the case of the mean field  $\hat{h}$ , where the importance of the spin-orbit potential has been known since the early days of the nuclear shell model. In a phenomenological approach based on density functional theory, such as the RHB framework, it is therefore fully justified to use a hybrid model with a non-relativistic pairing interaction.

## 2.5 Effective mass in relativistic models

In nonrelativistic mean-field models the effective nucleon mass  $m^*$  characterizes the energy dependence of an effective local potential which is equivalent to the nonlocal and frequency dependent microscopic nuclear potential [35].  $m^*$  represents a measure of the density of single-nucleon states around the Fermi surface and, therefore, it has a pronounced effect on the calculated properties of ground and excited states. In the case of Skyrme-type interactions, for instance, calculation of ground-state properties and excitation energies of quadrupole giant resonances have shown that a realistic choice for the nucleon effective mass is in the interval  $m^*/m = 0.8 \pm 0.1$  [36].

In the relativistic mean-field framework the expression “effective mass” has been used to denote different quantities. The quantity which is usually used to characterize an effective interaction, and which in the literature is most often called “the relativistic effective mass”, is also known as the “Dirac mass” [37]

$$m_D = m + S(\mathbf{r}) , \quad (2.86)$$

where  $m$  is the bare nucleon mass and  $S(\mathbf{r})$  denotes the scalar nucleon self-energy. The concept of the effective nucleon mass in the relativistic framework has been extensively analyzed in Refs. [37, 38]. Specifically, it has been pointed out that the Dirac mass should not be identified with the effective mass of the nonrelativistic mean-field models. Instead, the quantity which should be compared with the empirical effective mass derived from the nonrelativistic analyses of scattering and bound state data is given by

$$\frac{m^*}{m} = 1 - \frac{V(\mathbf{r})}{m} . \quad (2.87)$$

where  $V$  denotes the time-like component of the vector self-energy. The Dirac mass, on the other hand, is determined by two factors: (i) the empirical spin-orbit splittings in finite nuclei, and (ii) the binding energy at the saturation

density in nuclear matter. In the first order approximation, and assuming spherical symmetry, the spin-orbit part of the effective single-nucleon potential reads

$$V_{ls}(r) = \frac{1}{4\bar{M}^2} \left[ \frac{1}{r} \frac{d}{dr} (V - S) \right] \mathbf{l} \cdot \boldsymbol{\sigma}, \quad (2.88)$$

where  $\bar{M}$  is specified as

$$\bar{M} = M - \frac{1}{2}(V - S). \quad (2.89)$$

While the difference between the vector and scalar potentials determines the spin-orbit potential, their sum defines the effective single-nucleon potential and is determined by the nuclear matter binding energy at saturation density. The energy spacings between spin-orbit partner states in finite nuclei, and the nuclear matter binding and saturation, place the following constraints on the values of the Dirac mass and the nucleon effective mass:  $0.55m \leq m_D \leq 0.6m$ ,  $0.64m \leq m^* \leq 0.67m$ , respectively. These values have been used in most standard relativistic mean-field effective interactions. In comparison with the nonrelativistic models, the relativistic nucleon effective mass has a rather low value, and this results in a smaller density of states around the Fermi surface. Also, the range of allowed values of the nucleon effective mass is very narrow in the standard relativistic mean-field phenomenology, and there is really no room for any significant enhancement of the single-nucleon level densities at the Fermi surface.

### 2.5.1 Inclusion of a tensor term in $\omega$ -meson-nucleon coupling

An increase of the effective mass necessitates a reduction of the vector self-energy (see Eq. (2.87)). However, in order to retain the empirical value of the nuclear matter binding energy, the scalar self-energy should be reduced correspondingly. A serious problem arises because such an effective interaction would systematically underestimate the spin-orbit splittings in finite nuclei. A solution to this problem has been known for a long time, namely the tensor coupling of the  $\omega$ -meson to the nucleon. This interaction enhances the effective spin-orbit potential in finite nuclei, but is not included in the most commonly used relativistic mean-field models. In Ref. [39] it was shown that the tensor coupling

$$\mathcal{L}_{\text{tensor}} = -\frac{f_V}{2M} \bar{\psi} \sigma^{\mu\nu} \psi (\partial_\mu \omega_\nu - \partial_\nu \omega_\mu). \quad (2.90)$$

generates an additional term in the spin-orbit part of the effective nucleon potential, which now reads

$$V_{ls}(r) = \left[ \frac{1}{4\bar{M}^2} \frac{1}{r} \frac{d}{dr} (V - S) + \frac{f_V}{2M\bar{M}} \frac{1}{r} \frac{d\omega}{dr} \right] \mathbf{l} \cdot \boldsymbol{\sigma} \quad (2.91)$$

Naturally, the tensor term also appears in the Klein-Gordon equation for the  $\omega$ -meson which now reads

$$(-\Delta + m_\omega^2) \omega^0(\mathbf{r}) = g_\omega \rho_v(\mathbf{r}) - \frac{f_V}{4m} \rho_T, \quad (2.92)$$

with the tensor density obtained from a summation over states

$$\rho_T = i \nabla \cdot \sum_k V_k^+(\mathbf{r}) \boldsymbol{\gamma} V_k(\mathbf{r}). \quad (2.93)$$

Starting from the DD-ME1 interaction that has been used in the PN-RQRPA analysis of charge-exchange modes [40], and with the inclusion of the additional tensor omega-nucleon interaction (2.90), the parameters of the new interaction have been adjusted simultaneously to properties of nuclear matter and finite nuclei [16]. An additional constraint has been placed on the value of the nucleon effective mass. The modified effective interaction, denoted as DD-ME1\*, exhibits the following values for the Dirac mass and the nucleon effective mass:  $m_D = 0.67m$ ,  $m^* = 0.76m$ , respectively. These are the highest values for which a realistic description of nuclear matter and finite nuclei is still possible, i.e. the quality of the calculated nuclear matter equation of state and of ground-state properties of spherical nuclei is comparable to that of the DD-ME1 interaction. The value of the Dirac mass is also in agreement with the results of Ref. [39], where a detailed analysis was performed on the correlation between the isoscalar tensor coupling and the Dirac mass in successful mean-field models. Although the value of  $m^*$  is still lower than those typically used in nonrelativistic mean-field models, this result presents a significant improvement over the standard DD-ME1 density-dependent interaction ( $m_D = 0.58m$ ,  $m^* = 0.66m$ ).

The new interaction was used to calculate the energy spacings between spin-orbit partner states in the doubly closed-shell nuclei  $^{16}\text{O}$ ,  $^{40}\text{Ca}$ ,  $^{48}\text{Ca}$ ,  $^{132}\text{Sn}$ , and  $^{208}\text{Pb}$ . The results are shown in Table 2.2, in comparison with those obtained using the DD-ME1 interaction, and with the experimental data. Both interactions provide an excellent description of the spin-orbit splittings in finite nuclei. In order to illustrate the effect of the tensor-coupling term, in Fig. 2.1 the radial dependence of the spin-orbit term of the single-nucleon potential in the self-consistent solutions for the ground-state of  $^{132}\text{Sn}$  is displayed, calculated with the DD-ME1 and DD-ME1\* effective interactions. For DD-ME1\*, in particular, also the contributions of the first and second term in Eq. (2.91) are plotted separately. Even though the strength of the spin-orbit interaction that arises from the large scalar and vector self-energies (first term in Eq. (2.91)) is significantly reduced, the tensor omega-nucleon coupling effectively compensates this reduction, and the resulting spin-orbit potential is even slightly stronger than the one calculated with the DD-ME1 interaction. Therefore, while both interactions produce very similar results for the spin-orbit splittings in finite nuclei, the inclusion of the isoscalar tensor-coupling

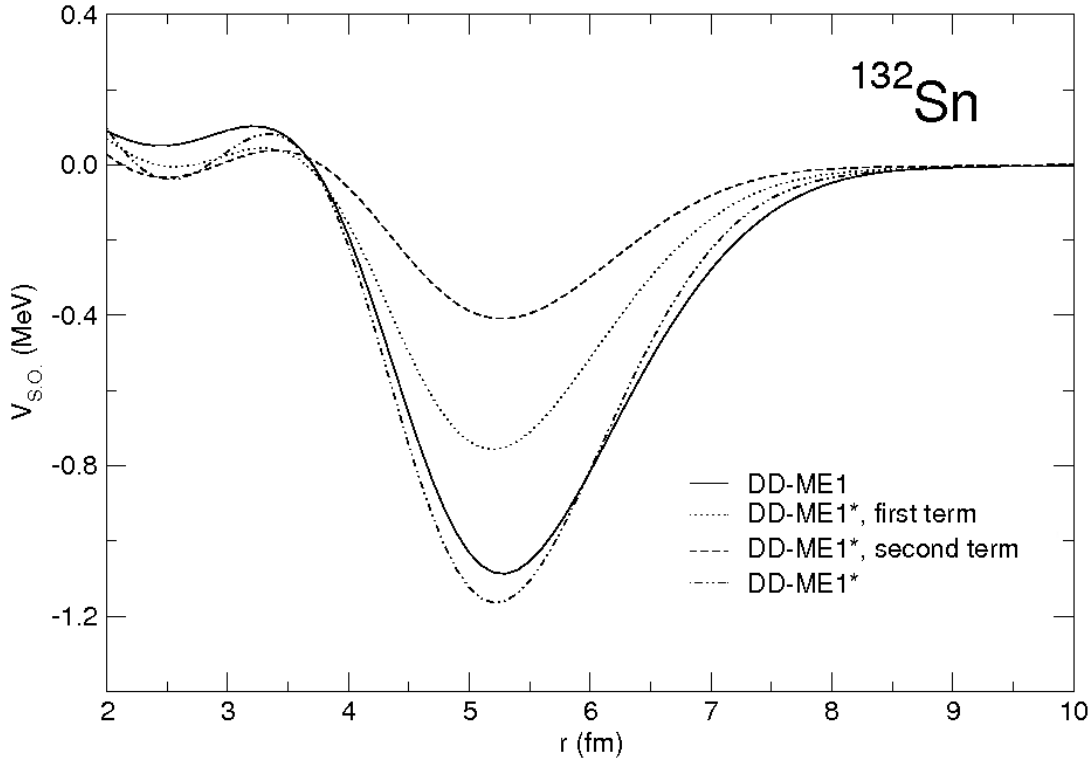


Figure 2.1: Radial dependence of the spin-orbit potential in the self-consistent solution for the ground-state of  $^{132}\text{Sn}$ . Full line corresponds to the potential obtained with the DD-ME1 interaction, while others are obtained with the DD-ME1\* interaction. First and second term correspond to the first and second term of the potential in (2.91).

term in DD-ME1\* allows for an increase of the Dirac mass and effective mass.

In Fig. 2.2 neutron and proton single-particle levels in  $^{132}\text{Sn}$  are displayed, calculated with DD-ME1 and DD-ME1\* and compared to experimental values. The levels calculated with DD-ME1\* are in much better agreement with data [42], than those obtained with the original DD-ME1 interaction.

### 2.5.2 Inclusion of momentum dependent terms in nucleon self-energies

A different solution to the problem of low effective mass is provided by relativistic mean-field model with momentum-dependent nucleon self-energies introduced in Refs. [43, 10]. In this model the standard effective Lagrangian with density-dependent meson-nucleon coupling vertices is extended by including a particular form of the couplings between the isoscalar meson fields and the derivatives of the nucleon fields. This leads to a linear momentum dependence

Table 2.2: Energy separation (in MeV) between spin-orbit partner states in doubly closed-shell nuclei, calculated with the DD-ME1 and DD-ME1\* interactions, and compared with experimental data [41].

|                   |          | DD-ME1 | DD-ME1* | Exp. |
|-------------------|----------|--------|---------|------|
| <sup>16</sup> O   | $\nu 1p$ | 6.32   | 6.02    | 6.18 |
|                   | $\pi 1p$ | 6.25   | 5.96    | 6.32 |
| <sup>40</sup> Ca  | $\nu 1d$ | 6.57   | 6.59    | 6.00 |
|                   | $\pi 1d$ | 6.51   | 6.51    | 6.00 |
| <sup>48</sup> Ca  | $\nu 1f$ | 7.69   | 7.79    | 8.38 |
|                   | $\nu 2d$ | 1.72   | 0.56    | 2.02 |
| <sup>132</sup> Sn | $\nu 2d$ | 1.88   | 2.03    | 1.65 |
|                   | $\pi 1g$ | 6.24   | 6.57    | 6.08 |
|                   | $\pi 2d$ | 1.82   | 1.98    | 1.75 |
| <sup>208</sup> Pb | $\nu 2f$ | 2.20   | 2.38    | 1.77 |
|                   | $\nu 1i$ | 6.84   | 7.13    | 5.84 |
|                   | $\nu 3p$ | 0.88   | 0.89    | 0.90 |
|                   | $\pi 2d$ | 1.65   | 1.82    | 1.33 |
|                   | $\pi 1h$ | 5.84   | 6.06    | 5.56 |

of the scalar and vector self-energies in the Dirac equation for the in-medium nucleon. Even though the extension of the standard mean-field framework is phenomenological, it is nevertheless based on Dirac-Brueckner calculations of in-medium nucleon self-energies, and consistent with the relativistic optical potential in nuclear matter, extracted from elastic proton-nucleus scattering data. In the extended model it is possible to increase the effective nucleon mass, while keeping a small Dirac mass which is required to reproduce the empirical strength of the effective spin-orbit potential.

In the work of Ref. [10], in particular, an improved Lagrangian density of the model with density-dependent and derivative couplings (D<sup>3</sup>C) has been introduced. The parameters of the coupling functions were adjusted to ground-state properties of eight doubly-magic spherical nuclei, and the results for nuclear matter, neutron matter, and finite nuclei were compared to those obtained with conventional RMF models. It was shown that the new effective interaction improves the description of binding energies, nuclear shapes and spin-orbit splittings of single-particle levels. More important, it was possible to increase the effective nucleon mass ( $m^* = 0.71 m$ ) and, correspondingly, the density of single-nucleon levels close to the Fermi surface as compared to standard RMF models. At the same time the Dirac mass was kept at the small value  $m_D = 0.54m$ , which ensures that the model reproduces the empirical spin-orbit splittings. The momentum dependence of the nucleon self-energies provides also a correct description of the empirical Schroedinger-equivalent

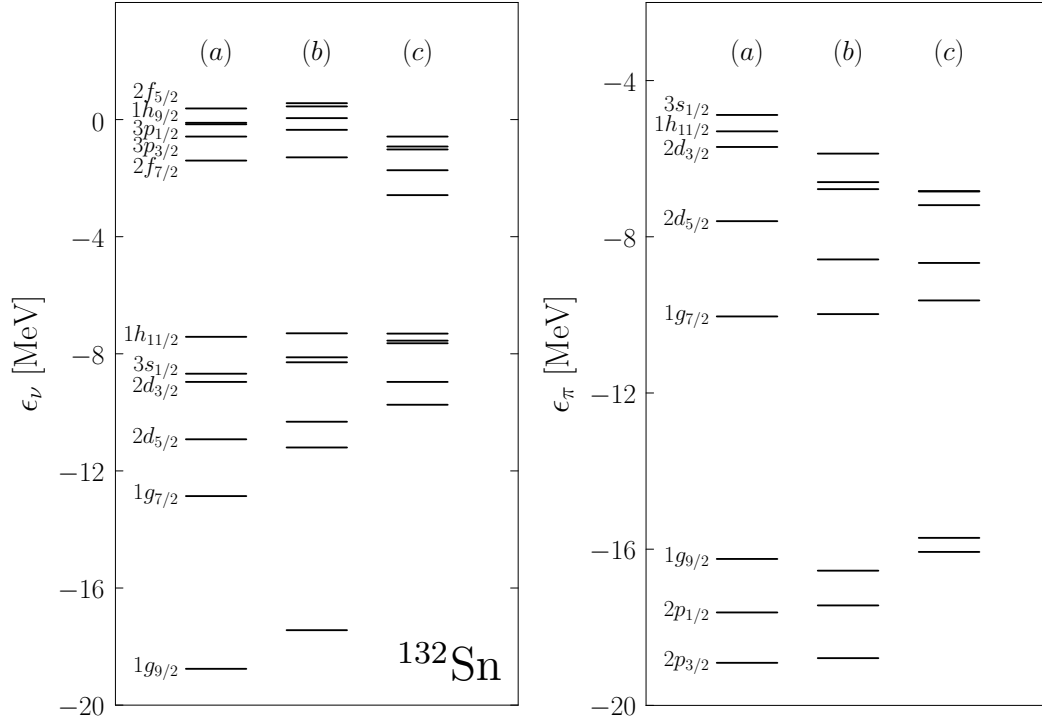


Figure 2.2: Neutron (left panel) and proton (right panel) single-particle energies for doubly-closed nucleus  $^{132}\text{Sn}$ . Plotted in the first column denoted with (a) are states calculated with the DD-ME1 interaction, DD-ME1\* (b) and compared to the experimental values in the last column (c). Experimental data is taken from [42].

central optical potential. This model is described in detail in Appendix A

The functional forms of the density dependence of the  $\sigma$ ,  $\omega$  and  $\rho$  meson-nucleon couplings are identical for the conventional DD-ME1 effective interaction and the D<sup>3</sup>C model. The latter includes momentum-dependent isoscalar scalar and vector self-energies, and thus contains two additional coupling functions  $\Gamma_S$  and  $\Gamma_V$ . In Ref. [10] these have been parametrized with the following functional form:

$$\Gamma_i(x) = \Gamma_i(\rho_{ref})x^{-a_i} \quad \text{for } i = S, V, \quad (2.94)$$

where  $x = \rho_v/\rho_{ref}$ ,  $\rho_v$  is the vector density, and the reference density  $\rho_{ref}$  corresponds to the vector density determined at the saturation point of symmetric nuclear matter. In the parameterization of Ref. [10]  $a_S = a_V = 1$ , and these values will be retained in the following calculation. The parameters  $\Gamma_S(\rho_{ref})$  and  $\Gamma_V(\rho_{ref})$  have been constrained by the requirement that the resulting optical potential in symmetric nuclear matter at saturation density has the value 50 MeV at a nucleon energy of 1 GeV. In total there are 10 adjustable parameters in the D<sup>3</sup>C model, compared to eight for the standard density-dependent



Table 2.3: Properties of symmetric nuclear matter at saturation density calculated with the models DD-ME1, D<sup>3</sup>C, and D<sup>3</sup>C\*.

|  | DD-ME1 | D <sup>3</sup> C | D <sup>3</sup> C* |
|--|--------|------------------|-------------------|
| $\varrho_{\text{sat}}$ [fm <sup>-3</sup> ] | 0.152  | 0.151            | 0.152             |
| $a_V$ [MeV]                                | -16.20 | -15.98           | -16.30            |
| $a_4$ [MeV]                                | 33.1   | 31.9             | 33.0              |
| $K_\infty$ [MeV]                           | 244.5  | 232.5            | 224.9             |
| $m_D/m$                                    | 0.58   | 0.54             | 0.57              |
| $m^*/m$                                    | 0.66   | 0.71             | 0.79              |
| $\Gamma_S$                                 | 0.0    | -21.632          | -146.089          |
| $\Gamma_V$                                 | 0.0    | 302.188          | 180.889           |

RMF models, e.g. the DD-ME1 parameterization.

The effective nucleon mass of the D<sup>3</sup>C model is  $m^* = 0.71 m$ , compared to  $m^* = 0.66 m$  for DD-ME1. In addition, starting from D<sup>3</sup>C, a new parameterization has been adjusted with  $m^* = 0.79 m$ , which is much closer to the effective masses used in non-relativistic Skyrme effective interactions [36, 44, 45]. The new effective interaction, denoted D<sup>3</sup>C\*, has been adjusted following the original procedure of Ref. [10], with an additional constraint on the effective nucleon mass. Value of  $m^* = 0.79 m$  is the highest for which a realistic description of nuclear matter and finite nuclei is still possible, and the quality of the calculated nuclear matter equation of state and of ground-state properties of spherical nuclei is comparable to that of the DD-ME1 and D<sup>3</sup>C interactions. The three interactions are compared in Table 2.3, where the characteristics of the corresponding nuclear matter equations of state at saturation point are listed: the saturation density  $\varrho_{\text{sat}}$ , the binding energy per particle  $a_V$ , the symmetry energy  $a_4$ , the nuclear matter compression modulus  $K_\infty$ , the Dirac mass  $m_D$ , and the effective (Landau) mass  $m^*$ . In addition, for the two interactions with energy-dependent single-nucleon potentials, the values of  $\Gamma_S(\rho_{ref})$  and  $\Gamma_V(\rho_{ref})$  are compared. A pronounced increase of the strength of the scalar field is noticeable. This is, however, compensated by the corresponding decrease of the strength of the vector coupling, so that the difference  $\Gamma_V(\rho_{ref}) - \Gamma_S(\rho_{ref})$  is practically the same for D<sup>3</sup>C and D<sup>3</sup>C\*. For both interactions the optical potential at 1 GeV nucleon energy has been constrained to 50 MeV. With the increase of the effective nucleon mass from DD-ME1 to D<sup>3</sup>C and D<sup>3</sup>C\*, there is a corresponding decrease of the nuclear matter compression modulus  $K_\infty$ . This correlation between  $K_\infty$  and  $m^*$  is also well known in non-relativistic Skyrme effective interactions [44].

In Fig. 2.3 the neutron and proton single-particle levels in <sup>132</sup>Sn are displayed, calculated in the relativistic mean-field model with the DD-ME1, D<sup>3</sup>C, and D<sup>3</sup>C\* effective interactions, in comparison with available data for the levels

close to the Fermi surface [42]. Compared to the DD-ME1 interaction, the enhancement of the effective mass in  $D^3C$  and  $D^3C^*$  results in the increase of the density of states around the Fermi surface, and the calculated spectra are in much better agreement with the empirical energy spacings.

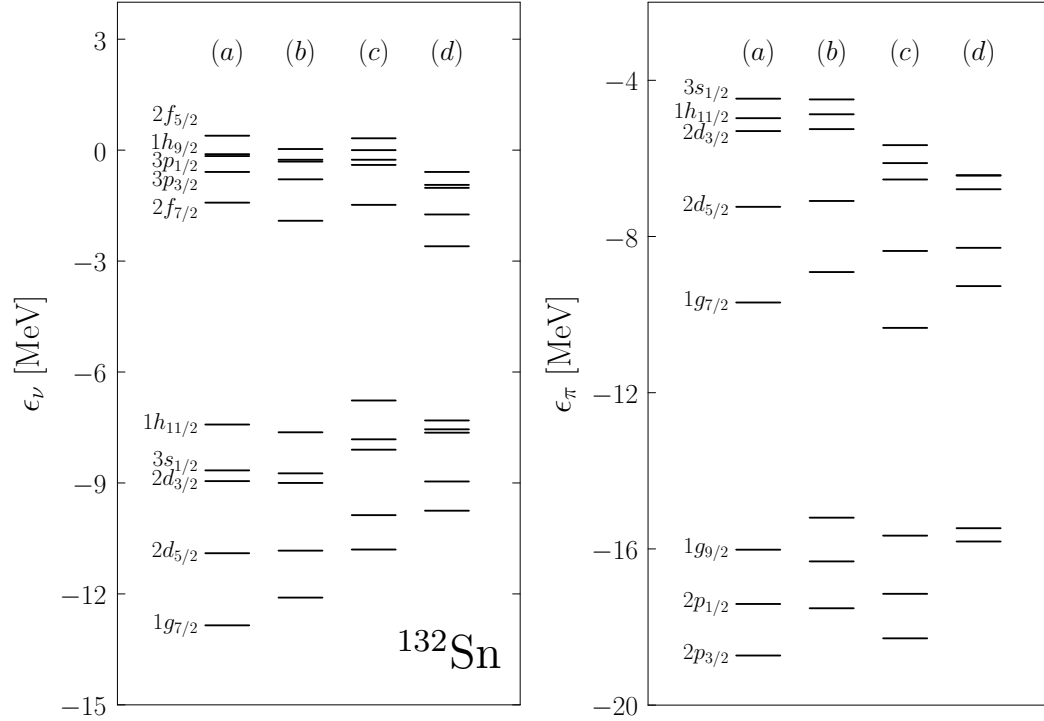


Figure 2.3: Neutron (left panel) and proton (right panel) single-particle energies for doubly-closed nucleus  $^{132}\text{Sn}$ . Plotted in the first column denoted with (a) are states calculated with the DD-ME1 interaction,  $D^3C$  (b) and  $D^3C^*$  (c) and compared to the experimental values in the last column (d). Experimental data is taken from [42].



# Chapter 3

## Relativistic quasiparticle random phase approximation

The successful application of the relativistic mean-field theory to finite nuclei has raised the possibility of describing excitation properties within the relativistic RPA framework. Small amplitude collective excitations of arbitrarily heavy nuclei can be accurately described by the random phase approximation (RPA) or, in the case of open-shell nuclei, by the quasiparticle random phase approximation (QRPA) [9].

A consistent and unified treatment of mean-field and pairing correlations is crucial for a quantitative analysis of ground-state properties and multipole response of unstable, weakly bound nuclei far from the line of stability. The relativistic quasiparticle random-phase approximation (RQRPA) has been formulated in the canonical single-nucleon basis of the relativistic Hartree-Bogoliubov (RHB) model [40]. The RHB model presents the relativistic extension of the Hartree-Fock-Bogoliubov framework, and it provides a unified description of particle-hole (ph) and particle-particle (pp) correlations. In this framework the ground state of a nucleus can be written either in the quasiparticle basis as a product of independent quasiparticle states, or in the canonical basis as a highly correlated BCS state. By definition, the canonical basis diagonalizes the density matrix and it is always localized. It describes both the bound states and the positive-energy single-particle continuum. The formulation of the RQRPA in the canonical basis is particularly convenient because, in order to describe transitions to low-lying excited states in weakly bound nuclei, the two-quasiparticle configuration space must include states with both nucleons in the discrete bound levels, states with one nucleon in a bound level and one nucleon in the continuum, and also states with both nucleons in the continuum.

Exploration of neutron-rich regions of the nuclear chart naturally includes the study of semi-leptonic weak interaction processes, e.g.  $\beta$ -decay, lepton capture, etc. The unique structure properties which characterize highly unstable

nuclei such as, for instance, the weak binding of the outermost nucleons and the coupling between bound states and the particle continuum, the modification of the effective nuclear potential and the formation of nuclei with very diffuse neutron densities, the occurrence of neutron skin and halo structures, will also affect the multipole response of these systems, and new modes of excitation could arise in nuclei at the limits of stability. Therefore a quantitative description of properties of ground and excited states in weakly bound nuclei, and especially studies of exotic modes far from stability, necessitate using the time-dependent self-consistent mean-field framework. To that end the proton-neutron relativistic quasiparticle RPA will be formulated as a relativistic extension of a nonrelativistic proton-neutron QRPA.

### 3.1 Relativistic random phase approximation

The relativistic random phase approximation (RRPA) represents the small amplitude limit of the time-dependent relativistic mean-field theory. In this section the RRPA matrix equations are derived from the response of the density matrix  $\hat{\rho}$

$$\hat{\rho}(\mathbf{r}, \mathbf{r}', t) = \sum_{i=1}^A |\psi_i(\mathbf{r}, t)\rangle \langle \psi_i(\mathbf{r}', t)|, \quad (3.1)$$

to an external field

$$\hat{F}(t) = \hat{F} e^{-i\omega t} + \text{h.c.} \quad (3.2)$$

that oscillates with a small amplitude. In the single-particle space, this field is represented by single-particle creation and destruction operators as

$$\hat{f}(t) = \sum_{kl} f_{kl}(t) \hat{a}_k^+ \hat{a}_l. \quad (3.3)$$

The equation of motion for the density operator reads

$$i\partial_t \hat{\rho} = \left[ \hat{h}(\hat{\rho}) + \hat{f}(t), \hat{\rho} \right]. \quad (3.4)$$

In the small amplitude limit the density matrix is expanded to linear order

$$\hat{\rho}(t) = \hat{\rho}^{(0)} + \delta\hat{\rho}(t), \quad (3.5)$$

where  $\hat{\rho}^{(0)}$  is the stationary ground-state density. From the definition of the density matrix (3.1), it follows that the density operator is a projector at all times, i.e.  $\hat{\rho}(t)^2 = \hat{\rho}(t)$ . In particular, this means that the eigenvalues of  $\hat{\rho}^{(0)}$  are 0 and 1. In the nonrelativistic case particle states above the Fermi level correspond to the eigenvalue 0, and hole states in the Fermi sea correspond to the eigenvalue 1. In the relativistic case one also has to take into account

states from the Dirac sea. In the no-sea approximation these states are not occupied, i.e. they correspond to the eigenvalue 0 of the density matrix. In the basis which diagonalizes  $\hat{\rho}^{(0)}$

$$\rho_{kl}^{(0)} = \delta_{kl}\rho_k^{(0)} = \begin{cases} 0 & \text{for unoccupied states above the Fermi sea (index } p \\ 1 & \text{for occupied states in the Fermi sea (index } h \\ 0 & \text{for unoccupied states in the Dirac sea (index } \alpha) \end{cases} \quad (3.6)$$

Since  $\hat{\rho}(t)$  is a projector at all times, one has in linear order

$$\hat{\rho}^{(0)}\delta\hat{\rho} + \delta\hat{\rho}\hat{\rho}^{(0)} = \delta\hat{\rho}. \quad (3.7)$$

This means that the non-vanishing matrix elements of  $\delta\hat{\rho}$  are  $\delta\rho_{ph}$ ,  $\delta\rho_{hp}$ ,  $\delta\rho_{\alpha h}$  and  $\delta\rho_{h\alpha}$ . These are determined by the solution of the TDRMF equation (3.4). In the linear approximation the equation of motion reduces to

$$i\partial_t\delta\hat{\rho} = [\hat{h}^{(0)}, \delta\hat{\rho}] + \left[ \frac{\partial\hat{h}}{\partial\rho}\delta\rho, \hat{\rho}^{(0)} \right] + [\hat{f}, \hat{\rho}^{(0)}], \quad (3.8)$$

where

$$\frac{\partial\hat{h}}{\partial\rho}\delta\rho = \sum_{ph} \frac{\partial\hat{h}}{\partial\rho_{ph}}\delta\rho_{ph} + \frac{\partial\hat{h}}{\partial\rho_{hp}}\delta\rho_{hp} + \frac{\partial\hat{h}}{\partial\rho_{\alpha h}}\delta\rho_{\alpha h} + \frac{\partial\hat{h}}{\partial\rho_{h\alpha}}\delta\rho_{h\alpha}. \quad (3.9)$$

In the small amplitude limit  $\delta\rho$  will, of course, also display a harmonic time dependence  $e^{-i\omega t}$ . Taking into account the fact that  $\hat{h}_{kl}^{(0)} = \delta_{kl}\epsilon_k$  is diagonal in the stationary basis, we obtain

$$\begin{aligned} (\omega - \epsilon_p + \epsilon_h)\delta\rho_{ph} &= f_{ph} + \sum_{p'h'} V_{ph'h'p'}\delta\rho_{p'h'} + V_{pp'h'h'}\delta\rho_{h'p'} \\ &+ \sum_{\alpha'h'} V_{ph'h'\alpha'}\delta\rho_{\alpha'h'} + V_{p\alpha'h'h'}\delta\rho_{h'\alpha'}, \\ (\omega - \epsilon_\alpha + \epsilon_h)\delta\rho_{\alpha h} &= f_{\alpha h} + \sum_{p'h'} V_{\alpha h'h'p'}\delta\rho_{p'h'} + V_{\alpha p'h'h'}\delta\rho_{h'p'} \\ &+ \sum_{\alpha'h'} V_{\alpha h'h'\alpha'}\delta\rho_{\alpha'h'} + V_{\alpha\alpha'h'h'}\delta\rho_{h'\alpha'}, \\ (\omega - \epsilon_h + \epsilon_p)\delta\rho_{hp} &= f_{hp} + \sum_{p'h'} V_{hh'p'p'}\delta\rho_{p'h'} + V_{hp'p'h'}\delta\rho_{h'p'} \\ &+ \sum_{\alpha'h'} V_{hh'p'\alpha'}\delta\rho_{\alpha'h'} + V_{h\alpha'p'h'}\delta\rho_{h'\alpha'}, \\ (\omega - \epsilon_h + \epsilon_\alpha)\delta\rho_{h\alpha} &= f_{h\alpha} + \sum_{p'h'} V_{hh'\alpha p'}\delta\rho_{p'h'} + V_{hp'\alpha h'}\delta\rho_{h'p'} \\ &+ \sum_{\alpha'h'} V_{hh'\alpha\alpha'}\delta\rho_{\alpha'h'} + V_{h\alpha'\alpha h'}\delta\rho_{h'\alpha'} \end{aligned} \quad (3.10)$$

or, in matrix form

$$\left[ \omega \begin{pmatrix} 1 & 0 \\ 0 & -1 \end{pmatrix} - \begin{pmatrix} A & B \\ B^* & A^* \end{pmatrix} \right] \begin{pmatrix} X \\ Y \end{pmatrix} = \begin{pmatrix} F \\ \bar{F} \end{pmatrix}. \quad (3.11)$$

The RPPA matrices  $A$  and  $B$  read

$$A = \begin{pmatrix} (\epsilon_p - \epsilon_h)\delta_{pp'}\delta_{hh'} & \\ & (\epsilon_\alpha - \epsilon_h)\delta_{\alpha\alpha'}\delta_{hh'} \end{pmatrix} + \begin{pmatrix} V_{ph'h'p'} & V_{ph'h'\alpha'} \\ V_{\alpha h'h'p'} & V_{\alpha h'h'\alpha'} \end{pmatrix} \quad (3.12)$$

$$B = \begin{pmatrix} V_{pp'h'h'} & V_{p\alpha'h'h'} \\ V_{\alpha p'h'h'} & V_{\alpha\alpha'h'h'} \end{pmatrix}, \quad (3.13)$$

and the amplitudes  $X$  and  $Y$  are defined as

$$X = \begin{pmatrix} \delta\rho_{ph} \\ \delta\rho_{\alpha h} \end{pmatrix} \quad \text{i} \quad Y = \begin{pmatrix} \delta\rho_{hp} \\ \delta\rho_{h\alpha} \end{pmatrix}. \quad (3.14)$$

The vectors which represent the external field contain the matrix elements

$$F = \begin{pmatrix} f_{ph} \\ f_{\alpha h} \end{pmatrix} \quad \text{i} \quad \bar{F} = \begin{pmatrix} f_{hp} \\ f_{h\alpha} \end{pmatrix}. \quad (3.15)$$

The eigenmodes of the system are determined by the RPA equation

$$\begin{pmatrix} A & B \\ -B^* & -A^* \end{pmatrix} \begin{pmatrix} X \\ Y \end{pmatrix}_\mu = \Omega_\mu \begin{pmatrix} F \\ \bar{F} \end{pmatrix}_\mu. \quad (3.16)$$

In principle, this is a non-Hermitian eigenvalue problem. In the non-relativistic case, however, it can be reduced to a Hermitian problem of half-dimension, if the RPA matrices are real and if  $(A+B)$  is positive definite. In this case one can also show that the eigenvalues  $\Omega_\mu^2$  are positive, i.e. the RPA eigenfrequencies  $\Omega_\mu$  are real [9].

The relativistic case is much more complicated. In addition to the normal  $ph$ -configurations with a particle  $p$  above the Fermi level and a hole  $h$  in the Fermi sea, one has the  $\alpha h$ -configurations with a particle  $\alpha$  in the Dirac sea, which is empty in the no-sea approximation, and a hole  $h$  in the Fermi sea. From Eq. (3.12) one can notice that the matrix  $(A+B)$  is not positive definite. The  $\alpha h$ -configurations have large negative diagonal matrix elements  $\epsilon_{\alpha h} = \epsilon_\alpha - \epsilon_h \leq -1.2$  GeV, and the RRPA equation can no longer be reduced to a Hermitian problem of half-dimension. In this case it is also not clear whether the eigenfrequencies are necessarily real, because the stability matrix

$$\mathcal{S} = \begin{pmatrix} A & B \\ B^* & A^* \end{pmatrix} \quad (3.17)$$

is no longer positive definite. Rather than minima, the solutions of the RMF equations are saddle points [46] in the multi-dimensional energy surface, and the Thouless theorem [47], which states that a positive definite stability matrix  $\mathcal{S}$  leads to a stable RPA equation with real frequencies, does not apply.

However, the opposite is not true: if the stability matrix is not positive definite, it does not automatically follow that the eigenvalues of the corresponding RPA matrix are not real. In fact, cases like this occur also in the non-relativistic RPA in the neighborhood of phase transitions, where the interaction  $V$  is very large and attractive. As compared to the matrix elements of  $V$ , the positive energies  $\epsilon_p - \epsilon_h$  on the diagonal of the stability matrix are not large enough to guarantee positive eigenvalues of  $\mathcal{S}$ . In the relativistic case the energies on the diagonal  $\epsilon_\alpha - \epsilon_h$  are negative. Even for small matrix

elements of  $V$  the stability matrix  $\mathcal{S}$  will have negative eigenvalues. However, as long as the diagonal part dominates, i.e. as long as one is not in the neighborhood of a phase transition, the RRPA eigenfrequencies are real. This can be easily demonstrated if instead of RPA amplitudes  $X$  and  $Y$ , one defines the generalized coordinates  $Q$  and momenta  $P$

$$Q = \frac{1}{\sqrt{2}}(X - Y^*), \quad P = \frac{i}{\sqrt{2}}(X + Y^*). \quad (3.18)$$

In the small amplitude limit the time-dependent mean-field equations take the form of classical Hamiltonian equations (see Ref. [9], Chapter 12)

$$\mathcal{H}(Q, P) = \frac{1}{2}(P^* - P)\mathcal{M}^{-1} \begin{pmatrix} P \\ -P^* \end{pmatrix} + \frac{1}{2}(Q^* Q)\mathcal{S} \begin{pmatrix} Q \\ Q^* \end{pmatrix}, \quad (3.19)$$

with the tensor of inertia

$$\mathcal{M} = \begin{pmatrix} A & -B \\ -B^* & A^* \end{pmatrix}^{-1}. \quad (3.20)$$

The large negative diagonal matrix elements are also present in the inertia tensor. If the off-diagonal matrix elements are not too large, a negative inertia and a negative curvature will result in real frequencies. In all applications of RRPA real frequencies have been found, though in none of these cases the stability matrix  $\mathcal{S}$  was positive definite. This also explains why the time-dependent RMF equations have stable solutions which describe oscillations with real frequencies around the stationary ground state, although the static solution itself corresponds to a saddle point.

The solution of the RPA equations in configuration space is much more complicated in the relativistic case. Firstly, because in addition to the usual  $ph$ -states, the configuration space includes a large number of  $\alpha h$ -states. A further complication arises because the full non-Hermitian RPA matrix has to be diagonalized, even in cases when the matrix elements are real. The usual method [9], which reduces the dimension of the RPA equations by half does not apply.

## 3.2 Relativistic quasiparticle random phase approximation

Relativistic RPA calculations have been performed since the early 1980s, but it is only more recently that non-linear meson self-interaction terms or density-dependent meson-nucleon couplings have been included in the RRPA framework [48, 49, 50]. As in the case of ground-state properties, the inclusion of a medium dependence in the residual interaction is necessary for a quantitative description of collective excited states. Another essential feature of



the RRPA is the fully consistent treatment of the Dirac sea of negative energy states. Within the no-sea approximation, in addition to the usual particle-hole pairs, the RRPA configuration space must also include pair-configurations built from positive-energy states occupied in the ground-state solution, and empty negative-energy states in the Dirac sea [51]. Collective excitations in open-shell nuclei can be analyzed with the relativistic quasiparticle random-phase approximation (RQRPA), which in Ref. [52] has been formulated in the canonical single-nucleon basis of the relativistic Hartree-Bogoliubov (RHB) model.

The RQRPA represents the small amplitude limit of the time-dependent relativistic Hartree-Bogoliubov (RHB) framework. The RQRPA matrix equations in the quasiparticle basis are, however, rather complicated and require the evaluation of the matrix elements of the Dirac Hamiltonian in the basis of the Hartree-Bogoliubov spinors  $U_k(\mathbf{r})$  and  $V_k(\mathbf{r})$ . A considerably simpler representation is provided by the canonical single-nucleon basis. Namely, any RHB wave function can be expressed either in the quasiparticle basis as a product of independent quasiparticle states, or in the canonical basis as a highly correlated BCS-state. The canonical basis is specified by the requirement that it diagonalizes the single-nucleon density matrix. The transformation to the canonical basis determines the energies and occupation probabilities of single-nucleon states that correspond to the self-consistent solution for the ground state of a nucleus. Since it diagonalizes the density matrix, the canonical basis is always localized. It describes both the bound states and the positive-energy single-particle continuum.

Taking into account the rotational invariance of the nuclear system, the matrix equations of the RQRPA read [52]:

$$\begin{pmatrix} A^J & B^J \\ B^{*J} & A^{*J} \end{pmatrix} \begin{pmatrix} X^{\lambda, JM} \\ Y^{\lambda, JM} \end{pmatrix} = \omega_\lambda \begin{pmatrix} 1 & 0 \\ 0 & -1 \end{pmatrix} \begin{pmatrix} X^{\lambda, JM} \\ Y^{\lambda, JM} \end{pmatrix}. \quad (3.21)$$

For each RQRPA energy  $\omega_\nu$ ,  $X^\nu$  and  $Y^\nu$  denote the corresponding forward and backward two-quasiparticle amplitudes, respectively. The coupled RQRPA matrices in the canonical basis read

$$\begin{aligned} A_{kk' ll'}^J &= H_{kl}^{11(J)} \delta_{k' l'} - H_{k'l}^{11(J)} \delta_{kl'} - H_{kl'}^{11(J)} \delta_{k'l} + H_{k'l'}^{11(J)} \delta_{kl} \\ &\quad + \frac{1}{2} (\xi_{kk'}^+ \xi_{ll'}^+ + \xi_{kk'}^- \xi_{ll'}^-) V_{kk' ll'}^J \\ &\quad + \zeta_{kk' ll'} \tilde{V}_{kl' k'l}^J \end{aligned} \quad (3.22)$$

$$\begin{aligned} B_{kk' ll'}^J &= \frac{1}{2} (\xi_{kk'}^+ \xi_{ll'}^+ - \xi_{kk'}^- \xi_{ll'}^-) V_{kk' ll'}^J \\ &\quad + \zeta_{kk' ll'} (-1)^{j_l - j_{l'} + J} \tilde{V}_{kl' k'l}^J. \end{aligned} \quad (3.23)$$

$H^{11}$  denotes the one-quasiparticle terms

$$H_{kl}^{11} = (u_k u_l - v_k v_l) h_{kl} - (u_k v_l + v_k u_l) \Delta_{kl}, \quad (3.24)$$

i.e. the canonical RHB basis does not diagonalize either the Dirac single-nucleon mean-field Hamiltonian  $\hat{h}_D$ , or the pairing field  $\hat{\Delta}$ . The occupation amplitudes  $v_k$  of the canonical states are eigenvalues of the density matrix.  $\tilde{V}$  and  $V$  are the particle-hole and particle-particle residual interactions, respectively. Their matrix elements are multiplied by the pairing factors  $\xi^\pm$  and  $\zeta$ , defined by the occupation amplitudes of the canonical states. The relativistic particle-hole interaction  $\tilde{V}$  is defined by the same effective Lagrangian density as the mean-field Dirac single-nucleon Hamiltonian  $\hat{h}_D$ .  $\tilde{V}$  includes the exchange of the isoscalar scalar  $\sigma$ -meson, the isoscalar vector  $\omega$ -meson, the isovector vector  $\rho$ -meson, and the electromagnetic interaction. The two-body matrix elements include also contributions from the spatial components of the vector fields. The pairing factors read

$$\zeta_{\kappa\kappa'\lambda\lambda'} = \begin{cases} \eta_{\kappa\kappa'}^+ \eta_{\lambda\lambda'}^+ & \text{for } \sigma, \omega^0, \rho^0, A^0; \text{ if J is even} \\ & \text{for } \boldsymbol{\omega}, \boldsymbol{\rho}, \mathbf{A}; \text{ if J is odd} \\ \eta_{\kappa\kappa'}^- \eta_{\lambda\lambda'}^- & \text{for } \sigma, \omega^0, \rho^0, A^0; \text{ if J is odd} \\ & \text{for } \boldsymbol{\omega}, \boldsymbol{\rho}, \mathbf{A}; \text{ if J is even} \end{cases} \quad (3.25)$$

with the  $\eta$ -coefficients defined by

$$\eta_{kk'}^\pm = u_k v_{k'} \pm v_k u_{k'} , \quad (3.26)$$

and

$$\xi_{kk'}^\pm = u_k u_{k'} \mp v_k v_{k'} . \quad (3.27)$$

$\sigma$ ,  $\omega^0$ ,  $\rho^0$ , and  $A^0$  denote the time-like components, and  $\boldsymbol{\omega}$ ,  $\boldsymbol{\rho}$ ,  $\mathbf{A}$  the spatial components of the meson and photon fields, respectively.

The RQRPA configuration space must also include the Dirac sea of negative energy states, i.e. pair-configurations formed from the fully or partially occupied states of positive energy and the empty negative-energy states from the Dirac sea. The inclusion of configurations built from occupied positive-energy states and empty negative-energy states is essential for current conservation and the decoupling of spurious states, as well as for a quantitative comparison with the experimental excitation energies of giant resonances.

The RQRPA model is fully self-consistent: the same interactions, in the particle-hole and particle-particle channels, are used both in the RHB equations that determine the canonical quasiparticle basis, and in the RQRPA equations. The parameters of the effective interactions are completely determined by the RHB calculations of ground-state properties, and no additional adjustment is needed in the RQRPA calculations. This is an essential feature of the RHB+RQRPA approach and it ensures that RQRPA amplitudes do not contain spurious components associated with the mixing of the nucleon number in the RHB ground state, or with the center-of-mass translational motion.

### 3.3 Proton-neutron RQRPA

Transitions between the  $0^+$  ground state of a spherical even-even parent nucleus and the  $J^\pi$  excited state of the corresponding odd-odd daughter nucleus are induced by a charge-exchange operator  $T^{JM}$ . Taking into account the rotational invariance of the nuclear system, the quasiparticle pairs can be coupled to good angular momentum and the matrix equations of the PN-RQRPA read

$$\begin{pmatrix} A^J & B^J \\ B^{*J} & A^{*J} \end{pmatrix} \begin{pmatrix} X^{\lambda J} \\ Y^{\lambda J} \end{pmatrix} = E_\lambda \begin{pmatrix} 1 & 0 \\ 0 & -1 \end{pmatrix} \begin{pmatrix} X^{\lambda J} \\ Y^{\lambda J} \end{pmatrix}. \quad (3.28)$$

The matrices  $A$  and  $B$  are defined in the canonical basis [9]

$$\begin{aligned} A_{pn,p'n'}^J &= H_{pp'}^{11} \delta_{nn'} + H_{nn'}^{11} \delta_{pp'} \\ &\quad + (u_p v_n u_{p'} v_{n'} + v_p u_n v_{p'} u_{n'}) V_{pn'np'}^{phJ} + (u_p u_n u_{p'} u_{n'} + v_p v_n v_{p'} v_{n'}) V_{pp'n'n'}^{ppJ} \\ B_{pn,p'n'}^J &= (-1)^{j_{p'} - j_{n'} + J} (u_p v_n v_{p'} u_{n'} + v_p u_n u_{p'} v_{n'}) V_{pp'nn'}^{phJ} \\ &\quad - (u_p u_n v_{p'} v_{n'} + v_p v_n u_{p'} u_{n'}) V_{pnp'n'}^{ppJ}. \end{aligned} \quad (3.29)$$

Here  $p, p'$ , and  $n, n'$  denote proton and neutron quasiparticle canonical states, respectively,  $V^{ph}$  is the proton-neutron particle-hole residual interaction, and  $V^{pp}$  is the corresponding particle-particle interaction. The canonical basis diagonalizes the density matrix and the occupation amplitudes  $v_{p,n}$  are the corresponding eigenvalues. The canonical basis, however, does not diagonalize the Dirac single-nucleon mean-field Hamiltonian  $\hat{h}_D$  and the pairing field  $\hat{\Delta}$ , and therefore the off-diagonal matrix elements  $H_{nn'}^{11}$  and  $H_{pp'}^{11}$  appear in Eq. (3.29):

$$H_{\kappa\kappa'}^{11} = (u_\kappa u_{\kappa'} - v_\kappa v_{\kappa'}) h_{\kappa\kappa'} - (u_\kappa v_{\kappa'} + v_\kappa u_{\kappa'}) \Delta_{\kappa\kappa'}, \quad (3.30)$$

For each energy  $E_\lambda$ ,  $X^{\lambda J}$  and  $Y^{\lambda J}$  in Eq. (3.29) denote the corresponding forward- and backward-going QRPA amplitudes, respectively. The total strength for the transition between the ground state of the even-even (N,Z) nucleus and the excited state of the odd-odd (N+1,Z-1) or (N-1,Z+1) nucleus, induced by the operator  $T^{JM}$ , reads

$$B_{\lambda J}^\pm = \left| \sum_{pn} \langle p || T^J || n \rangle (X_{pn}^{\lambda J} u_p v_n + (-1)^J Y_{pn}^{\lambda J} v_p u_n) \right|^2. \quad (3.31)$$

The isoscalar part of the interaction

$$V_\tau^{T=0} = \mathbf{1}_1 \mathbf{1}_2 \quad (3.32)$$

does not contribute to the particle-hole interaction due to vanishing matrix element

$$\langle pn' | \mathbf{1}_1 \mathbf{1}_2 | np' \rangle = 0. \quad (3.33)$$

However, the isovector part

$$V_{\tau}^{T=1} = \vec{\tau}_1 \vec{\tau}_2 = 4\tau_{1z}\tau_{2z} + 2\tau_{1+}\tau_{2-} + 2\tau_{1-}\tau_{2+} \quad (3.34)$$

gives a finite two-body matrix element

$$\langle pn' | \vec{\tau}_1 \vec{\tau}_2 | np' \rangle = 2. \quad (3.35)$$

Therefore, in the PN-RQRPA model only the isovector parts of the interaction contribute to the particle-hole matrix elements of the interaction.

The spin-isospin dependent interaction terms are generated by the  $\rho$ - and  $\pi$ -meson exchange. Because of parity conservation, the one-pion direct contribution vanishes in the mean-field calculation of a nuclear ground state. Its inclusion is important, however, in calculations of excitations that involve spin and isospin degrees of freedom. The particle-hole residual interaction in the PN-RQRPA is derived from the Lagrangian density

$$\mathcal{L}_{\pi+\rho}^{int} = -g_{\rho} \bar{\psi} \gamma^{\mu} \vec{\rho}_{\mu} \vec{\tau} \psi - \frac{f_{\pi}}{m_{\pi}} \bar{\psi} \gamma_5 \gamma^{\mu} \partial_{\mu} \vec{\pi} \vec{\tau} \psi. \quad (3.36)$$

Vectors in isospin space are denoted by arrows, and boldface symbols will indicate vectors in ordinary three-dimensional space.

The coupling between the  $\rho$ -meson and the nucleon is assumed to be a vertex function of the vector density  $\rho_v = \sqrt{j_{\mu} j^{\mu}}$ , with  $j_{\mu} = \bar{\psi} \gamma_{\mu} \psi$ . In Ref. [50] it has been shown that the explicit density dependence of the meson-nucleon couplings introduces additional rearrangement terms in the residual two-body interaction of the RRPA, and that their contribution is essential for a quantitative description of excited states. However, since the rearrangement terms include the corresponding isoscalar ground-state densities, it is easy to see that they are absent in the charge exchange channel, and the residual two-body interaction reads

$$V(\mathbf{r}_1, \mathbf{r}_2) = \vec{\tau}_1 \vec{\tau}_2 (\beta \gamma^{\mu})_1 (\beta \gamma_{\mu})_2 g_{\rho}(\rho_v(\mathbf{r}_1)) g_{\rho}(\rho_v(\mathbf{r}_2)) D_{\rho}(\mathbf{r}_1, \mathbf{r}_2) - \left( \frac{f_{\pi}}{m_{\pi}} \right)^2 \vec{\tau}_1 \vec{\tau}_2 (\boldsymbol{\Sigma}_1 \nabla_1) (\boldsymbol{\Sigma}_2 \nabla_2) D_{\pi}(\mathbf{r}_1, \mathbf{r}_2), \quad (3.37)$$

$D_{\rho(\pi)}$  denotes the meson propagator

$$D_{\rho(\pi)} = \frac{1}{4\pi} \frac{e^{-m_{\rho(\pi)} |\mathbf{r}_1 - \mathbf{r}_2|}}{|\mathbf{r}_1 - \mathbf{r}_2|}, \quad (3.38)$$

and

$$\boldsymbol{\Sigma} = \begin{pmatrix} \boldsymbol{\sigma} & 0 \\ 0 & \boldsymbol{\sigma} \end{pmatrix}. \quad (3.39)$$

For the  $\rho$ -meson coupling the functional form used in the DD-ME1 density-dependent effective interaction [16] is adopted

$$g_{\rho}(\rho_v) = g_{\rho}(\rho_{sat}) \exp[-a_{\rho}(x - 1)], \quad (3.40)$$

where  $x = \rho_v/\rho_{sat}$ , and  $\rho_{sat}$  denotes the saturation vector nucleon density in symmetric nuclear matter. For the pseudovector pion-nucleon coupling the standard values are used

$$m_\pi = 138.0 \text{ MeV} \quad \frac{f_\pi^2}{4\pi} = 0.08 . \quad (3.41)$$

The derivative type of the pion-nucleon coupling necessitates the inclusion of the zero-range Landau-Migdal term, which accounts for the contact part of the nucleon-nucleon interaction

$$V_{\delta\pi} = g' \left( \frac{f_\pi}{m_\pi} \right)^2 \vec{\tau}_1 \vec{\tau}_2 \boldsymbol{\Sigma}_1 \cdot \boldsymbol{\Sigma}_2 \delta(\mathbf{r}_1 - \mathbf{r}_2) , \quad (3.42)$$

with the parameters  $g'_{DD-ME1} = 0.55$ ,  $g'_{DD-ME1^*} = 0.62$  for DD-ME1\* interaction which includes the tensor coupling of the  $\omega$ -meson, and  $g'_{D^3C^*} = 0.76$  for the momentum-dependent interaction  $D^3C^*$  adjusted to reproduce experimental data on the GTR excitation energies.

With respect to the RHB calculation of the ground state of an even-even nucleus, the charge-exchange channel includes the additional one-pion exchange contribution. The PN-RQRPA model is fully consistent: the same interactions, both in the particle-hole and particle-particle channels, are used in the RHB equation that determines the canonical quasiparticle basis, and in the PN-RQRPA equation (3.28). In both channels the same strength parameters of the interactions are used in the RHB and RQRPA calculations.

The two-quasiparticle configuration space includes states with both nucleons in the discrete bound levels, states with one nucleon in the bound levels and one nucleon in the continuum, and also states with both nucleons in the continuum. In addition to the configurations built from two-quasiparticle states of positive energy, the RQRPA configuration space contains pair-configurations formed from the fully or partially occupied states of positive energy and the empty negative-energy states from the Dirac sea. As will be shown in the next section, the inclusion of configurations built from occupied positive-energy states and empty negative-energy states is essential for the consistency of the model.

In the  $pp$ -channel of the RHB model a phenomenological pairing interaction was used, the pairing part of the Gogny force,

$$V^{pp}(1,2) = \sum_{i=1,2} e^{-((\mathbf{r}_1-\mathbf{r}_2)/\mu_i)^2} (W_i + B_i P^\sigma - H_i P^\tau - M_i P^\sigma P^\tau), \quad (3.43)$$

with the set D1S [33] for the parameters  $\mu_i$ ,  $W_i$ ,  $B_i$ ,  $H_i$  and  $M_i$  ( $i = 1, 2$ ). This force has been very carefully adjusted to the pairing properties of finite nuclei all over the periodic table. In particular, the basic advantage of the Gogny force is the finite range, which automatically guarantees a proper cut-off in momentum space. In the present analysis the Gogny interaction in the  $T = 1$

$pp$ -channel of the PN-RQRPA will also be used. For the  $T = 0$  proton-neutron pairing interaction in open shell nuclei a similar interaction is employed: a short-range repulsive Gaussian combined with a weaker longer-range attractive Gaussian:

$$V_{12} = -V_0 \sum_{j=1}^2 g_j e^{-\frac{r_{12}^2}{\mu_j^2}} \hat{\Pi}_{S=1, T=0}. \quad (3.44)$$

where  $\hat{\Pi}_{S=1, T=0}$  projects onto states with  $S = 1$  and  $T = 0$ . This interaction was used in the non-relativistic QRPA calculation [53] of  $\beta$ -decay rates for spherical neutron-rich  $r$ -process waiting-point nuclei. As it was done in Ref. [53], the ranges  $\mu_1=1.2$  fm and  $\mu_2=0.7$  fm of the two Gaussians are taken from the Gogny interaction (3.43), and choose the relative strengths  $g_1 = 1$  and  $g_2 = -2$  so that the force is repulsive at small distances. The only remaining free parameter is  $V_0$ , the overall strength.

### 3.4 Treatment of allowed transitions in neutron-rich nuclei

Because of the identity of the Fermi operator with the nuclear isospin-lowering operator and because of the resulting selection rules, the only state that can be reached by the superallowed Fermi transition is the isobaric analog state. This state is shifted in energy relative to the  $\beta$ -decaying state by the Coulomb displacement energy and consequently lies beyond the  $Q_\beta$  window for  $\beta^-$  transitions. Therefore, allowed transitions in neutron-rich nuclei are exclusively Gamow-Teller transitions.

The total strength for the transition between the ground state of the even-even  $(N, Z)$  nucleus and a  $1^+$  state of the odd-odd  $(N-1, Z+1)$  nucleus, induced by the Gamow-Teller operator, reads

$$B_\lambda = \left| \sum_{pn} \langle p \| \sigma \tau_- \| n \rangle (X_{pn}^\lambda u_p v_n - Y_{pn}^\lambda v_p u_n) \right|^2. \quad (3.45)$$

The rate for the decay of an even-even nucleus in the allowed Gamow-Teller approximation reads

$$\frac{1}{T_{1/2}} = \sum_m \lambda_{if}^m = D^{-1} g_A^2 \sum_m \int dE_e \left| \sum_{pn} \langle 1_\lambda^+ \| \sigma \tau_- \| 0^+ \rangle \right|^2 \frac{dn_m}{dE_e}, \quad (3.46)$$

where  $D = 6163.4 \pm 3.8$  s [54].  $|0^+\rangle$  denotes the ground state of the parent nucleus, and  $|1_\lambda^+\rangle$  is a state of the daughter nucleus. The sum runs over all final states with an excitation energy smaller than the  $Q_{\beta^-}$  value. In order to account for the universal quenching of the Gamow-Teller strength function,

the effective weak axial nucleon coupling constant  $g_A = 1$  is used, instead of  $g_A = 1.26$  [55]. The kinematic factor in Eq. (3.46) can be written as

$$\frac{dn_m}{dE_e} = E_e \sqrt{E_e^2 - m_e^2} (\omega - E_e)^2 F(Z, A, E_e), \quad (3.47)$$

where  $\omega$  denotes the energy difference between the initial and the final state. The Fermi function  $F(Z, A, E_e)$  corrects the phase-space factor for the nuclear charge and finite nuclear size effects [56]. Defining  $E_{1_m^+}^*$  as the energy of the  $m$ -th excited  $J^\pi = 1^+$  state with respect to the ground state of the daughter nucleus, the maximum energy of the electron is

$$\omega = Q_\beta - E_{1_m^+}^*. \quad (3.48)$$

To obtain an approximation for the maximum energy of the electron without explicitly calculating the Q-value,  $Q_\beta$  is expressed in terms of nuclear ground-state binding energies

$$Q_\beta = \Delta M_{n-H} + B_{g.s.}(Z, N) - B_{g.s.}(Z + 1, N - 1), \quad (3.49)$$

with  $\Delta M_{n-H} = 0.78227$  MeV being the difference in mass between a neutron and a hydrogen atom. The ground-state binding energy of an odd-odd final nucleus, in the independent quasiparticle approximation is given by

$$B(Z + 1, N - 1) \approx B(Z, N) + \frac{dE}{dZ} - \frac{dE}{dN} + E_{2qp,lowest} \quad (3.50)$$

where  $dE/dZ \equiv \lambda_p$  and  $dE/dN \equiv \lambda_n$  are the proton and neutron Fermi energies, respectively, and  $E_{2qp,lowest}$  is the lowest two-quasiparticle excitation with respect to the parent nucleus [53]. The excitation energies of the  $q^+$  states with respect to the final ground state

$$E_{1_m^+}^* \approx E_{QRPA} - E_{2qp,lowest}, \quad (3.51)$$

where  $E_{QRPA}$  is the QRPA phonon energy. It follows from Eqs. (3.49) and (3.50) that the energy released in the transition from the ground state of the initial nucleus to a  $1^+$  state in the final nucleus is

$$\omega = Q_\beta - E_{1_m^+}^* \approx \lambda_n - \lambda_p + \Delta M_{n-H} - E_{QRPA}. \quad (3.52)$$

The Fermi function  $F(Z, A, E_e)$  corresponds to the ratio of the relativistic electron density at the nucleus to the density at infinity [57]. To account for finite nuclear size effects, the expression is evaluated for a point nucleus at the nuclear radius  $R$  obtaining

$$F(\pm Z, A, E_e) = 2(1 + \gamma_0) \left( \frac{2pR}{\hbar} \right)^{-2(1-\gamma_0)} e^{+\pi\nu} \left( \frac{|\Gamma(\gamma_0 + i\nu)|}{\Gamma(2\gamma_0 + 1)} \right)^2, \quad (3.53)$$

with

$$\gamma_0 \equiv \sqrt{1 - (\alpha Z)^2}, \quad \alpha \equiv \frac{e^2}{\hbar c} \quad (3.54)$$

and

$$\nu \equiv \pm \frac{\alpha Z E_e}{cp}. \quad (3.55)$$

In these expressions the plus sign is used in case of electron emission, and minus sign in case of positron emission, and  $Z$  is the charge of the final nucleus. Finally, to correct for electron screening  $F(\pm Z, A, E_e)$  is replaced with [56]

$$F(\pm Z, A, E_e) \rightarrow F(\pm Z, A, E_e \mp V_0) \left[ \frac{(E_e \mp V_0)^2 - (m_e c^2)^2}{E_e^2 - (m_e c^2)^2} \right]^{1/2} \left( \frac{E_e \mp V_0}{E_e} \right), \quad (3.56)$$

where  $V_0$  is the shift in the potential energy of the nucleus caused by the screening, and has been shown to be

$$V_0 \approx 1.45 \alpha^2 |Z|^{4/3} m_e c^2. \quad (3.57)$$

### 3.5 Half-lives of neutron rich nuclei around closed shells

The first attempt to apply the PN-RQRPA to  $\beta$ -decay processes, by employing the DD-ME1 interaction, was not successful. We tried to reproduce the empirical half-life of the  $^{78}\text{Ni}$ . This spherical nucleus undergoes high-energy fast  $\beta$ -decay and, since it has doubly-closed spherical shells, there is no contribution from the  $T = 0$  pairing. The PN-RQRPA with the DD-ME1 interaction predicts a half-life  $T_{1/2} = 7$  s, which is an order of magnitude longer than the experimental value  $T_{1/2} = 104 + 126 - 57$  ms [58]. The results of nonrelativistic QRPA calculations are much closer to the empirical half-life. For example, for the interaction DF3 the calculated half-life is  $T_{1/2} \approx 0.3$  s [59], whereas the Skyrme interaction SkO' predicts  $T_{1/2} \approx 0.6$  s [53]. Obviously, while the DD-ME1 interaction provides an accurate description of the high-energy region of the GT strength function, it does a rather poor job for the low-energy tail of the distribution. The problem, as already emphasized, lies in the low density of single-proton states around the Fermi level. This has motivated the adjustment of the new effective interaction DD-ME1\*, which has a considerably higher value of the nucleon effective mass, and consequently produces a higher density of single-nucleon states at the Fermi surface.

The change of the density of single-nucleon states will also affect the position of the GT resonance, and therefore the parameter of the zero-range Landau-Migdal force has to be readjusted. A higher density of states implies a lowering of the GT strength distribution, and this means that value of  $g' = 0.55$  used



with DD-ME1, has to be increased in order to reproduce the empirical excitation energy of GT resonances. For DD-ME1\* the new value  $g' = 0.62$  was adjusted to the position of the GT resonance in  $^{208}\text{Pb}$ . With this value of  $g'$  an excellent agreement between the calculated and experimental excitation energies of the GTR for  $^{48}\text{Ca}$ ,  $^{90}\text{Zr}$ , and  $^{112-124}\text{Sn}$  is also found. For the momentum-dependent interaction  $\text{D}^3\text{C}^*$  the value  $g' = 0.76$  was obtained in the same way.

With the new set of parameters (DD-ME1\* effective interaction,  $m_\pi = 138$  MeV,  $f_\pi^2/4\pi = 0.08$ ,  $g' = 0.62$ ), the  $\beta$ -decay half-life of  $^{78}\text{Ni}$  was recalculated. The value  $T_{1/2} = 0.9$  s presents a significant improvement over our first result obtained with DD-ME1, although it still overestimates the empirical half-life of  $^{78}\text{Ni}$ , and the values calculated with the nonrelativistic PN-QRPA. The most probable reason is that the value of the nucleon effective mass used in DD-ME1\* is still below the values used in the nonrelativistic effective interactions [53, 59]. A further increase of  $m^*$  in our relativistic model is, however, not possible without downgrading the agreement with experimental data on ground state properties of finite nuclei.

In recent years a number of experimental and theoretical studies have focused on the level structure and decay properties of neutron-rich nuclei in the vicinity of the doubly magic  $^{78}\text{Ni}$  and  $^{132}\text{Sn}$ . In particular, beta-decay rates in these two regions of the periodic chart have been extensively investigated in the framework of the nonrelativistic PN-QRPA [53, 54, 59]. In the next two sections the relativistic pn-QRPA will be applied in the calculation of  $\beta$ -decay half-lives of nuclei in the regions  $N \approx 50$  and  $N \approx 82$ .

### 3.5.1 $N \approx 50$ region

In this region iron, nickel, and zinc isotopic chains, and the  $N = 50$  isotones were investigated. The structure of the low-energy part of the GT strength distribution crucially depends on the occupancy of the  $Z = 28$  proton shell. It should be noted that, because of possible deformation effects in the Fe and Zn chains, these nuclei might not be as good as the Ni isotopes for a comparison with results of spherical PN-QRPA calculations.

In Fig. 3.1 the calculated half-lives of the Fe isotopes (two holes in the  $\pi 1f_{7/2}$  orbit) are displayed in comparison with the available experimental data [60]. The results are obtained with the DD-ME1\* interaction,  $m_\pi = 138$  MeV,  $f_\pi^2/4\pi = 0.08$ ,  $g' = 0.62$ , Gogny D1S  $T=1$  pairing, and the  $\text{D}^3\text{C}^*$  interaction,  $g' = 0.76$ . Predicted half-lives are displayed both with and without the inclusion of the  $T = 0$  pairing channel. Obviously, the absolute values of the calculated half-lives are very sensitive to the  $T = 0$  pairing strength. Without the inclusion of this pairing channel, in all considered cases the calculated half-lives are at least an order of magnitude longer than the experimental values. In the case of iron isotopes the pairing strength parameter  $V_0$  has been

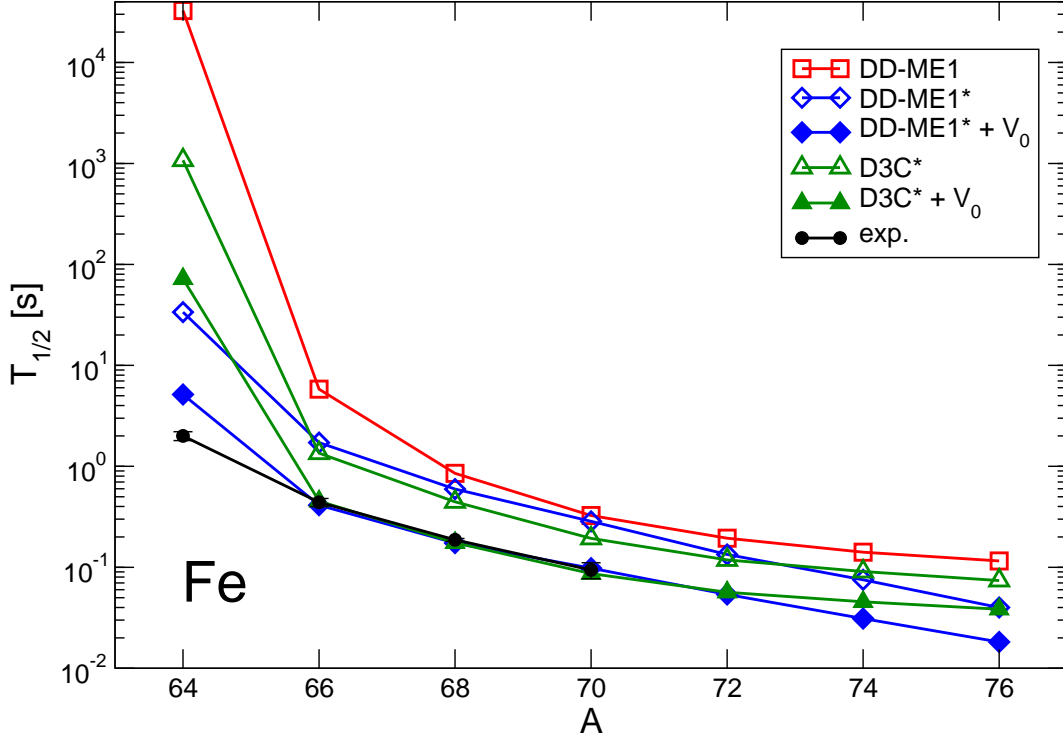


Figure 3.1: Half-lives of iron isotopes calculated with various interactions. Open symbols denote values obtained without  $T = 0$  residual interaction, while full symbols denote values with additional interaction. Strength of the residual pairing is  $V_0 = 115$  MeV for the DD-ME1\* interaction, and  $V_0 = 125$  MeV for the momentum-dependent D3C\* interaction. Theoretical results are compared to experimental values taken from Ref. [60].

adjusted to reproduce the half-life of  $^{68}\text{Fe}$ . With this value it is possible to reproduce the half-lives of the  $^{66}\text{Fe}$  and  $^{70}\text{Fe}$  isotopes very accurately, whereas the lifetime of the  $^{64}\text{Fe}$  isotope is somewhat overestimated.

It is, however, probable that the inclusion of a strong  $T = 0$  pairing partially compensates the deficiencies of the single-particle spectra calculated with the DD-ME1\* interaction. The ground-state occupation probabilities for the single-particle levels relevant for this  $\beta$ -decay process are listed in Table 3.1. Since the  $\pi 1f_{7/2}$  orbit is not fully occupied, the transition with the highest probability is dominated (95% of the neutron-to-proton QRPA amplitude) by the back spin-flip configuration  $\nu 1f_{5/2} \rightarrow \pi 1f_{7/2}$ . Other transitions, with much smaller probabilities, correspond to the back spin-flip configuration  $\nu 2p_{1/2} \rightarrow \pi 2p_{3/2}$ , and the core-polarization configurations  $\nu 1f_{5/2} \rightarrow \pi 1f_{5/2}$ ,  $\nu 1g_{9/2} \rightarrow \pi 1g_{9/2}$ ,  $\nu 2p_{3/2} \rightarrow \pi 2p_{3/2}$ , and  $\nu 2p_{1/2} \rightarrow \pi 2p_{1/2}$ . Since except  $\pi 1f_{7/2}$ , all proton single-particle levels listed in Table 3.1 have very small occupation probabilities, the only sizeable contribution from the  $T = 0$  pairing to the

RQRPA matrices comes from the  $\pi 1f_{7/2}(\nu 1f_{5/2})^{-1}$  pair. Because of the attractive nature of the pairing interaction, the large diagonal matrix element  $v_p^2 V_{pnpn}^{pp}$  (p and n denote  $\pi 1f_{7/2}$  and  $\nu 1f_{5/2}$  states, respectively) effectively reduces the sum of the quasiparticle energies:  $H_{pp}^{11} + H_{nn}^{11} = E_p + E_n$ . This means that the  $T = 0$  pairing compensates for the fact that even the DD-ME1\* interaction still predicts a rather low density of states around the Fermi surface, i.e., the  $\pi 1f_{7/2}$  and  $\nu 1f_{5/2}$  single-particle levels are still too close. The inclusion of the  $T = 0$  pairing will affect only configurations with the proton level at least partially occupied.

Table 3.1: Occupation probabilities of neutron and proton single-particle states for the ground-states of  $^{76}\text{Fe}$  and  $^{80}\text{Zn}$ .

| $^{76}\text{Fe}$ |          |         | $^{80}\text{Zn}$ |          |         |
|------------------|----------|---------|------------------|----------|---------|
| $nlj$            | NEUTRONS | PROTONS | $nlj$            | NEUTRONS | PROTONS |
| $1f_{7/2}$       | 1.000    | 0.743   | $1f_{7/2}$       | 1.000    | 0.980   |
| $1f_{5/2}$       | 1.000    | 0.019   | $1f_{5/2}$       | 1.000    | 0.260   |
| $2p_{3/2}$       | 1.000    | 0.005   | $2p_{3/2}$       | 1.000    | 0.098   |
| $2p_{1/2}$       | 1.000    | 0.004   | $2p_{1/2}$       | 1.000    | 0.040   |
| $1g_{9/2}$       | 1.000    | 0.004   | $1g_{9/2}$       | 1.000    | 0.014   |

For the Ni isotopes the  $\pi 1f_{7/2}$  orbit is completely occupied, i.e., in this case the transition  $\nu 1f_{5/2} \rightarrow \pi 1f_{7/2}$  is blocked. The  $T = 0$  pairing could only have an effect on the  $\pi 1g_{9/2}(\nu 1g_{9/2})^{-1}$  configuration, because the  $\nu 1g_{9/2}$  orbit is not fully occupied for isotopes below  $^{78}\text{Ni}$ . However, it is true that when this orbit is almost empty ( $^{70}\text{Ni}$ ,  $^{72}\text{Ni}$ ) there is a large contribution from the pairing interaction, but at the same time there is only a small number of neutrons which can participate in the  $\beta$ -decay process. On the other hand, when this orbit is almost full ( $^{74}\text{Ni}$ ,  $^{76}\text{Ni}$ ), the contribution from the  $T = 0$  pairing becomes negligible. In contrast to the iron isotopic chain, it was not possible to obtain a single value of the  $T = 0$  pairing strength parameter that would provide a consistent description of the entire chain of nickel isotopes. To reproduce the experimental half-lives, an extremely strong  $T = 0$  pairing would have to be used and this would cause the collapse of the PN-RQRPA calculation. Because of the closed  $Z = 28$  proton shell, the  $T = 0$  pairing is not effective in Ni isotopes and, therefore, the calculated  $\beta$ -decay half-lives, shown in Fig. 3.2, overestimate the experimental data.

In this mass region the half-lives of zinc isotopes were also analyzed. In Ref. [53] the measured half-lives of three zinc isotopes  $^{76}\text{Zn}$ ,  $^{78}\text{Zn}$ , and  $^{80}\text{Zn}$ , and of  $^{82}\text{Ge}$ , were used to adjust the  $T = 0$  pairing strength. It was shown that the experimental lifetimes can all be reproduced with a single value of the  $T = 0$  pairing strength,  $V_0 = 230$  MeV. In the present calculation the mea-

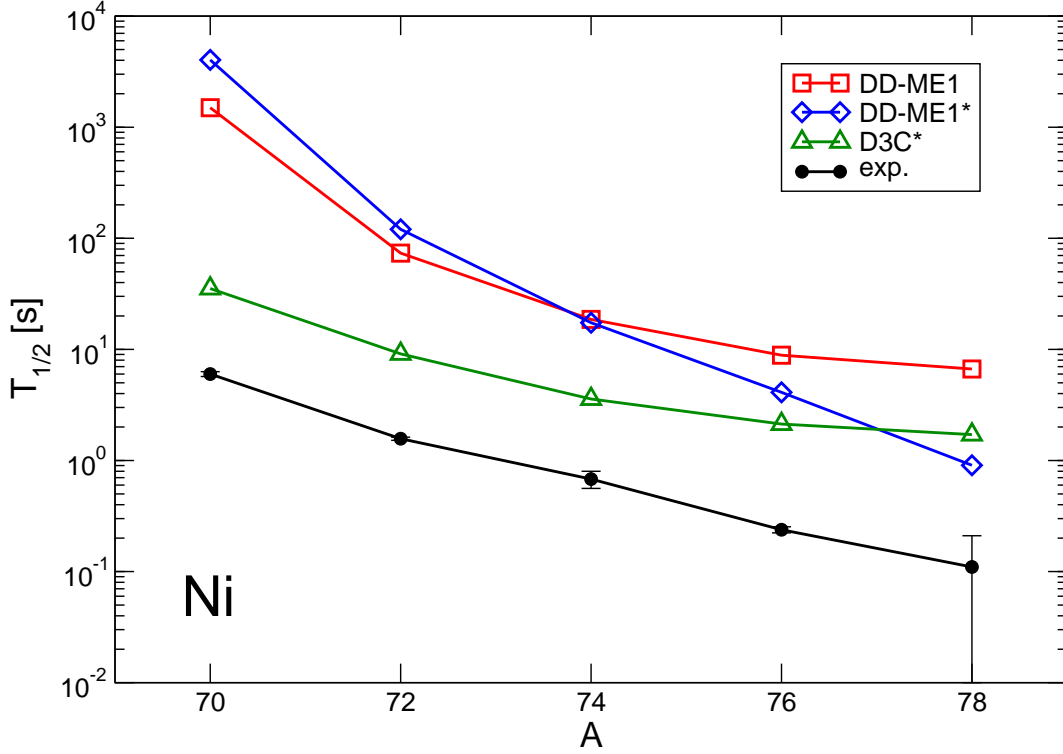


Figure 3.2: Half-lives of nickel isotopes calculated with various interactions. Experimental values taken from Ref. [60], except for  $^{78}\text{Ni}$  which is taken from Ref. [58].

sured half-lives are only reproduced by using a much stronger  $T = 0$  pairing interaction. The effect that  $T = 0$  pairing has on the  $\beta$ -decay probability is illustrated in the example of the semi-magic nucleus  $^{80}\text{Zn}$ . In Table 3.1 the ground-state occupation probabilities for the relevant single-particle levels are included. It is important to note that, because of the  $T = 1$  pairing, the occupation probability of the  $\pi 1f_{7/2}$  state is not equal to one. Besides  $\pi 1f_{7/2}$ , only  $\pi 1f_{5/2}$  has a sizeable occupation probability among the proton states. The  $T = 0$  pairing interaction produces a large contribution to the RQRPA matrices for the following configurations:  $\pi 1f_{5/2}(\nu 1f_{5/2})^{-1}$  and  $\pi 1f_{7/2}(\nu 1f_{5/2})^{-1}$ . Because the transition  $\nu 1f_{5/2} \rightarrow \pi 1f_{7/2}$  is essentially blocked, the effect of  $T = 0$  pairing is much weaker than in the case of Fe isotopes. If the parameter  $V_0$  is kept below  $\approx 250$  MeV, the  $T = 0$  pairing has virtually no effect on the calculated half-lives. In the interval between  $V_0 = 0$  MeV and  $V_0 = 220$  MeV the half-life decreases by just 10%. With a further increase of  $V_0$ , however, the calculated half-life displays a steep decrease. The measured half-life is reproduced for  $V_0 \approx 330$  MeV. The corresponding distributions of neutron-to-proton QRPA amplitudes for three values of the  $T = 0$  pairing strength ( $V_0 = 0$  MeV,  $V_0 = 255$  MeV, and  $V_0 = 330$  MeV) are shown in Table 3.2. As

one would expect, in the absence of  $T = 0$  pairing, the  $\beta$ -decay process is characterized by two transitions. The lower one is dominated by the back spin-flip transition  $\nu 2p_{1/2} \rightarrow \pi 2p_{3/2}$ , whereas the higher component represents a mixture of core-polarization transitions. Increasing the  $T = 0$  pairing strength to  $V_0 = 255$  MeV, two points are noted: (i) transitions built from the back spin-flip configuration  $\nu 2p_{1/2} \rightarrow \pi 2p_{3/2}$  and the core-polarization configurations are no longer well separated, and (ii) an additional transition appears, built dominantly on the back spin-flip configuration  $\nu 1f_{5/2} \rightarrow \pi 1f_{7/2}$ , which results in a sudden reduction of the calculated half-life. Of course, this would not be possible if  $\pi 1f_{7/2}$  was fully occupied. This was the case for the Ni isotopes, and consequently their half-lives could not be improved by increasing the strength of the  $T = 0$  pairing. Since the  $T = 0$  pairing has a strong effect on the  $\nu 1f_{5/2} \rightarrow \pi 1f_{7/2}$  configuration, a further increase of its strength lowers the energy of the corresponding transition. For  $V_0 = 330$  MeV only one transition is found, predominantly based on the  $\nu 1f_{5/2} \rightarrow \pi 1f_{7/2}$  configuration.

### 3.5.2 $N \approx 82$ region

In the mass region around the doubly magic  $^{132}\text{Sn}$ , the  $\beta$ -decay half-lives of the cadmium, tin, and tellurium isotopic chains have been calculated. In Fig. 3.4 the calculated half-lives of the Cd isotopes are plotted. The results correspond to two calculations, with  $V_0 = 0$  and  $V_0 = 225$  MeV for the strength parameter of the  $T = 0$  pairing. As in the cases that have been considered in the previous section, the calculated half-lives are more than an order of magnitude too long when the  $T = 0$  pairing is not included. With the pairing strength parameter  $V_0 = 225$  MeV adjusted to reproduce the half-life of  $^{130}\text{Cd}$ , the PN-QRPA calculation reproduces the experimental half-lives of the Cd isotopic chain. With two holes in the  $\pi 1g_{9/2}$  orbit, the situation in the cadmium chain is similar to that of Fe isotopes (two holes in the  $\pi 1f_{7/2}$  orbit). The  $\beta$ -decay process in the Cd isotopes is dominated by the back spin-flip transition  $\nu 1g_{7/2} \rightarrow \pi 1g_{9/2}$ . Again, an increase of the  $T = 0$  pairing strength partially compensates for the fact that the difference between the  $\nu 1g_{7/2}$  and  $\pi 1g_{9/2}$  single-particle energies is too small, due to a relatively small effective mass.

For the Sn isotopes the  $\pi 1g_{9/2}$  orbit is completely occupied and the transition  $\nu 1g_{7/2} \rightarrow \pi 1g_{9/2}$  is blocked. A similar problem was already encountered for the Ni isotopes. One would, therefore, expect that the calculated half-lives of the Sn isotopes will overestimate the experimental values by at least an order of magnitude, and furthermore that it will not be possible to improve the results by simply increasing the  $T = 0$  pairing strength. However, this turns out to be true only for  $^{132}\text{Sn}$ . The model predicts that this isotope is stable against  $\beta$ -decay, whereas the experimental half-life is  $T_{1/2} = 39.7 \pm 0.5$  s [60]. In Fig. 3.5 the calculated half-lives of the Sn isotopes are displayed, in comparison with the available experimental data [60]. In contrast to  $^{132}\text{Sn}$ , the

Table 3.2:  $\beta^-$ -transitions in  $^{80}\text{Zn}$  for three values of the  $T = 0$  pairing strength. The contribution (in percent) of a particular configuration to the QRPA amplitude is included in parenthesis.

| $V_0 = 0 \text{ MeV } (T_{1/2} = 18.9 \text{ s})$ |                                     | $V_0 = 255 \text{ MeV } (T_{1/2} = 13.1 \text{ s})$ |                                     | $V_0 = 330 \text{ MeV } (T_{1/2} = 0.6 \text{ s})$ |                                     |
|---|-------------------------------------|---|-------------------------------------|--|-------------------------------------|
| $E_f - E_i \text{ (MeV)}$                         |                                     | $E_f - E_i \text{ (MeV)}$                           |                                     | $E_f - E_i \text{ (MeV)}$                          |                                     |
| -3.088  | $g_{9/2} \rightarrow g_{9/2}$ (12%) | -3.271  | $f_{5/2} \rightarrow f_{5/2}$ (11%) | -5.273   | $f_{7/2} \rightarrow f_{7/2}$ (5%)  |
|   | $p_{1/2} \rightarrow p_{3/2}$ (80%) |   | $g_{9/2} \rightarrow g_{9/2}$ (18%) |  | $f_{5/2} \rightarrow f_{7/2}$ (71%) |
| -2.690  | $p_{3/2} \rightarrow p_{3/2}$ (6%)  | -2.982  | $f_{5/2} \rightarrow f_{5/2}$ (13%) | -2.302   | $p_{1/2} \rightarrow p_{1/2}$ (13%) |
|   | $p_{1/2} \rightarrow p_{3/2}$ (11%) |   | $g_{9/2} \rightarrow g_{9/2}$ (16%) |  | $g_{9/2} \rightarrow g_{9/2}$ (15%) |
|   | $f_{5/2} \rightarrow f_{5/2}$ (22%) |   | $p_{1/2} \rightarrow p_{3/2}$ (19%) |  | $f_{5/2} \rightarrow f_{7/2}$ (58%) |
|   | $g_{9/2} \rightarrow g_{9/2}$ (54%) |   | $p_{3/2} \rightarrow f_{5/2}$ (47%) |  |                                     |
|   |                                     |   |                                     |  |                                     |

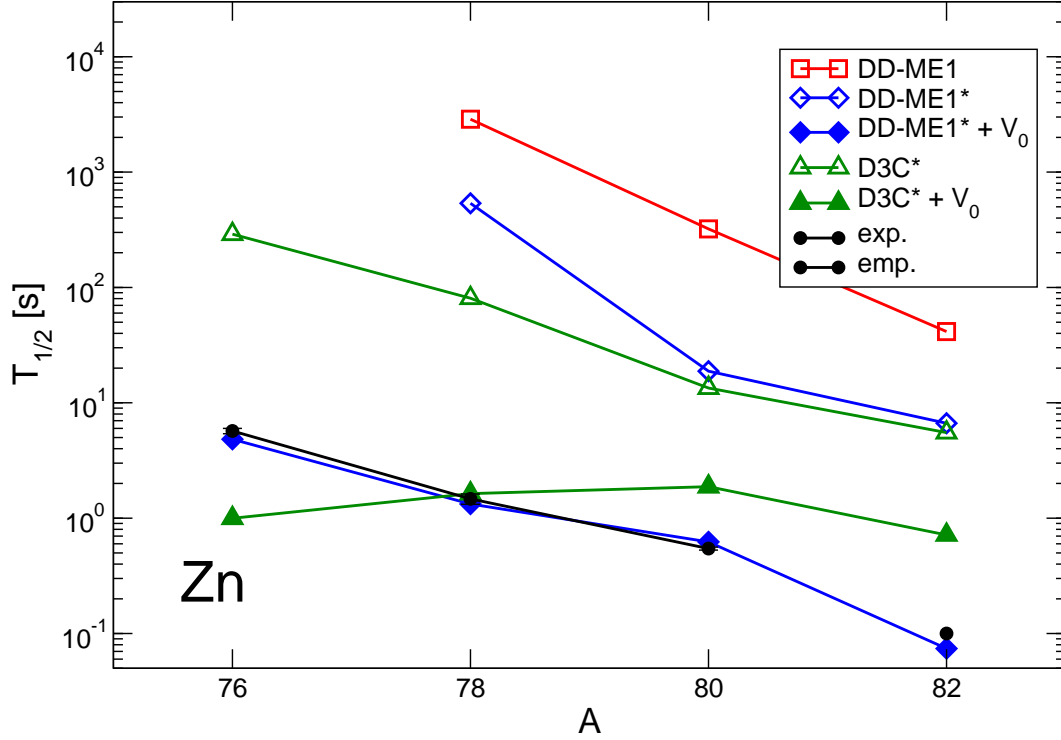


Figure 3.3: Half-lives of zinc isotopes calculated with various interactions. Open symbols denote values obtained without  $T = 0$  residual interaction, while full symbols denote values with additional interaction. Strength of the residual pairing is  $V_0 = 330$  MeV for the DD-ME1\* interaction, and  $V_0 = 300$  MeV for the momentum-dependent D3C\* interaction. Experimental values taken from Ref. [60]. No experimental value is available for  $^{82}\text{Zn}$ , so an empirical value was used.

theoretical half-lives of the heavier Sn isotopes show a pronounced dependence on the  $T = 0$  pairing strength. For  $V_0 = 225$  MeV the calculated half-lives are only slightly longer than the experimental values. This is easily explained by the fact that in tin isotopes beyond  $^{132}\text{Sn}$  neutrons begin to occupy the  $\nu 1h_{9/2}$  single-particle level, and this enables the back spin-flip transition  $\nu 1h_{9/2} \rightarrow \pi 1h_{11/2}$ . The occupation probabilities of the  $\nu 1h_{9/2}$  single-particle level for the Sn and Te isotopes are included in Table 3.3. Because the neutron level  $\nu 1h_{9/2}$  has low occupancy, the  $T = 0$  pairing produces a very strong effect on the  $\pi 1h_{11/2}(\nu 1h_{9/2})^{-1}$  configuration, and reduces the calculated half-lives to the experimental values.

This effect is further illustrated in Fig. 3.6, where the calculated half-lives of the Te isotopes are plotted, in comparison with available experimental data. In this case, the choice  $V_0 = 225$  MeV results in half-lives that are even somewhat shorter than the experimental values. This is related to the fact that the calculated energy spacing between the  $\nu 1h_{9/2}$  and  $\pi 1h_{11/2}$  states in  $^{132}\text{Sn}$

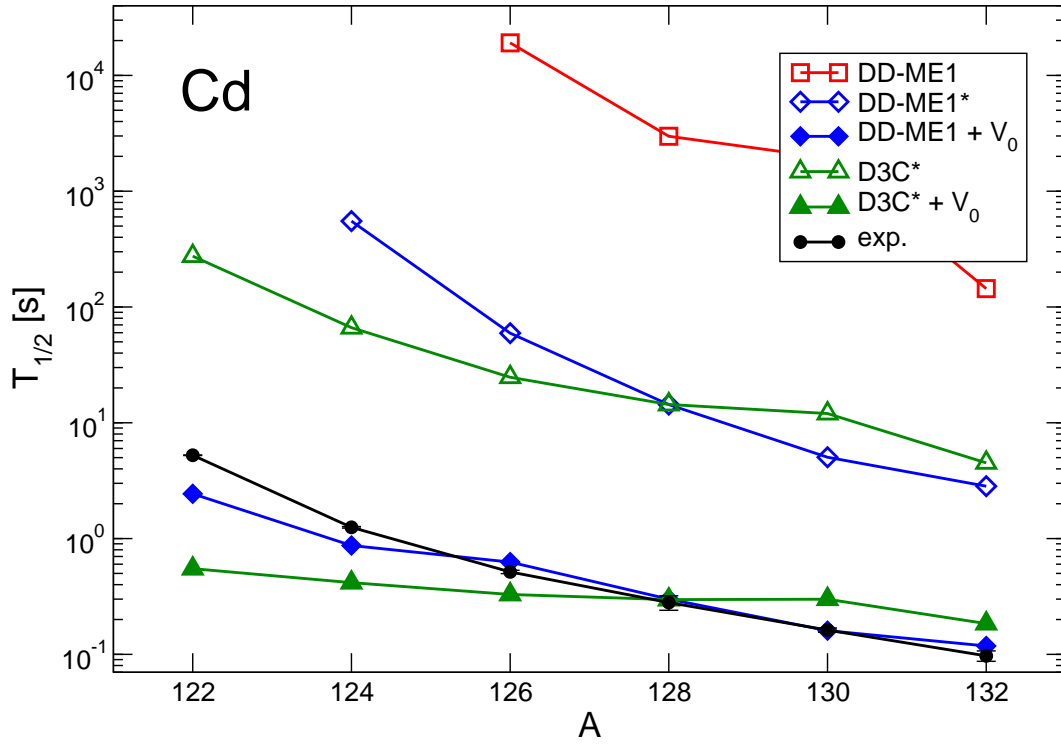


Figure 3.4: Half-lives of cadmium isotopes calculated with various interactions. Open symbols denote values obtained without  $T = 0$  residual interaction, while full symbols denote values with additional interaction. Strength of the residual pairing is  $V_0 = 225$  MeV for the DD-ME1\* interaction, and  $V_0 = 235$  MeV for the momentum-dependent D3C\* interaction. Experimental values taken from Ref. [60].

is larger than the experimental value. A slightly lower value of the  $T = 0$  pairing strength ( $V_0 = 200$  MeV) accurately reproduces the half-lives of the Te isotopes.



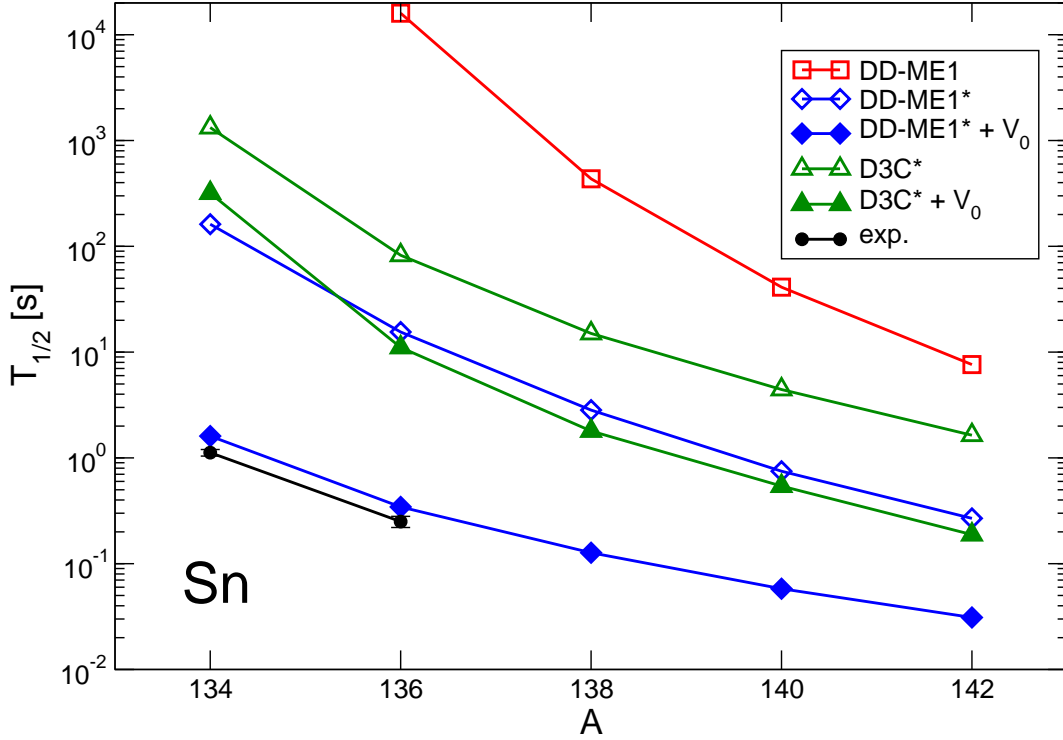


Figure 3.5: Half-lives of tin isotopes calculated with various interactions. Open symbols denote values obtained without  $T = 0$  residual interaction, while full symbols denote values with additional interaction. Strength of the residual pairing is  $V_0 = 225$  MeV for the DD-ME1\* interaction, and  $V_0 = 235$  MeV for the momentum-dependent D3C\* interaction. Experimental values taken from Ref. [60].

Table 3.3: Occupation probabilities of the  $\nu 1h_{9/2}$  single-particle state for the ground-states of the Sn and Te isotopes.

| Sn  |                      | Te  |                      |
|-----|----------------------|-----|----------------------|
| A   | $v_{\nu 1h_{9/2}}^2$ | A   | $v_{\nu 1h_{9/2}}^2$ |
| 134 | 0.024                | 136 | 0.035                |
| 136 | 0.054                | 138 | 0.077                |
| 138 | 0.092                | 140 | 0.129                |
| 142 | 0.142                | 142 | 0.192                |
| 144 | 0.203                | 144 | 0.263                |
| 146 | 0.271                | 146 | 0.339                |

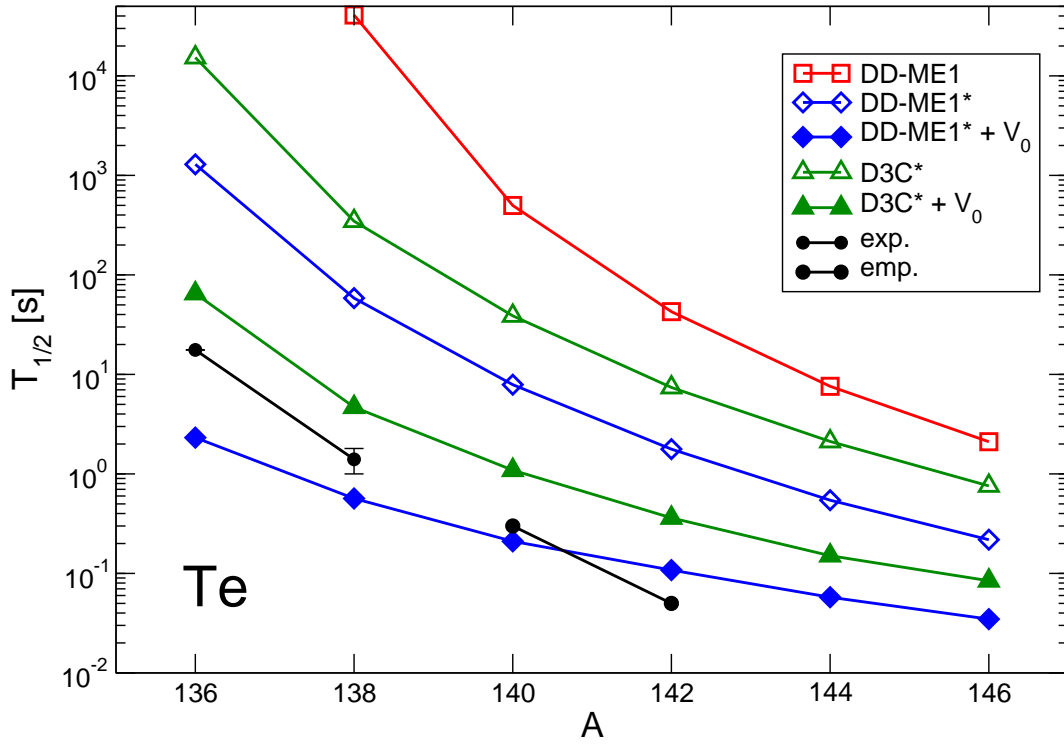


Figure 3.6: Half-lives of tellurium isotopes calculated with various interactions. Open symbols denote values obtained without  $T = 0$  residual interaction, while full symbols denote values with additional interaction. Strength of the residual pairing is  $V_0 = 225$  MeV for the DD-ME1\* interaction, and  $V_0 = 235$  MeV for the momentum-dependent D3C\* interaction. Experimental values taken from Ref. [60].



# Chapter 4

## Nuclear semi-leptonic weak-interaction processes

The latest theoretical and computational advances in nuclear structure modeling have also had a strong impact on nuclear astrophysics. More and more often calculations of stellar nucleosynthesis, nuclear aspects of supernova collapse and explosion, and neutrino-induced reactions are based on microscopic global predictions for the nuclear ingredients rather than on oversimplified phenomenological approaches. The nuclear input for astrophysics calculations necessitates the properties of thousands of nuclei far from stability, including the characteristics of strong electromagnetic and weak interaction processes. Most of these nuclei, especially on the neutron-rich side, are not accessible in experiments and, therefore, many nuclear astrophysics calculations crucially depend on accurate theoretical predictions for the nuclear masses, bulk properties, nuclear excitations,  $(n, \gamma)$  and  $(\gamma, n)$  rates,  $\alpha$ - and  $\beta$ -decay half-lives, fission probabilities, electron and neutrino capture rates, and so on.

A unified description of semileptonic weak interaction processes in nuclei, i.e. the  $\beta$ -decay, charged-lepton capture and neutrino capture can be obtained in close analogy to the theory of electron scattering. The conserved vector current (CVC) theory equates half of the weak interaction matrix elements, those coming from the vector current, with those measured in electron scattering. Using the weak interaction Hamiltonian written in the current-current form, one can obtain a general expression for the matrix element of the Hamiltonian valid for all semi-leptonic processes. Reaction rate for a particular process then follows from the Fermi Golden rule. To successfully combine the theoretical description with a particular microscopic approach and extend it to regions of unknown nuclei far from stability, it is necessary to perform extensive tests and compare results with available data. Reliable prediction of weak interaction rates, in particular, requires a fully consistent description of the structure of the ground state and multipole excitations.

Calculated  $\beta$ -decay half-lives are very sensitive to single-particle structure

of the ground-state, but due to small momentum transfer they can only test excitations of lowest multipoles. Higher multipoles are excited in neutrino-nucleus reactions in the low-energy range below 100 MeV, and these reactions at low energies play an important role in many phenomena in nuclear and particle physics, as well as astrophysics. These reactions present extremely subtle physical processes, not only because they involve the weak interaction but also because they are very sensitive to the structure of nuclear ground states and excitations, i.e., to the solution of the nuclear many-body problem that includes the strong and electromagnetic interactions. The use of microscopic nuclear structure models in a consistent theoretical framework is therefore essential for a quantitative description of neutrino-nucleus reactions [7]. Detailed predictions of neutrino-nucleus cross sections are crucial for the interpretation of neutrino experiments and the detection of neutrinos produced in supernova explosions. Neutrino-nucleus reactions that occur in a type II supernova could also contribute to the nucleosynthesis [3], but data on cross sections are necessary for a more complete understanding of this process, as well as the supernova dynamics.

Many more data is available for total muon capture rates. Muon capture on stable nuclei has been studied in details since many years, both experimentally and theoretically [6, 61]. In this process the momentum transfer is of the order of the muon mass and, therefore, the calculation of total muon capture rates presents an excellent test of models that are also used in studies of low-energy neutrino-nucleus reactions.

## 4.1 Formalism of weak interaction processes

In the interaction representation, fermion fields take the following form

$$\Psi(\mathbf{x}) = \frac{1}{\sqrt{V}} \sum_{\mathbf{k}\lambda} (a_{\mathbf{k}\lambda} u(\mathbf{k}\lambda) e^{i\mathbf{k}\cdot\mathbf{x}} + b_{\mathbf{k}\lambda}^{\dagger} v(-\mathbf{k}\lambda) e^{-i\mathbf{k}\cdot\mathbf{x}}). \quad (4.1)$$

In this expression  $a$  destroys a lepton,  $b^{\dagger}$  creates an antilepton, and  $\lambda$  denotes the helicity with respect to the accompanying momentum variable.

In weak interactions, massless leptons couple through the following two-component fields

$$\phi = \frac{1}{2} (1 + \gamma_5) \psi. \quad (4.2)$$

This expression implies that the lepton coupling terms in the weak Hamiltonian take the following form

$$\bar{\phi}_a O_i \phi_b = \frac{1}{4} \bar{\psi}_a (1 - \gamma_5) O_i (1 + \gamma_5) \psi_b. \quad (4.3)$$

This expression vanishes for scalar, pseudoscalar and tensor couplings of the form  $O_i = 1, \gamma_5, \sigma_{\mu\nu}$ ; and in the case of vector and axial-vector interactions

$O_i = \gamma_\mu, \gamma_\mu \gamma_5$  the coupling is unique

$$\bar{\phi}_a O_i \phi_b = \frac{1}{4} \bar{\psi}_a (1 - \gamma_5) \gamma_\mu (1 + \gamma_5) \psi_b = \frac{1}{2} \bar{\psi}_a \gamma_\mu (1 + \gamma_5) \psi_b. \quad (4.4)$$

To include other leptons the lepton current in the Hamiltonian is generalized to

$$j_\lambda^{(-)}(\text{leptonic}) = i \sum_{l=e,\mu,\tau} \bar{\psi}_l \gamma_\mu (1 + \gamma_5) \psi_{\nu_l}, \quad (4.5)$$

with the total current having both a hadronic and a leptonic part

$$\mathcal{J}_\lambda^{(-)} = \mathcal{J}_\lambda(\text{hadronic}) + j_\lambda. \quad (4.6)$$

The adjoint of the above current describes weak processes where the charge is raised

$$\mathcal{J}_\lambda^{(+)} \equiv \left( \mathcal{J}_1^{(-)+}, \mathcal{J}_2^{(-)+}, \mathcal{J}_3^{(-)+}, +i\mathcal{J}_0^{(-)+} \right) \quad (4.7)$$

It is then an empirical fact that all charge-changing weak interactions can be described through a universal current-current interaction of the currents in Eqs. (4.6) and (4.7)

$$\mathcal{H}_W = -\frac{G}{\sqrt{2}} \mathcal{J}_\lambda^{(+)} \mathcal{J}_\lambda^{(-)}, \quad (4.8)$$

where  $G$  is the Fermi constant. It can be determined experimentally from muon decay and is equal to

$$G_\mu = \frac{1.0267 \cdot 10^{-5}}{m_p^2} \quad (4.9)$$

Using only Lorentz, parity and isospin invariance of the nuclear interaction, a general form of the single-nucleon matrix elements can be obtained.

$$\langle p' | J_\mu^{(-)} | p \rangle = \frac{i}{V} \bar{u}(p') [F_1 \gamma_\mu + F_2 \sigma_{\mu\nu} q_\nu + iF_S q_\mu] \tau_- u(p) \quad (4.10)$$

$$\langle p' | J_{\mu 5}^{(-)} | p \rangle = \frac{i}{V} \bar{u}(p') [F_A \gamma_5 \gamma_\mu - iF_P \gamma_5 q_\mu - F_T \gamma_5 \sigma_{\mu\nu} q_\nu] \tau_- u(p) \quad (4.11)$$

where  $q \equiv p - p'$ ,  $p^2 = p'^2 = -m^2$  and all the form factors are functions of momentum transfer as  $F_i(q^2)$ . The conserved vector current theory states that the Lorentz vector part of the weak charge-changing current is obtained from the other spherical isospin components of the same isovector operator that appears in the electromagnetic current. As a consequence, one can relate matrix elements of the Lorentz vector part of the charge-changing weak currents to those of the isovector part of the electromagnetic current. The CVC theory provides relations between the weak and electromagnetic formfactors of the nucleon,

$$F_{1,2} = F_{1,2}^V \quad (4.12)$$

with

$$F_1^V(0) = 1 \quad (4.13)$$

$$2mF_2^V(0) = \lambda_p - \lambda_n = 3.706 \quad (4.14)$$

where  $\lambda_p$  and  $\lambda_n$  are the proton and neutron anomalous magnetic moments, respectively.

To examine the axial-vector part of the interaction, one must turn to pion processes. There is a one-pion exchange process in the lepton-nucleon scattering which produces a pole in the scattering amplitude. Evaluation of the S-matrix gives the following form of the pseudoscalar form factor

$$F_P = -\frac{\sqrt{2}g_\pi F_\pi}{q^2 + m_\pi^2} \quad (4.15)$$

The value of the constant  $F_\pi$  can be determined from pion decay process  $\pi^- \rightarrow l^- + \bar{\nu}_l$ . The decay rate is given by

$$\omega = \frac{G^2 F_\pi^2}{8\pi} m_\pi^2 \left(\frac{m_l}{m_\pi}\right)^2 \left(1 - \frac{m_l}{m_\pi}\right)^2 m_\pi. \quad (4.16)$$

A comparison with experiment gives the value as

$$F_\pi \approx 0.92m_\pi \quad (4.17)$$

The final form factor  $F_A$  can be determined using the partially conserved axial-vector current (PCAC) postulate which states

$$\frac{\partial J_{\lambda 5}^V(x)}{\partial x_\lambda} = O(m_\pi^2). \quad (4.18)$$

In the limit of  $m_\pi \rightarrow 0$  the current is fully conserved. Evaluating the single-nucleon matrix element of the divergence of the axial-vector current and using the results obtained in the pion processes, the Goldberger-Treiman relation is obtained

$$-2mF_A = \sqrt{2}g_\pi F_\pi \quad (4.19)$$

Combining Eqs. (4.15) and (4.19) provides

$$F_P(q^2) = \frac{2mF_A(0)}{q^2 + m_\pi^2}, \quad (4.20)$$

where  $F_A(0)$  is determined from decay of the neutron as

$$F_A(0) = -1.23 \pm 0.01 \quad (4.21)$$

All form factors except for the pseudoscalar one have the momentum dependence of the nucleon charge form factor [62].

Finally, due to a theorem of Weinberg [63], if the currents have the same transformation properties under time reversal, parity, charge conjugation and isospin as the bare current then

$$F_S = F_T = 0. \quad (4.22)$$

## 4.2 Multipole analysis of the leptonic matrix element

Starting from the weak interaction Hamiltonian written in a more convenient form

$$\mathcal{H}_W = -\frac{G}{\sqrt{2}} \int d^3x \mathcal{J}_\mu(\mathbf{x}) j_\mu^{\text{leptonic}}(\mathbf{x}) \quad (4.23)$$

its matrix element reads

$$\langle f | \mathcal{H}_W | i \rangle = -\frac{G}{\sqrt{2}} l_\mu \int d^3x e^{-i\mathbf{q}\cdot\mathbf{x}} \langle f | \mathcal{J}_\mu(\mathbf{x}) | i \rangle \quad (4.24)$$

where

$$q = k_2 \pm k_1. \quad (4.25)$$

Here the + sign is for neutrino or charged lepton capture, and the – sign is for decay.  $k_2$  and  $k_1$  are the momenta of the outgoing and incoming particles, respectively, except for the case of decay where  $k_2$  is the momentum of the particle and  $k_1$  momentum of the antiparticle. Here two assumptions are made

- target is well localized in space enabling partial integration on the transition matrix elements, neglecting the vanishing contribution at infinity,
- initial and final states of the target nucleus have definite angular momentum and parity.

By defining a complete orthonormal set of unit vectors with z-axis in the direction of momentum transfer, any vector can be expanded into its spherical components as

$$\mathbf{l} = \sum_{\lambda=0,\pm 1} l_\lambda \mathbf{e}_\lambda^+ \Rightarrow l_\lambda = \mathbf{e}_\lambda \cdot \mathbf{l}. \quad (4.26)$$

Combining this result with the multipole expansion of the exponential function ( $\kappa = |\mathbf{q}|$ )

$$e^{i\mathbf{q}\cdot\mathbf{x}} = \sum_{J=0}^{\infty} \sqrt{4\pi(2J+1)} j_J(\kappa x) Y_{J0}(\Omega_x), \quad (4.27)$$

the expansion

$$\begin{aligned} \mathbf{e}_{\mathbf{q}\lambda} e^{i\mathbf{q}\cdot\mathbf{x}} &= -\frac{i}{\kappa} \sum_{J=0}^{\infty} \sqrt{4\pi(2J+1)} i^J \nabla (j_J(\kappa x) Y_{J0}(\Omega_x)), \quad \lambda = 0 \\ &= -\sum_{J \geq 1}^{\infty} \sqrt{2\pi(2J+1)} i^J \left[ \lambda j_J(\kappa x) \mathcal{Y}_{JJ1}^\lambda + \frac{1}{\kappa} \nabla \times (j_J(\kappa x) \mathcal{Y}_{JJ1}^\lambda) \right], \quad \lambda = \pm 1 \end{aligned} \quad (4.28)$$



is obtained. Defining the Coulomb, longitudinal, transverse electric and transverse magnetic multipole tensor operators by

$$\mathcal{M}_{JM}(\kappa) \equiv M_{JM} + M_{JM}^5 = \int d^3x [j_J(\kappa x) Y_{JM}(\Omega_x)] \mathcal{J}_0(\mathbf{x}), \quad (4.29)$$

$$\mathcal{L}_{JM}(\kappa) \equiv L_{JM} + L_{JM}^5 = \frac{i}{\kappa} \int d^3x \{ \nabla [j_J(\kappa x) Y_{JM}(\Omega_x)] \} \cdot \mathcal{J}(\mathbf{x}), \quad (4.30)$$

$$\mathcal{T}_{JM}^{\text{el}}(\kappa) \equiv T_{JM}^{\text{el}} + T_{JM}^{\text{el},5} = \frac{1}{\kappa} \int d^3x [\nabla \times j_J(\kappa x) \mathbf{r} \mathcal{Y}_{JJ_1}^M(\Omega_x)] \cdot \mathcal{J}(\mathbf{x}) \quad (4.31)$$

$$\mathcal{T}_{JM}^{\text{mag}}(\kappa) \equiv T_{JM}^{\text{mag}} + T_{JM}^{\text{mag},5} = \int d^3x [j_J(\kappa x) \mathbf{r} \mathcal{Y}_{JJ_1}^M(\Omega_x)] \cdot \mathcal{J}(\mathbf{x}). \quad (4.32)$$

The index “5” denotes terms arising from the axial-vector part of the current. Using these operators the matrix element of the Hamiltonian can be expressed as

$$\begin{aligned} \langle f | \mathcal{H}_W | i \rangle &= -\frac{G}{\sqrt{2}} \left\langle f \left| \left\{ -\sum_{J \geq 1} \sqrt{2\pi(2J+1)} (-i)^J \sum_{\lambda=\pm 1} l_\lambda [\lambda \mathcal{T}_{J-\lambda}^{\text{mag}}(\kappa) + \mathcal{T}_{J-\lambda}^{\text{el}}(\kappa)] \right. \right. \right. \\ &\quad \left. \left. \left. + \sum_{J \geq 0} \sqrt{4\pi(2J+1)} (-i)^J [l_3 \mathcal{L}_{J0}(\kappa) - l_0 \mathcal{M}_{J0}(\kappa)] \right\} \right| i \right\rangle. \end{aligned} \quad (4.33)$$

Employing the Wigner-Eckart theorem, summing over final target states and averaging over initial states, and using the relation

$$\sum_{\lambda=\pm 1} l_\lambda l_\lambda^* |a + \lambda b|^2 = (|a|^2 + |b|^2)^2 (\mathbf{l} \cdot \mathbf{l}^* - l_3 l_3^*) - i (\mathbf{l} \times \mathbf{l}^*)_3 2\text{Re } a^* b \quad (4.34)$$

a general expression for the matrix element of the Hamiltonian is obtained valid for all semileptonic nuclear processes

$$\begin{aligned} \frac{1}{2J_i + 1} \sum_{M_i, M_f} |\langle f | \mathcal{H}_W | i \rangle|^2 &= \frac{G^2}{2} \frac{4\pi}{2J_i + 1} \\ &\times \left\{ \sum_{J \geq 1} \left[ \frac{1}{2} (\mathbf{l} \cdot \mathbf{l}^* - l_3 l_3^*) \left( |\langle J_f || \mathcal{T}_J^{\text{mag}} || J_i \rangle|^2 + |\langle J_f || \mathcal{T}_J^{\text{el}} || J_i \rangle|^2 \right) \right. \right. \\ &- \frac{i}{2} (\mathbf{l} \times \mathbf{l}^*)_3 \left( 2\text{Re} \langle J_f || \mathcal{T}_J^{\text{mag}} || J_i \rangle \langle J_f || \mathcal{T}_J^{\text{mag}} || J_i \rangle^* \right) \left. \right] \\ &+ \sum_{J \geq 0} \left[ l_3 l_3^* |\langle J_f || \mathcal{L}_J || J_i \rangle|^2 + l_0 l_0^* |\langle J_f || \mathcal{M}_J || J_i \rangle|^2 \right. \\ &\left. \left. - 2\text{Re} \left( l_3 l_0^* \langle J_f || \mathcal{L}_J || J_i \rangle \langle J_f || \mathcal{M}_J || J_i \rangle^* \right) \right] \right\} \quad (4.35) \end{aligned}$$

Table 4.1: Lepton traces obtained from lepton matrix elements  $l_\mu$ .

| Summand  | General result <sup>1</sup>   | ERL ( $ \boldsymbol{\beta}  \rightarrow 1$ )  |
|--|---|---|
| $\frac{1}{2}(\mathbf{l} \cdot \mathbf{l}^* - l_3 l_3^*)$ | $1 - (\hat{\boldsymbol{\nu}} \cdot \hat{\mathbf{q}})(\boldsymbol{\beta} \cdot \hat{\mathbf{q}})$  | $\frac{q_\mu^2}{q^2} \cos^2 \frac{\vartheta}{2} + 2 \sin^2 \frac{\vartheta}{2}$   |
| $l_0 l_0^*$  | $1 + \hat{\boldsymbol{\nu}} \cdot \boldsymbol{\beta}$   | $2 \cos^2 \frac{\vartheta}{2}$  |
| $l_3 l_3^*$  | $1 - \hat{\boldsymbol{\nu}} \cdot \boldsymbol{\beta} + 2(\hat{\boldsymbol{\nu}} \cdot \hat{\mathbf{q}})(\boldsymbol{\beta} \cdot \hat{\mathbf{q}})$ | $2 \frac{q_0^2}{q^2} \cos^2 \frac{\vartheta}{2}$  |
| $-l_3 l_0^*$   | $-\hat{\mathbf{q}} \cdot (\hat{\boldsymbol{\nu}} + \boldsymbol{\beta})$   | $-2 \frac{q_0}{ q } \cos^2 \frac{\vartheta}{2}$   |
| $-\frac{i}{2}(\mathbf{l} \times \mathbf{l}^*)_3$         | $-S_1 \hat{\mathbf{q}} \cdot (\hat{\boldsymbol{\nu}} - \boldsymbol{\beta})$   | $2 \frac{S_1 S_3}{ q } \sin \frac{\vartheta}{2} \sqrt{q_\mu^2 \cos^2 \frac{\vartheta}{2} + q^2 \sin^2 \frac{\vartheta}{2}}$ |

Table 4.2: Sign factors for weak processes used in Table 4.1.

| Process               | $S_1$ | $S_3$                        |
|-----------------------|-------|------------------------------|
| Neutrino reaction     | -1    | +1                           |
| Antineutrino reaction | +1    | +1                           |
| Lepton capture        | +1    | -1                           |
| $\beta^-$ -decay      | -1    | $\text{sgn}(\epsilon - \nu)$ |
| $\beta^+$ -decay      | +1    | $\text{sgn}(\epsilon - \nu)$ |

To obtain the reaction rates of semileptonic weak processes, a sum over lepton spins is performed. The results of this summation are given in Table 4.1. The sign factors  $S_1$  and  $S_3$  that appear in the lepton traces are specific to a particular process, and are given in Table 4.2.

To make use of this relation, an actual form of the reduced matrix elements of the multipole operators is required. A derivation is given for the case where the nuclear current operator is taken to be the sum of contributions of individual nucleons. In the approximation that nucleons in the target move nonrelativistically, the four-component Dirac wave function reads

$$u(\mathbf{p}, \lambda) \approx \begin{pmatrix} \chi_\lambda \\ \frac{\boldsymbol{\sigma} \cdot \mathbf{p}}{2m} \chi_\lambda \end{pmatrix} \quad (4.36)$$

where  $\chi_\lambda$  are two-component Pauli spinors, and the component of the  $\boldsymbol{\sigma}$  operators are Pauli matrices. Substituting this wave function into expressions (4.10) and (4.11) and evaluating the result to order  $1/m$  provides

$$\langle \mathbf{p}', \lambda', \rho' | \mathcal{J}_\mu^{(-)}(0) | \mathbf{p} \lambda \rho \rangle = \frac{1}{V} \chi_{\lambda'}^+ \eta_{\rho'}^+ \left[ M_\mu - q_\mu \left( F_P \frac{\boldsymbol{\sigma} \cdot \mathbf{q}}{2m} \right) \right] \tau_{-\eta_\rho} \chi_\lambda, \quad (4.37)$$

where the time-like and space-like components of the operator  $M_\mu$  are

$$M_0 = F_1 + \boldsymbol{\sigma} \cdot \left[ \left( F_A \frac{2\mathbf{p} - \mathbf{q}}{2m} \right) \right], \quad (4.38)$$

$$\mathbf{M} = F_A \boldsymbol{\sigma} - (F_1 + 2mF_2) \frac{i\boldsymbol{\sigma} \times \mathbf{q}}{2m} + F_1 \left( \frac{2\mathbf{p} - \mathbf{q}}{2m} \right). \quad (4.39)$$

This single-particle operator can be broken down into seven fundamental operators [64]

$$M_J^M(\mathbf{x}) = j_J(\kappa x) Y_{JM}(\Omega_x), \quad (4.40)$$

$$\Delta_{JM}(\mathbf{x}) = \mathbf{M}_{JJ}^M(\mathbf{x}) \cdot \frac{1}{\kappa} \nabla, \quad (4.41)$$

$$\Delta'_{JM}(\mathbf{x}) = - \left[ \frac{1}{\kappa} \nabla \times \mathbf{M}_{JJ}^M(\mathbf{x}) \right] \cdot \frac{1}{\kappa} \nabla, \quad (4.42)$$

$$\Sigma_{JM}(\mathbf{x}) = \mathbf{M}_{JJ}^M(\mathbf{x}) \cdot \boldsymbol{\sigma}, \quad (4.43)$$

$$\Sigma'_{JM}(\mathbf{x}) = -i \left[ \frac{1}{\kappa} \nabla \times \mathbf{M}_{JJ}^M(\mathbf{x}) \right] \cdot \boldsymbol{\sigma}, \quad (4.44)$$

$$\Sigma''_{JM}(\mathbf{x}) = \left[ \frac{1}{\kappa} \nabla M_J^M(\mathbf{x}) \right] \cdot \boldsymbol{\sigma}, \quad (4.45)$$

$$\Omega_{JM}(\mathbf{x}) = M_J^M(\mathbf{x}) \boldsymbol{\sigma} \cdot \frac{1}{\kappa} \nabla, \quad (4.46)$$

where  $\mathbf{M}_{JL}^M(\mathbf{x}) = j_L(\kappa x) \mathbf{Y}_{JL1}^M(\Omega_x)$ , and  $\mathbf{Y}_{JL1}^M$  are the vector spherical harmonics. Reduced single-particle matrix elements in the spherical harmonic oscillator basis are given in Ref. [61].

Using these seven basic operators, the expressions for the vector and axial-vector parts of the multipole operators in Eqs. (4.29) – (4.32) can be written down as

$$M_{JM}(\mathbf{x}) = F_1^V M_J^M(\mathbf{x}), \quad (4.47)$$

$$M_{JM}^5(\mathbf{x}) = -i \frac{\kappa}{m} \left[ F_A \Omega_{JM}(\mathbf{x}) + \frac{1}{2} (F_A - \lambda m F_P) \Sigma''_{JM}(\mathbf{x}) \right], \quad (4.48)$$

$$L_{JM}(\mathbf{x}) = \frac{q_0}{\kappa} F_1^V M_{JM}(\mathbf{x}), \quad (4.49)$$

$$L_{JM}^5(\mathbf{x}) = i \left[ F_A - \frac{1}{2} \lambda' \left( \frac{\kappa}{m} \right)^2 m F_P \right] \Sigma''_{JM}(\mathbf{x}), \quad (4.50)$$

$$T_{JM}^{\text{el}}(\mathbf{x}) = \frac{\kappa}{m} \left[ F_1^V \Delta'_{JM}(\mathbf{x}) + \frac{1}{2} \mu^V \Sigma_{JM}(\mathbf{x}) \right], \quad (4.51)$$

$$T_{JM}^{\text{el},5}(\mathbf{x}) = i F_A \Sigma'_{JM}(\mathbf{x}), \quad (4.52)$$

$$T_{JM}^{\text{mag}}(\mathbf{x}) = -i \frac{\kappa}{m} \left[ F_1^V \Delta_{JM}(\mathbf{x}) - \frac{1}{2} \mu^V \Sigma'_{JM}(\mathbf{x}) \right], \quad (4.53)$$

$$T_{JM}^{\text{mag},5}(\mathbf{x}) = F_A \Sigma_{JM}(\mathbf{x}). \quad (4.54)$$

Here, the parameters  $\lambda$  and  $\lambda'$  differ depending on the process in question. For neutrino processes  $\lambda = -q_0/m$  and  $\lambda' = 1$ , for muon capture  $\lambda = m_\mu/m$  and  $\lambda' = 0$  and for all electron processes both  $\lambda$  and  $\lambda'$  are equal to 0.

Having derived the most general expression for the matrix element of the weak interaction Hamiltonian, including summation over final spins and averaging over initial spins, particular processes can be examined.

### 4.3 Muon capture

The capture of a negative muon from the atomic  $1s$  orbit on a nucleus  $(Z, N)$

$$\mu^- + (Z, N) \longrightarrow \nu_\mu + (Z - 1, N + 1)^* , \quad (4.55)$$

presents a simple semi-leptonic reaction that proceeds via the charged current of the weak interaction. Detailed expressions for the reaction rates and the transition matrix elements can be found in Refs. [64, 61, 5]. The capture rate reads

$$\omega_{fi} = \frac{\Omega \nu^2}{2\pi} \sum_{\text{lepton spins}} \frac{1}{2J_i + 1} \sum_{M_i} \sum_{M_f} |\langle f | \hat{H}_W | i \rangle|^2 , \quad (4.56)$$

where  $\Omega$  denotes the quantization volume and  $\nu$  is the muon neutrino energy. The expression for the muon capture rate is given by

$$\omega_{fi} = \frac{2G^2 \nu^2}{(1 + \nu/M_T)} \frac{1}{2J_i + 1} \left\{ \sum_{J=0}^{\infty} \left| \langle J_f \parallel \phi_{1s} (\hat{\mathcal{M}}_J - \hat{\mathcal{L}}_J) \parallel J_i \rangle \right|^2 \right. \\ \left. + \sum_{J=1}^{\infty} \left| \langle J_f \parallel \phi_{1s} (\hat{\mathcal{T}}_J^{el} - \hat{\mathcal{T}}_J^{mag}) \parallel J_i \rangle \right|^2 \right\} \quad (4.57)$$

where  $G$  is the weak coupling constant, the phase-space factor  $(1 + \nu/M_T)^{-1}$  accounts for the nuclear recoil, and  $M_T$  is the mass of the target nucleus. The nuclear transition matrix elements between the initial state  $|J_i\rangle$  and final state  $|J_f\rangle$ , correspond to the charge  $\hat{\mathcal{M}}_J$ , longitudinal  $\hat{\mathcal{L}}_J$ , transverse electric  $\hat{\mathcal{T}}_J^{EL}$ , and transverse magnetic  $\hat{\mathcal{T}}_J^{MAG}$  multipole operators. The neutrino energy is determined by the energy conservation relation

$$m_\mu - \epsilon_b + E_i = E_f + \nu_f , \quad (4.58)$$

where  $\epsilon_b$  is the binding energy of the muonic atom.

For each nucleus the muon wave function and binding energy are calculated as solutions of the Dirac equation with the Coulomb potential determined by the self-consistent ground-state charge density. However, while the RHB single-nucleon equations are solved by expanding nucleon spinors and meson fields in terms of eigenfunctions of a spherically symmetric harmonic oscillator

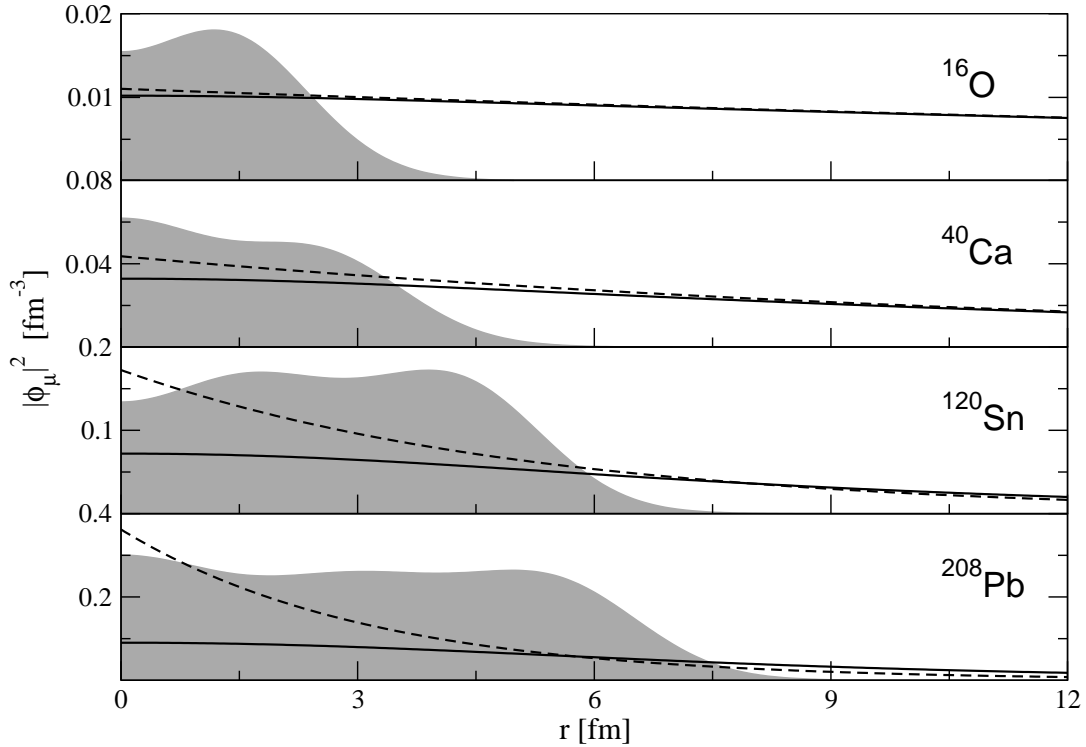


Figure 4.1: Square of the wave function of a muon in a  $1s$  state for  $^{16}\text{O}$ ,  $^{40}\text{Ca}$ ,  $^{120}\text{Sn}$  and  $^{208}\text{Pb}$ . Dashed lines denote wave functions of a muon in a potential of pointlike charge  $Z$ , while the full line denotes wave functions obtained by performing the full finite element method calculation for the self-consistent Coulomb potential. Shaded area indicates charge density distribution in a particular nucleus scaled by an arbitrary factor.

potential, the same method could not be used for the muon wave functions. The reason, of course, is that the muon wave functions extend far beyond the surface of the nucleus and, even using a large number of oscillator shells, solutions expressed in terms of harmonic oscillator basis functions do not converge. The Dirac equation for the muon is therefore solved in coordinate space using the method of finite elements with B-spline shape functions [65, 66]. As an illustration, in Fig. 4.1 the square of the  $1s$  muon wave functions for  $^{16}\text{O}$ ,  $^{40}\text{Ca}$ ,  $^{120}\text{Sn}$  and  $^{208}\text{Pb}$  is plotted. The solutions that correspond to self-consistent ground-state charge densities are compared with eigenfunctions of the Coulomb potential for the corresponding point-charge  $Z$ . For light nuclei the radial dependence of the  $1s$  muon wave function is not very different from that of the point-charge Coulomb potential. With the increase of  $Z$  the muon is pulled into the nuclear Coulomb potential, and thus the magnitude of the  $1s$  density inside the nucleus is reduced with respect to the point-charge value. To test our calculation of muon orbitals in the nuclear Coulomb potential, in

Table 4.3: Calculated muon transition energies in tin isotopes (in units of keV), compared with available data [67].

|                   | $1p_{1/2} - 1s_{1/2}$ |       | $1p_{3/2} - 1s_{1/2}$ |       |
|-------------------|-----------------------|-------|-----------------------|-------|
|                   | exp.                  | calc. | exp.                  | calc. |
| $^{112}\text{Sn}$ | 3432                  | 3439  | 3478                  | 3485  |
| $^{114}\text{Sn}$ | 3426                  | 3432  | 3471                  | 3478  |
| $^{116}\text{Sn}$ | 3420                  | 3427  | 3465                  | 3472  |
| $^{118}\text{Sn}$ |                       | 3421  |                       | 3466  |
| $^{120}\text{Sn}$ | 3408                  | 3415  | 3454                  | 3460  |
| $^{122}\text{Sn}$ |                       | 3409  |                       | 3454  |
| $^{124}\text{Sn}$ | 3400                  | 3404  | 3445                  | 3450  |

Table 4.4: Calculated muon transition energies in  $^{208}\text{Pb}$  (in units of keV), in comparison with experimental values [68].

| $^{208}\text{Pb}$     | exp. | calc. |
|-----------------------|------|-------|
| $1p_{3/2} - 1s_{1/2}$ | 5963 | 5956  |
| $1p_{1/2} - 1s_{1/2}$ | 5778 | 5773  |
| $1d_{3/2} - 1p_{1/2}$ | 2642 | 2633  |
| $1d_{5/2} - 1p_{3/2}$ | 2501 | 2493  |
| $1d_{3/2} - 1p_{3/2}$ | 2458 | 2450  |

Tables 4.3 and 4.4 the muon transition energies in Sn isotopes and in  $^{208}\text{Pb}$ , respectively, are compared with available data [67, 68]. The calculated transition energies are in good agreement with experimental values.

The effect of the finite distribution of ground-state charge densities on the calculated muon capture rates is illustrated in Fig. 4.2. For a large set of nuclei from  $^{12}\text{C}$  to  $^{244}\text{Pu}$ , the ratio between calculated and experimental muon capture rates is plotted. This ratio is  $\leq 1.5$  for all nuclei when the muon  $1s$  wave functions are determined by self-consistent ground-state charge densities, whereas for point-charge Coulomb potentials one notes a distinct increase with  $Z$ , and  $\omega_{\text{calc.}}/\omega_{\text{exp.}} \geq 4$  for the heaviest systems.

The muon capture rates shown in Fig. 4.2 are calculated with the standard set of free nucleon weak form factors, i.e. the calculation does not include any in-medium quenching of the corresponding strength functions. Even with muon wave functions determined self-consistently by finite-charge densities, the resulting capture rates are larger than the corresponding experimental values by a factor  $\approx 1.2 - 1.4$ . This is in contrast to the results of Ref. [69], where

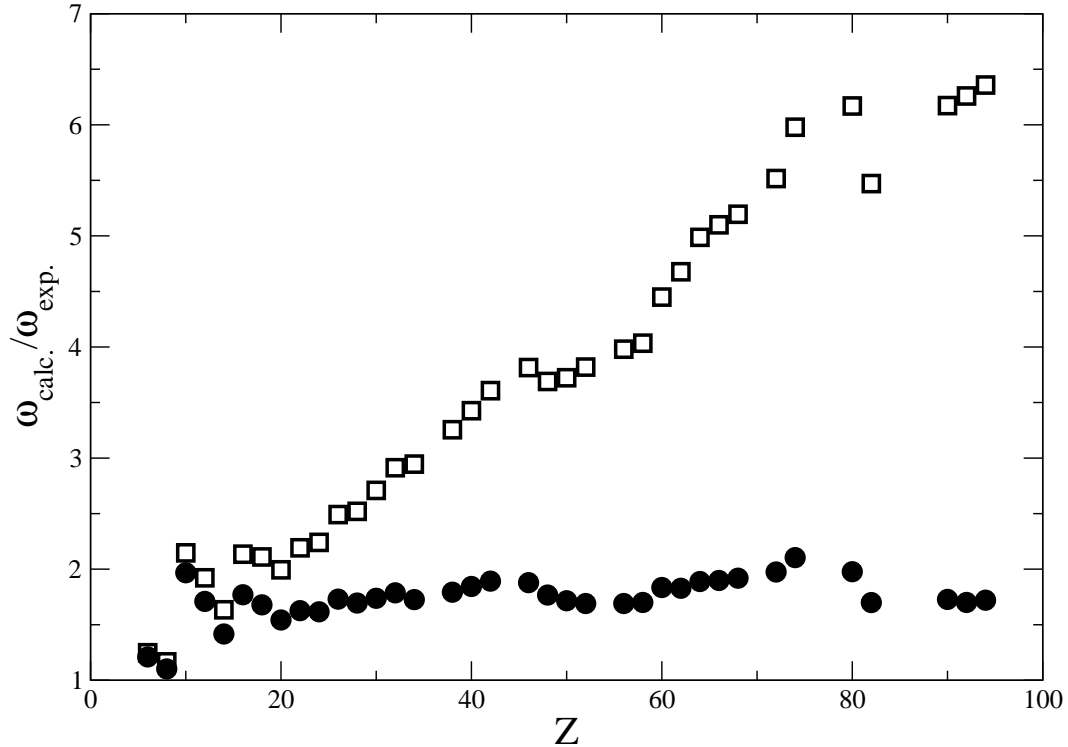


Figure 4.2: Ratio of the calculated and experimental total muon capture rates, as function of the proton number  $Z$ . The theoretical values are calculated with muon  $1s$  wave functions determined by self-consistent ground-state charge densities (filled circle symbols), and by the corresponding point-charge Coulomb potentials (squares).

the experimental values have been reproduced to better than 15% accuracy, using the free-nucleon weak form factors and residual interactions with a mild  $A$  dependency. In fact, it was shown that the calculated rates for the same residual interactions would be significantly below the data if the in-medium quenching of the axial-vector coupling constant is employed to other than the true Gamow-Teller (GT) amplitudes. Consequently, the calculations reported in Ref. [69] were performed with quenching only the GT part of the transition strength by a common factor  $(0.8)^2 = 0.64$ . It was concluded, however, that there is actually no need to apply any quenching to operators that contribute to the muon capture process, especially those involving single-nucleon transitions between major oscillator shells.

As already emphasized in the Introduction, although both calculations are based on the RPA framework, there are important differences between the model of Ref. [69], and the RHB+RQRPA approach employed in the present study. The main difference is probably the fact that the present calculation is fully consistent: for all nuclei both the basis of single-nucleon states and the

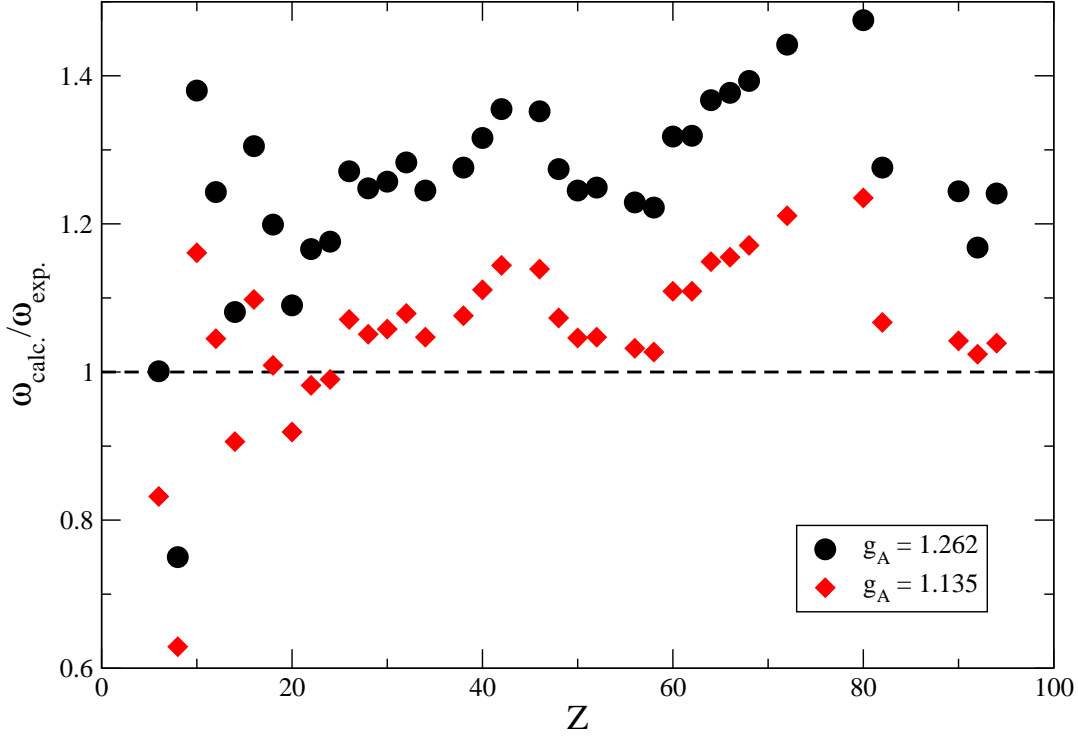


Figure 4.3: Ratio of the calculated and experimental total muon capture rates, as function of the proton number  $Z$ . Circles correspond to rates calculated with the free-nucleon weak form factors [62], and diamonds denote values obtained by quenching the free-nucleon axial-vector coupling constant  $g_A = 1.262$  to  $g_A = 1.135$  for all operators, i.e. in all multipole channels.

multipole response are calculated using the same effective interaction, whereas in Ref. [69] the phenomenological Woods-Saxon potential was adjusted to individual nuclei and the strength of the residual Landau-Migdal force had a mild  $A$ -dependence.

In Fig. 4.3 the ratios of the theoretical and experimental total muon capture rates are compared for two sets of weak form factors. First, the rates calculated with the free nucleon weak form factors [62] (circles), and already shown in Fig. 4.2. The lower rates, denoted by diamonds, are calculated by applying the same quenching  $g_A = 1.262 \rightarrow g_A = 1.135$  to all axial operators, i.e.  $g_A$  is reduced by 10% in all multipole channels. In the latter case the level of agreement is very good, with the mean deviation between theoretical and experimental values of only 6%. The factor 0.9 with which the free-nucleon  $g_A$  is multiplied is chosen in such a way to minimize the deviation from experimental values for spherical, closed-shell medium-heavy and heavy nuclei. On the average the results are slightly better than those obtained in Ref. [69] (cf. Fig. 2 of [69]). Note, however, that in the calculation of Zinner, Langanke and Vogel [69] only the true Gamow-Teller  $0\hbar\omega$  transition strength was



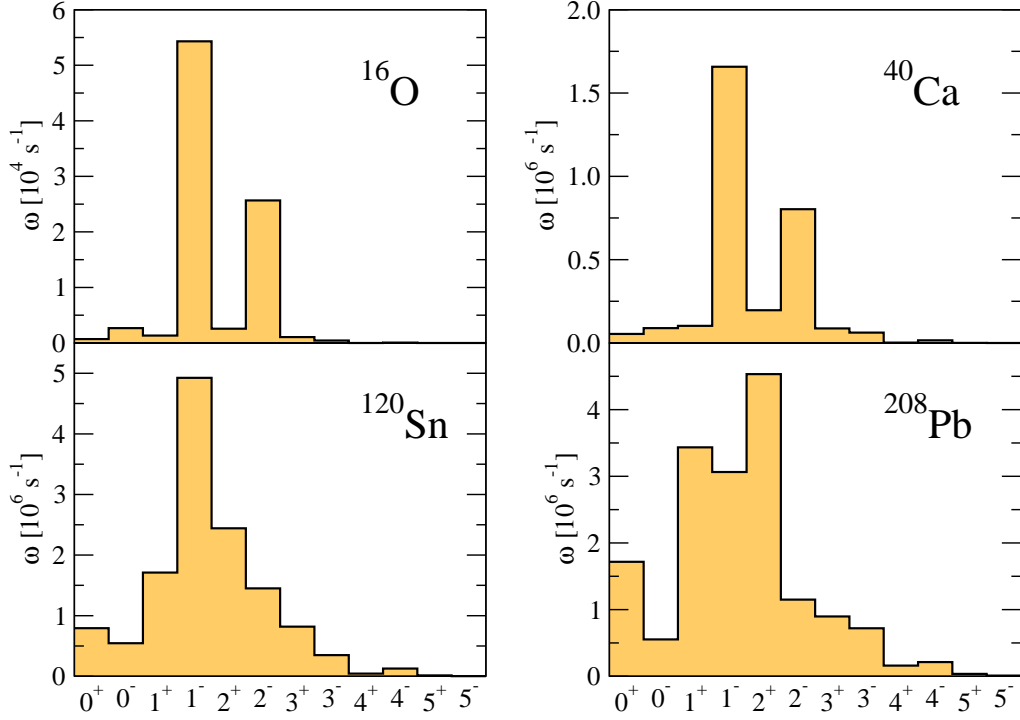


Figure 4.4: Relative contributions of different multipole transitions to the RHB plus RQRPA total muon capture rates in  $^{16}\text{O}$ ,  $^{40}\text{Ca}$ ,  $^{120}\text{Sn}$  and  $^{208}\text{Pb}$ .

quenched, rather than the total strength in the  $1^+$  channel. In the present study considerably better results are obtained when the quenched value of the axial-vector coupling constants is used for all multipole operators. The reason to consider quenching the strength in all multipole channels, rather than just for the GT is, of course, that the axial form factor appears in all four operators Eqs. (4.29 – (4.32) that induce transitions between the initial and final states, irrespective of their multipolarity. Even more importantly, only a relatively small contribution to the total capture rates actually comes from the GT channel  $1^+$ . This is illustrated in Fig. 4.4, where the relative contributions of different multipole transitions to the RHB plus RQRPA muon capture rates in  $^{16}\text{O}$ ,  $^{40}\text{Ca}$ ,  $^{120}\text{Sn}$  and  $^{208}\text{Pb}$  are displayed. For the two lighter  $N = Z$  nuclei the dominant multipole transitions are  $\lambda^\pi = 1^-$  and  $\lambda^\pi = 2^-$  (spin-dipole). For the two heavier nuclei there are also significant contributions of the  $\lambda^\pi = 1^+$  and  $\lambda^\pi = 2^+$ , especially for  $^{208}\text{Pb}$  and for other heavy nuclei. Note that in heavy nuclei the  $\lambda^\pi = 1^+$  multipole represents  $2\hbar\omega$  transitions, rather than the  $0\hbar\omega$  Gamow-Teller transitions.

Returning to Fig. 4.3, with a 10% quenching of the free-nucleon axial-vector coupling constant  $g_A$ , for medium-heavy and heavy nuclei the calculated capture rates are still slightly larger than the corresponding experimental values, with the ratio  $\omega_{\text{calc.}}/\omega_{\text{exp.}}$  typically around 1.1, whereas for several lighter nuclei

considered here this ratio is actually less than 1 (cf. also Table 4.5). Overall the best results, with  $\omega_{\text{calc.}}/\omega_{\text{exp.}} \approx 1$ , are obtained near closed shells. The characteristic arches between closed shells can probably be attributed to deformation effects, not taken into account in our RHB+RQRPA model. In addition to the DD-ME2 interaction, a full calculation of total capture rates from  $^{12}\text{C}$  to  $^{244}\text{Pu}$  was also carried out, using the density- and momentum-dependent relativistic effective interaction D3C\*. In the study of  $\beta$ -decay half-lives of Ref. [70], this interaction was constructed with the aim to enhance the effective (Landau) nucleon mass, and thus improve the RQRPA description of  $\beta$ -decay rates. When D3C\* is used to calculate muon capture rates, some improvement is obtained only locally, for certain regions of  $Z$ , whereas in other regions ( $Z \approx 50$  and  $Z \geq 82$ ) the results are not as good as those obtained with DD-ME2. The overall quality of the agreement between theoretical and experimental capture rates is slightly better with DD-ME2.

The calculated total muon capture rates for natural elements and individual isotopes are also collected in Table 4.5, and compared with available data [71]. In particular, the calculation nicely reproduces the empirical isotopic dependence of the capture rates [76], i.e. for a given proton number  $Z$  the rates decrease with increasing neutron number, because of the gradual blocking of available neutron levels. The isotopic trend is also illustrated in Fig. 4.5, where the experimental and theoretical total muon capture rates on Ca, Cr and Ni nuclei are plotted. The latter correspond to the quenching  $g_A = 1.262 \rightarrow g_A = 1.135$  for all multipole operators.

## 4.4 Neutrino capture

In the present section the charged-current neutrino-nucleus reactions are considered:

$$\nu_l + {}_Z X_N \rightarrow {}_{Z+1} X_{N-1}^* + l^- , \quad (4.59)$$

where  $l$  denotes the charged lepton (electron, muon). Detailed expressions for the reaction rates and the transition matrix elements can be found in Refs. [64, 61]. The charged-current neutrino-nucleus cross section reads

$$\left( \frac{d\sigma_\nu}{d\Omega} \right) = \frac{1}{(2\pi)^2} V^2 p_l E_l \sum_{\text{lepton spins}} \frac{1}{2J_i + 1} \sum_{M_i M_f} |\langle f | \hat{H}_W | i \rangle|^2 , \quad (4.60)$$

where  $p_l$  and  $E_l$  are the momentum and energy of the outgoing lepton, respectively. In the *extreme relativistic limit*— (ERL), in which the energy of the outgoing lepton is considered much larger than its rest mass, the differential

Table 4.5: Experimental and calculated muon capture rates for natural elements and individual isotopes. The theoretical rates are calculated using the fully consistent RHB plus RQRPA framework with the DD-ME2 universal effective interaction, and with the quenching of the axial-vector coupling constant  $g_A = 1.262 \rightarrow g_A = 1.135$  for all multipole operators. Values for naturally occurring elements (element symbol with no superscript) are weighted averages of capture rates on individual isotopes, using their natural abundances. Experimental values are from Ref. [71], unless otherwise stated. All rates are in units of  $10^6 \text{ s}^{-1}$ .

| Nucleus          | Exp.               | Calc. | Nucleus           | Exp.             | Calc.  | Nucleus           | Exp.               | Calc.  |
|------------------|--------------------|-------|-------------------|------------------|--------|-------------------|--------------------|--------|
| $^{12}\text{C}$  | 0.039              | 0.032 | $^{94}\text{Zr}$  |                  | 8.792  | Nd                | 12.50              | 13.861 |
| $^{16}\text{O}$  | 0.103              | 0.065 | Zr                | 8.660            | 9.619  | $^{148}\text{Sm}$ |                    | 15.425 |
| $^{18}\text{O}$  | 0.088              | 0.057 | $^{92}\text{Mo}$  |                  | 12.374 | $^{150}\text{Sm}$ |                    | 14.132 |
| $^{20}\text{Ne}$ | 0.204              | 0.237 | $^{94}\text{Mo}$  |                  | 12.001 | $^{152}\text{Sm}$ |                    | 13.451 |
| $^{24}\text{Mg}$ | 0.484              | 0.506 | $^{96}\text{Mo}$  |                  | 10.933 | $^{154}\text{Sm}$ |                    | 12.563 |
| $^{28}\text{Si}$ | 0.871              | 0.789 | $^{98}\text{Mo}$  |                  | 9.804  | Sm                | 12.22              | 13.554 |
| $^{32}\text{S}$  | 1.352              | 1.485 | Mo                | 9.614            | 10.995 | $^{156}\text{Gd}$ |                    | 14.785 |
| $^{40}\text{Ar}$ | 1.355              | 1.368 | $^{104}\text{Pd}$ |                  | 13.182 | $^{158}\text{Gd}$ |                    | 13.573 |
| $^{40}\text{Ca}$ | 2.557              | 2.340 | $^{106}\text{Pd}$ |                  | 11.912 | $^{160}\text{Gd}$ |                    | 12.460 |
| $^{44}\text{Ca}$ | 1.793              | 1.851 | $^{108}\text{Pd}$ |                  | 10.795 | Gd                | 11.82              | 13.580 |
| $^{48}\text{Ca}$ | 1.214 <sup>a</sup> | 1.163 | $^{110}\text{Pd}$ |                  | 9.821  | $^{162}\text{Dy}$ |                    | 14.917 |
| $^{48}\text{Ti}$ | 2.590              | 2.544 | Pd                | 10.00            | 11.391 | $^{164}\text{Dy}$ |                    | 13.540 |
| $^{50}\text{Cr}$ | 3.825              | 4.001 | $^{110}\text{Cd}$ |                  | 12.960 | Dy                | 12.29              | 14.194 |
| $^{52}\text{Cr}$ | 3.452              | 3.419 | $^{112}\text{Cd}$ |                  | 11.800 | $^{166}\text{Er}$ |                    | 16.129 |
| $^{54}\text{Cr}$ | 3.057              | 3.065 | $^{114}\text{Cd}$ |                  | 10.746 | $^{168}\text{Er}$ |                    | 14.949 |
| Cr               | 3.472              | 3.483 | $^{116}\text{Cd}$ |                  | 9.829  | $^{170}\text{Er}$ |                    | 13.912 |
| $^{56}\text{Fe}$ | 4.411              | 4.723 | Cd                | 10.61            | 11.381 | Er                | 13.04              | 15.270 |
| $^{58}\text{Ni}$ | 6.110              | 6.556 | $^{116}\text{Sn}$ |                  | 12.395 | $^{178}\text{Hf}$ |                    | 16.434 |
| $^{60}\text{Ni}$ | 5.560              | 5.610 | $^{118}\text{Sn}$ |                  | 11.369 | $^{180}\text{Hf}$ |                    | 15.276 |
| $^{62}\text{Ni}$ | 4.720              | 4.701 | $^{120}\text{Sn}$ |                  | 10.486 | Hf                | 13.03              | 15.783 |
| Ni               | 5.932              | 6.234 | $^{122}\text{Sn}$ |                  | 9.645  | $^{182}\text{W}$  |                    | 17.259 |
| $^{64}\text{Zn}$ |                    | 6.862 | $^{124}\text{Sn}$ |                  | 8.837  | $^{184}\text{W}$  |                    | 15.938 |
| $^{66}\text{Zn}$ |                    | 5.809 | Sn                | 10.44            | 10.923 | $^{186}\text{W}$  |                    | 14.807 |
| $^{68}\text{Zn}$ |                    | 4.935 | $^{126}\text{Te}$ |                  | 10.652 | W                 | 12.36              | 15.971 |
| Zn               | 5.834              | 6.174 | $^{128}\text{Te}$ |                  | 9.830  | $^{198}\text{Hg}$ |                    | 17.369 |
| $^{70}\text{Ge}$ |                    | 6.923 | $^{130}\text{Te}$ |                  | 9.068  | $^{200}\text{Hg}$ |                    | 16.227 |
| $^{72}\text{Ge}$ |                    | 5.970 | Te                | 9.270            | 9.706  | $^{202}\text{Hg}$ |                    | 15.205 |
| $^{74}\text{Ge}$ |                    | 5.519 | $^{132}\text{Xe}$ | 9.4 <sup>b</sup> | 10.631 | $^{204}\text{Hg}$ |                    | 13.993 |
| Ge               | 5.569              | 6.011 | $^{136}\text{Xe}$ | 8.6 <sup>b</sup> | 8.625  | Hg                | 12.74              | 15.733 |
| $^{78}\text{Se}$ |                    | 6.644 | $^{136}\text{Ba}$ |                  | 11.461 | $^{206}\text{Pb}$ |                    | 15.717 |
| $^{80}\text{Se}$ |                    | 5.796 | $^{138}\text{Ba}$ |                  | 10.127 | $^{208}\text{Pb}$ |                    | 13.718 |
| $^{82}\text{Se}$ |                    | 4.935 | Ba                | 9.940            | 10.259 | Pb                | 13.45              | 14.348 |
| Se               | 5.681              | 5.950 | $^{140}\text{Ce}$ |                  | 11.888 | $^{232}\text{Th}$ | 12.56              | 13.092 |
| $^{86}\text{Sr}$ |                    | 8.885 | $^{142}\text{Ce}$ |                  | 12.142 | $^{234}\text{U}$  | 13.79              | 14.231 |
| $^{88}\text{Sr}$ |                    | 7.393 | Ce                | 11.60            | 11.917 | $^{236}\text{U}$  | 13.09 <sup>c</sup> | 13.490 |
| Sr               | 7.020              | 7.553 | $^{142}\text{Nd}$ |                  | 14.043 | $^{238}\text{U}$  | 12.57 <sup>c</sup> | 12.872 |
| $^{90}\text{Zr}$ |                    | 9.874 | $^{144}\text{Nd}$ |                  | 14.288 | $^{242}\text{Pu}$ | 12.90              | 13.554 |
| $^{92}\text{Zr}$ |                    | 9.694 | $^{146}\text{Nd}$ |                  | 12.981 | $^{244}\text{Pu}$ | 12.40 <sup>d</sup> | 12.887 |

<sup>a</sup> From Ref. [72].

<sup>b</sup> From Ref. [73].

<sup>c</sup> From Ref. [74].

<sup>d</sup> From Ref. [75].

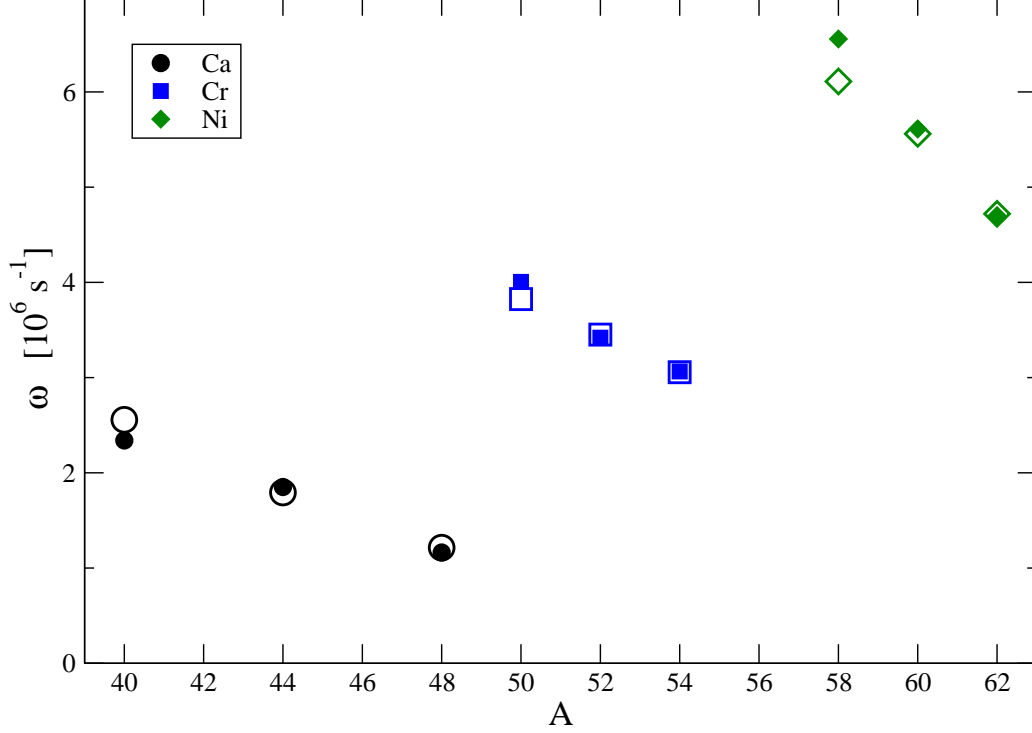


Figure 4.5: Total muon capture rates on Ca, Cr and Ni isotopes. Experimental rates (filled symbols) are compared to theoretical values (empty symbols), calculated using the fully consistent RHB plus RQRPA framework with the DD-ME2 universal effective interaction, and with the quenching of the axial-vector coupling constant  $g_A = 1.262 \rightarrow g_A = 1.135$  for all multipole operators.

neutrino-nucleus cross section takes the form

$$\begin{aligned}
\left(\frac{d\sigma_\nu}{d\Omega}\right)_{ERL} &= \frac{2G^2 \cos^2 \theta_c}{\pi} \frac{E_l^2}{2J_i + 1} \times \left\{ \cos^2 \frac{\vartheta}{2} \sum_{J=0}^{\infty} \left| \langle J_f \parallel \hat{\mathcal{M}}_J - \frac{q_0}{|\mathbf{q}|} \hat{\mathcal{L}}_J \parallel J_i \rangle \right|^2 \right. \\
&+ \left[ \frac{q_\mu^2}{2\mathbf{q}^2} \cos^2 \frac{\vartheta}{2} + \sin^2 \frac{\vartheta}{2} \right] \sum_{J=1}^{\infty} \left[ \left| \langle J_f \parallel \hat{\mathcal{T}}_J^{\text{mag}} \parallel J_i \rangle \right|^2 + \left| \langle J_f \parallel \hat{\mathcal{T}}_J^{\text{el}} \parallel J_i \rangle \right|^2 \right] \\
&\mp \left. \frac{\sin \vartheta/2}{|\mathbf{q}|} \sqrt{q_\mu^2 \cos^2 \frac{\vartheta}{2} + \mathbf{q}^2 \sin^2 \frac{\vartheta}{2}} \sum_{J=1}^{\infty} 2\text{Re} \left[ \langle J_f \parallel \hat{\mathcal{T}}_J^{\text{mag}} \parallel J_i \rangle \langle J_f \parallel \hat{\mathcal{T}}_J^{\text{mag}} \parallel J_i \rangle^* \right] \right\}, \quad (4.61)
\end{aligned}$$

where  $G_F$  is the Fermi constant for the weak interaction,  $\theta_c$  is the Cabibbo's angle,  $\vartheta$  denotes the angle between the incoming and outgoing leptons, the energy of the lepton in the final state is  $E_l$ , and the 4-momentum transfer is  $q \equiv (q_0, \mathbf{q})$ . The nuclear transition matrix elements between the initial state  $|J_i\rangle$  and final state  $|J_f\rangle$ , correspond to the charge  $\hat{\mathcal{M}}_J$ , longitudinal  $\hat{\mathcal{L}}_J$ , transverse electric  $\hat{\mathcal{T}}_J^{\text{el}}$ , and transverse magnetic  $\hat{\mathcal{T}}_J^{\text{mag}}$  multipole operators.

The inclusive cross sections, that sum the contributions from transitions to

all possible final states, are given as functions of neutrino energy, and can be averaged over the experimental neutrino flux when available, e.g. from the decay at rest of  $\mu^+$ , and the decay in flight of  $\pi^+$  [77, 78, 79, 80, 81]. The flux-averaged cross sections provide a crucial test for the validity of the theoretical approach used for modeling neutrino-nucleus reactions.

For charged-current reactions the cross section Eq. (4.60) must be corrected for the distortion of the outgoing lepton wave function by the Coulomb field of the daughter nucleus. In order to be able to compare present results with previous studies [82, 83], the same prescription for the Coulomb correction is used. The cross section can either be multiplied by a Fermi function obtained from the numerical solution of the Dirac equation for an extended nuclear charge distribution [83] or, at higher energies, the effect of the Coulomb field can be described by the effective momentum approximation (EMA) [84], in which the lepton momentum  $p_l$  and energy  $E_l$  are modified as

$$p_l^{eff} = \sqrt{E_l^{eff} - m_l^2} \quad (4.62)$$

$$E_l^{eff} = E_l - V_C(0), \quad (4.63)$$

where  $V_C^{eff}$  is the effective Coulomb potential, the nuclear charge radius is denoted by  $r_c$ , and  $m_l$  is the mass of the outgoing lepton. In a recent study using exact Dirac wave functions, it has been shown that an accurate approximation for the effective electron momenta is obtained by using the mean value of the Coulomb potential;  $V_C^{eff} = 4V_C(0)/5$ , where  $V_C(0) = -3Z\alpha/(2r_c)$  corresponds to the electrostatic potential evaluated at the center of the nucleus [85]. In calculations with EMA the original lepton momentum  $p_l$  and energy  $E_l$  appearing in the expression for the cross section, are replaced by the above effective quantities.

The results of model calculations can be compared with available data by averaging the cross section over the neutrino flux  $f(E_\nu)$ , which depends on the specific neutrino source

$$\langle \sigma_\nu \rangle = \frac{\int dE_\nu \sigma_\nu(E_\nu) f(E_\nu)}{\int dE'_\nu f(E'_\nu)}. \quad (4.64)$$

For  $\nu_e$  the Michel flux from the decay at rest (DAR) of  $\mu^+$  is used [81],

$$f(E_{\nu_e}) = \frac{96E_{\nu_e}^2}{m_\mu^4} (m_\mu - 2E_{\nu_e}), \quad (4.65)$$

whereas for  $\nu_\mu$  the polynomial fit to the experimental flux obtained from the decay in flight (DIF) of  $\pi^+$  [86] is employed.

In Fig. 4.6 the calculated inclusive cross sections are plotted up to 100 MeV neutrino energy for three reactions including also heavier nuclei:  $^{16}\text{O}(\nu_e, e^-)^{16}\text{F}$ ,

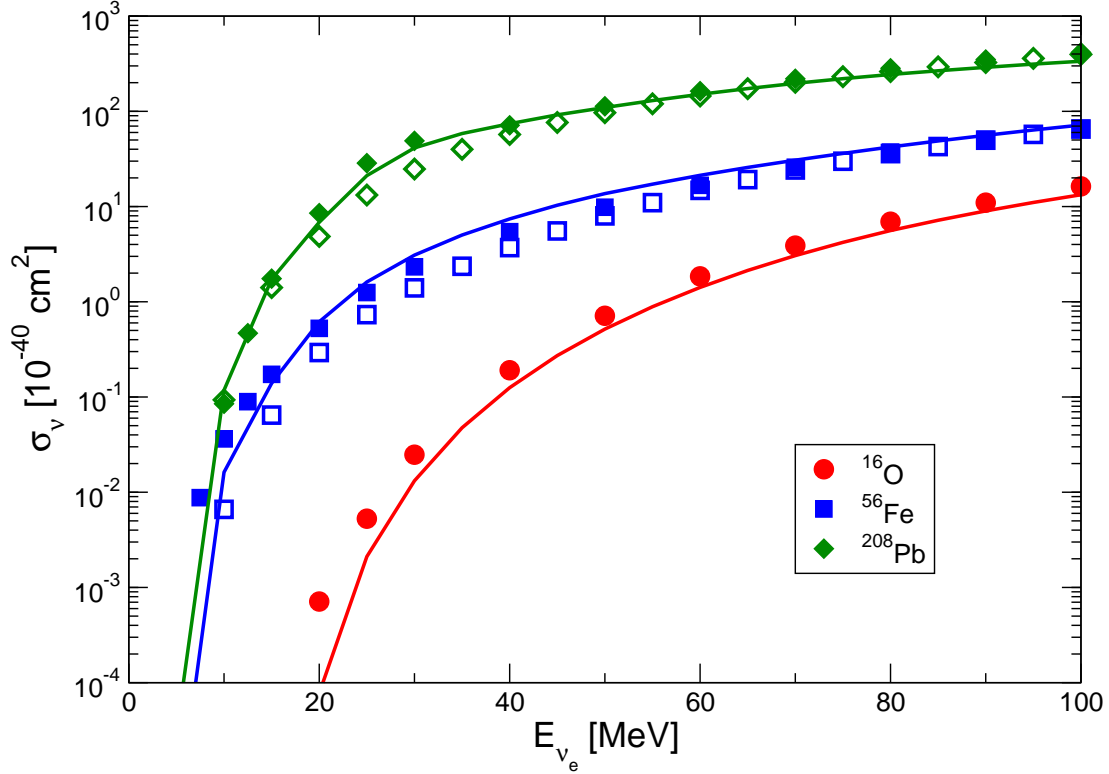


Figure 4.6: Inclusive cross sections for the  $^{16}\text{O}(\nu_e, e^-)^{16}\text{F}$ ,  $^{56}\text{Fe}(\nu_e, e^-)^{56}\text{Co}$ , and  $^{208}\text{Pb}(\nu_e, e^-)^{208}\text{Bi}$  reactions. The RHB plus PN-RQRPA(DD-ME2) results are compared with those obtained in the QRPA with the Skyrme interaction SIII [87] (full symbols) and with a hybrid model [88] (open symbols).

$^{56}\text{Fe}(\nu_e, e^-)^{56}\text{Co}$ , and  $^{208}\text{Pb}(\nu_e, e^-)^{208}\text{Bi}$ . The results of the RHB plus PN-RQRPA calculations are compared with those of a very recent analysis performed with the nonrelativistic QRPA and using the Skyrme interaction SIII [87]. The pronounced enhancement of cross sections for neutrino reactions on heavier nuclei is noticeable: from  $^{16}\text{O}$  to  $^{208}\text{Pb}$  the reaction cross sections increase by more than two orders of magnitude. For the reaction on  $^{208}\text{Pb}$  the present results are in excellent agreement with the QRPA - SIII cross sections [87] at all neutrino energies. This is also the case for the reactions on  $^{16}\text{O}$  and  $^{56}\text{Fe}$  at neutrino energies above 40 MeV, whereas at lower energies the RHB plus RQRPA cross sections appear somewhat below the QRPA results.

In Table 4.6 various theoretical results of flux-averaged cross sections for the electron neutrino reactions with  $^{16}\text{O}$ ,  $^{56}\text{Fe}$ , and  $^{208}\text{Pb}$  target nuclei are compared. For the neutrino flux the DAR spectrum Eq. (4.65) is used, and values obtained with the shell model [89], the tensor model [90], Tamm-Dancoff [91], and various RPA-based calculations are included. For the  $^{16}\text{O}$  target, the present PN-RQRPA(DD-ME2) cross section agrees with the shell

Table 4.6: Flux-averaged cross sections for the  $\nu_e$  reaction on  $^{16}\text{O}$ ,  $^{56}\text{Fe}$ , and  $^{208}\text{Pb}$  target nuclei. Values denoted with  $^a$  were obtained without any quenching of the axial-vector coupling constant ( $g_A = -1.262$ ), while values denoted with  $^b$  were obtained using a quenching factor of  $Q = 0.8$  ( $g_A = -1.0$ ).

|                                       | $^{16}\text{O}(\nu_e, e^-)^{16}\text{F}$<br>$\langle\sigma\rangle(10^{-42}\text{cm}^2)$ | $^{56}\text{Fe}(\nu_e, e^-)^{56}\text{Co}$<br>$\langle\sigma\rangle(10^{-42}\text{cm}^2)$ | $^{208}\text{Pb}(\nu_e, e^-)^{208}\text{Bi}$<br>$\langle\sigma\rangle(10^{-42}\text{cm}^2)$ |
|---------------------------------------|---|---|---|
| SM( $0\hbar\omega \times 0.64$ ) [89] | 10.8  |   |   |
| TM [90]                               |   | 214   |   |
| TDA(SKIII) [91]                       |   |   | 2954,3204   |
| SM + SGII [92]                        |   | 269   |   |
| RPA [93]                              | 14.55   | 277   | 2643  |
| CRPA(WS+LM) [88]                      |   | 240   | 3620  |
| (Q)RPA(SIII,SGII)                     | 16.90,17.20 [94]  | 352 [87]  | 4439 [95]   |
| PN-RQRPA(DD-ME2) <sup>a</sup>         | 8.825   | 473   | 4848  |
| PN-RQRPA(DD-ME2) <sup>b</sup>         | 6.090   | 341   | 3284  |
| Exp.(KARMEN) [79, 88]                 |   | $256 \pm 108 \pm 43$  |   |

model and (Q)RPA results. For heavier targets the differences between various calculations are more pronounced. Particularly important is the reaction  $^{56}\text{Fe}(\nu_e, e^-)^{56}\text{Co}$ , because it is the only case in which data are available for a medium-heavy target nucleus [79, 88]. The two self-consistent calculations: the QRPA [87] and the present RHB plus PN-RQRPA, which do not require any additional adjustments of the model parameters to the specific target nucleus, predict values for the cross section:  $352 \times 10^{-42}\text{cm}^2$  (QRPA [87]) and  $341 \times 10^{-42}\text{cm}^2$  (PN-RQRPA) which are within the uncertainties of the experimental result  $(256 \pm 108 \pm 43) \times 10^{-42}\text{cm}^2$ .

Obviously various theoretical approaches differ significantly in the predicted neutrino-nucleus cross sections, and this will require more detailed studies of the underlying nuclear structure that contributes to the neutrino reaction rates. On the other hand, the only data for a medium-heavy target nucleus are from the KARMEN collaboration [79], and this result has not yet been confirmed by independent measurement. One hopes that future experiments will provide additional constraints for theoretical models that are used in the description of weak interaction rates. At the same time the nuclear structure input for neutrino-nucleus cross sections must be further analyzed, and checked by improving the description of nuclear ground-state properties and spin-isospin excitations relevant for the calculation of the reaction rates.

The contribution of different multipole transitions to the cross section for the reaction  $^{56}\text{Fe}(\nu_e, e^-)^{56}\text{Co}$ , at increasing neutrino energies, is illustrated in Fig. 4.7. The partial contributions to the total cross section of multipoles

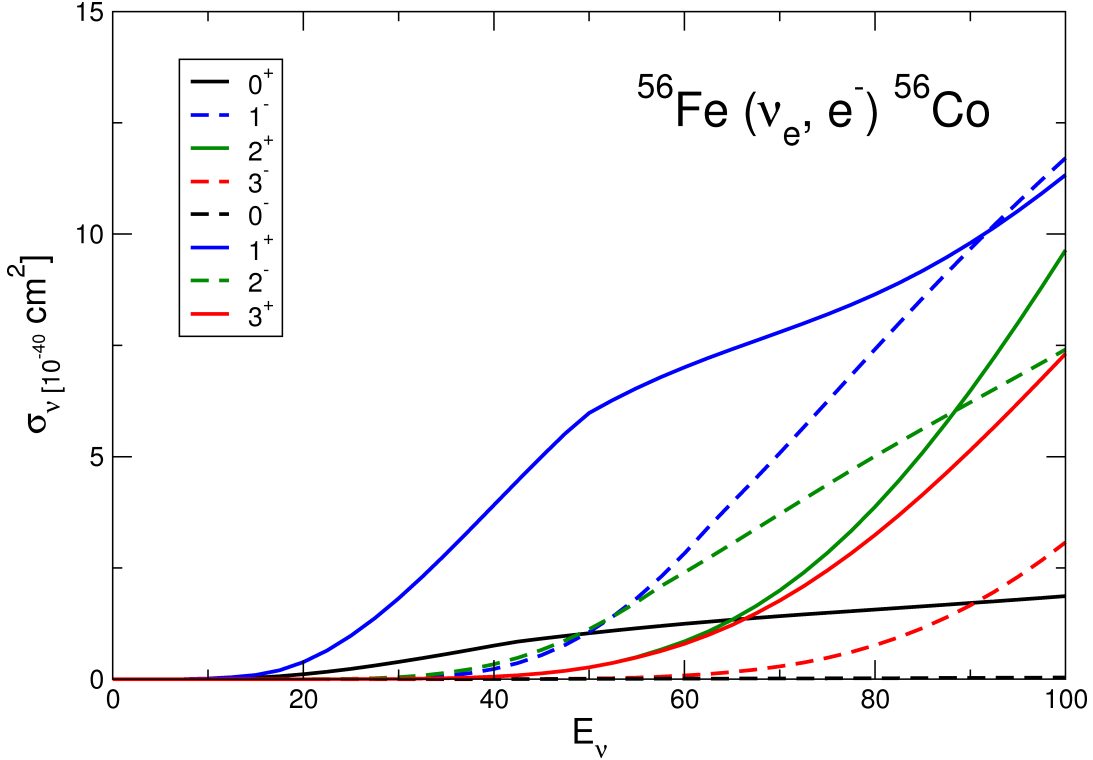


Figure 4.7: Inclusive cross sections for the  $^{56}\text{Fe}(\nu_e, e^-)^{56}\text{Co}$  reaction. Positive parity multipoles are denoted by full lines, while negative parity transitions are denoted by dashed lines.

from  $J = 0^\pm$  to  $J = 3^\pm$  are displayed. At  $E_{\nu_e} = 20$  MeV the reaction is dominated by transitions to the IAS and GTR. At higher energies, however, other multipolarities start to play an important role and one notices, in particular, the dominant contribution of the  $1^-$  transitions at  $E_{\nu_e} = 60$  and 80 MeV. This distribution of multipole transitions, calculated in the RHB plus PN-RQRPA model, is similar to the one obtained in the QRPA with Skyrme effective interactions [87]. The differences in the contributions of higher multipoles can be attributed to the different effective interactions employed in the two models.

Using the decay-at-rest (DAR) neutrino spectrum, cross sections have been averaged for each multipole with results compared to hybrid model calculation [96] in Table 4.7. Maximum neutrino energy in the DAR spectrum is 52.8 MeV, making these averaged cross sections sensitive only to relatively low energies. The expected result is that dominating contribution comes from Gamow-Teller channel, with a noticeable contribution of allowed  $0^+$  and forbidden  $1^-$  and  $2^-$  excitations. Both theoretical studies reproduce this structure. Main difference occurs in the Gamow-Teller channel where the relativistic model predicts a cross section which is twice as large as the hybrid model prediction.  $1^-$  and  $2^-$  transitions calculated using the DD-ME2 interaction are



Table 4.7: Flux-averaged cross sections of each multipole transition for the  $^{56}\text{Fe}(\nu_e, e^-)^{56}\text{Co}$  reaction compared to a hybrid shell model + CRPA calculation. Averaged cross sections were obtained using a quenching factor of  $Q = 0.8$  ( $g_A = -1.0$ ). All cross sections given in units of  $10^{-42} \text{ cm}^2$ .

| $J^\pi$ | Hybrid model [96] | DD-ME2 |
|---------|-------------------|--------|
| $0^+$   | 52.7              | 48.0   |
| $0^-$   | 0.4               | 0.2    |
| $1^+$   | 112.1             | 244.9  |
| $1^-$   | 29.4              | 16.6   |
| $2^+$   | 4.1               | 4.2    |
| $2^-$   | 35.0              | 21.8   |
| $3^+$   | 4.2               | 4.2    |
| $3^-$   | 0.2               | 0.1    |

approximately 40% smaller than those obtained with the hybrid model. This occurs due to quenching of the axial-vector coupling constant for all multipoles equally in the relativistic model, as opposed to quenching applied only in the Gamow-Teller channel in the hybrid model.

An important application of microscopic models of neutrino-nucleus reactions is the calculation of cross sections for supernova neutrinos. Accurate modeling of reaction rates on nuclei that can be used as targets for the supernova neutrino detectors is, of course, essential for studies of supernova dynamics and, in particular, of weak interaction processes which determine the evolution of a supernova explosion. The supernova neutrino flux is usually described by the Fermi-Dirac spectrum:

$$f(E_\nu) = \frac{1}{T^3} \frac{E_\nu^2}{\exp[(E_\nu/T) - \alpha] + 1}. \quad (4.66)$$

At typical supernova neutrino energies one expects the total cross section for the charged current reaction ( $\nu_e, e^-$ ) to be dominated by the allowed transitions to the IAS and the Gamow-Teller resonance states in the daughter nucleus. In Fig. 4.9 the flux-averaged cross sections for the reaction  $^{56}\text{Fe}(\nu_e, e^-)^{56}\text{Co}$  are displayed, evaluated at different temperatures in the interval  $T = 2 - 10 \text{ MeV}$ , and for the chemical potential  $\alpha=0$ . The results are in good agreement with those obtained in the shell-model calculation of Ref. [92, 97], particularly at higher temperatures. This is a very interesting result, because the two models are based on entirely different concepts, and use different effective interactions. An important advantage of the present approach, however, is that it can easily be extended to heavier nuclei and to systems far from stability, and therefore also applied in the description of the  $r$ -process nucleosynthesis.

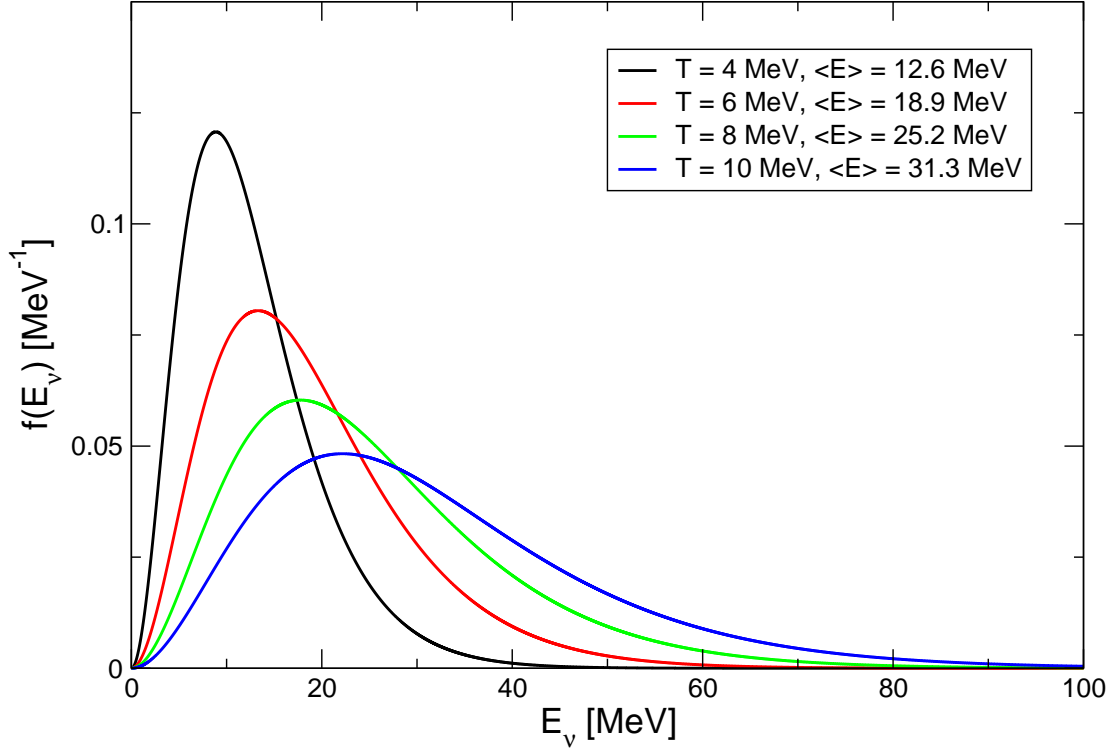


Figure 4.8: Supernova neutrino fluxes for temperatures ranging from  $T = 4$  MeV to  $T = 10$  MeV,  $\alpha = 0$ .

The model has also been tested in the case of the heavy target:  $^{208}\text{Pb}(\nu_e, e^-)^{208}\text{Bi}$ . For the same neutrino flux as in the previous example, the corresponding cross sections are shown in Fig. 4.10 and compared, at  $T = 6, 8$  and  $10$  MeV, with the results from Refs. [88, 95, 99]. Since at higher temperatures the neutrino flux extends toward higher neutrino energies, the calculated cross sections display a pronounced enhancement with temperature. In comparison with the RPA-based results from Refs. [95, 88], good agreement is obtained at all temperatures. Note that the calculation of Ref. [99], which includes the IAS, the GT, and the first-forbidden transitions computed in the Goldhaber-Teller model, consistently predicts higher values for the flux-averaged cross section at all considered temperatures. As it has already been discussed in Ref. [95], a possible origin of this difference could be the use of the Fermi function for the Coulomb correction at higher neutrino energies, instead of the EMA.

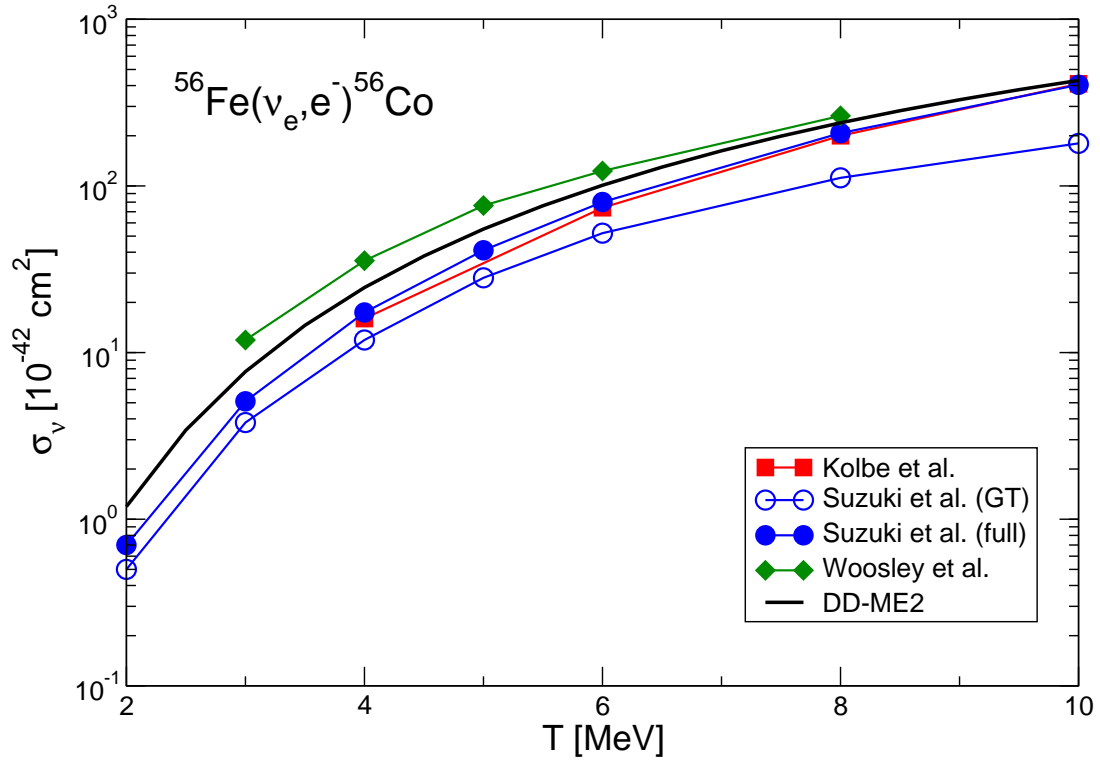


Figure 4.9: Inclusive cross section for the  $^{56}\text{Fe}(\nu_e, e^-)^{56}\text{Co}$  reaction, averaged over the supernova neutrino flux and plotted as a function of temperature. The pn-RQRPA results obtained with the DD-ME2 effective interaction are compared with the shell model cross sections from Refs. [88, 92, 98].

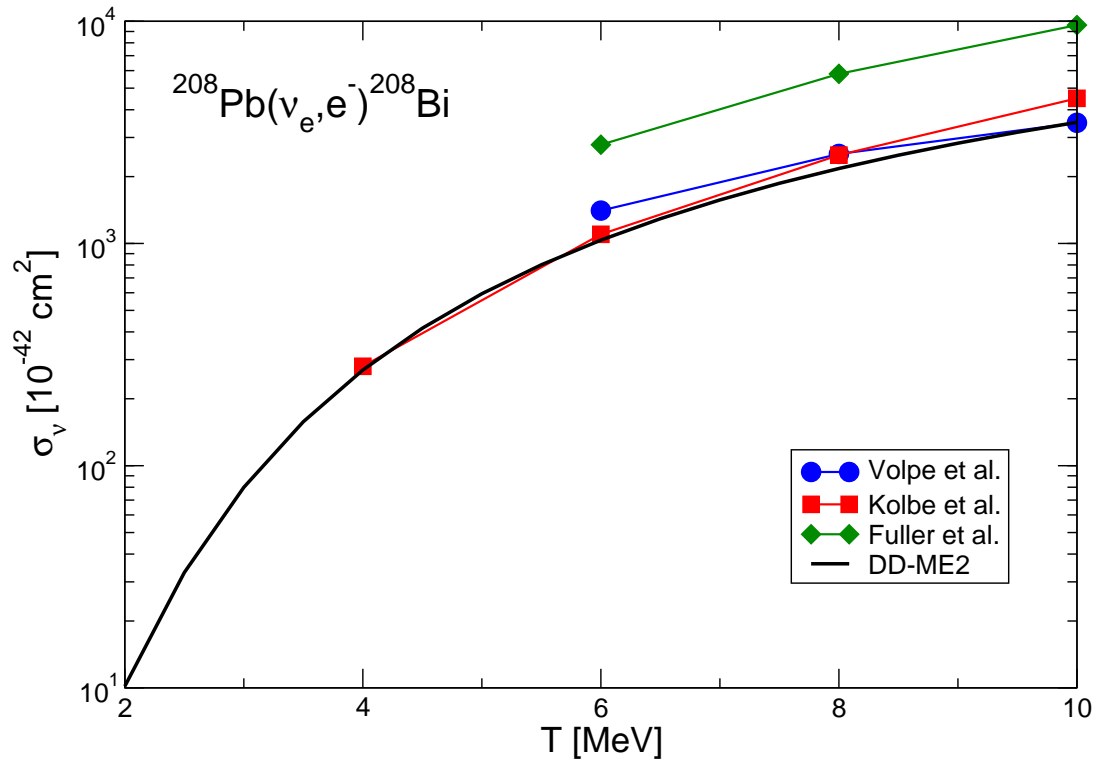


Figure 4.10: Inclusive cross section for the  $^{56}\text{Fe}(\nu_e, e^-)^{56}\text{Co}$  reaction, averaged over the supernova neutrino flux and plotted as a function of temperature. The pn-RQRPA results obtained with the DD-ME2 effective interaction are compared with the shell model cross sections from Refs. [88, 95, 99].



# Chapter 5

## Conclusion

In the present thesis the relativistic Hartree-Bogoliubov (RHB) + proton-neutron relativistic quasiparticle random phase approximation (pn-RQRPA) have been employed in an effort to study semi-leptonic weak-interaction processes in spherical, even-even, neutron-rich nuclei. In the particle-hole channel an effective Lagrangian with meson-nucleon coupling constants dependent on nucleon vector density was used, while the pairing correlations were described with the pairing part of the D1S Gogny interaction. Due to a standard problem of low effective nucleon mass in relativistic models two extensions of the density-dependent RHB were made by (i) inclusion of an  $\omega$ -meson tensor coupling term in the Lagrangian density and (ii) inclusion of momentum dependence of nucleon vector and scalar self-energies. Interaction used at the RPA level is identical to the one used at the mean-field level making the framework fully self-consistent. This is an important characteristic of the model, as it removes spurious components of strength distributions. Only spherical, even-even nuclei were treated, where the pion field contribution was nonexistent at the mean-field level due to the negative parity of the pion. It needs to be included at the RPA level, however, as well as the Landau-Migdal contact term to resolve issues with divergent contributions. Strength of the Landau-Migdal term is the only additional parameter introduced, adjusted to reproduce the position of the Gamow-Teller resonance in  $^{208}\text{Pb}$ .

Microscopic global predictions of weak interaction rates are important, as most of the neutron-rich nuclei relevant for the  $r$ -process nucleosynthesis are not experimentally accessible. Calculated  $\beta$ -decay half-lives depend on a detailed description of transition energies, shell structure, and on the choice of the residual interactions in the  $ph$  and  $pp$  channels. In the present analysis it has been shown that standard relativistic mean-field effective interactions, adjusted to nuclear matter and ground-state properties of spherical nuclei, generally overestimate the empirical half-lives by more than an order of magnitude. The main reason is their low effective nucleon mass which is, in the standard choice of interaction terms, strongly related to the empirical energy

spacings of spin-orbit partner states. Thus, in order to be able to reproduce measured  $\beta$ -decay half-lives, the effective nucleon mass of the relativistic mean-interaction used in the RHB calculation of nuclear ground state and in the  $ph$  channel of the QRPA residual interaction has to be increased. In this thesis this has been done on the mean-field level, by including an additional isoscalar tensor-coupling term in the Lagrangian, which allows for an increase of the Dirac mass and effective mass, while at the same time the new effective interaction reproduces the ground-state properties of finite nuclei, including the spin-orbit splitting. The new force has been adjusted starting from our most successful parameter set so far, the density-dependent interaction DD-ME1. However, the inclusion of the tensor term allows only for a moderate increase of the effective mass. It is not possible, like in Skyrme forces for example, to obtain interactions with values of the effective mass close to one.

With the new density-dependent interaction DD-ME1\* the GT distribution strengths and  $\beta$ -decay rates of neutron-rich nuclei in the mass regions  $Z \approx 28$  and  $Z \approx 50$  have been calculated. The model reproduces in detail the data on GT resonances and the low-energy GT strength. The results for  $\beta$ -decay half-lives are similar to those obtained in the nonrelativistic PN-QRPA calculation of Ref. [53], where it was shown that a fine tuning of the strength of the  $T = 0$  pairing interaction is necessary in order to reproduce the experimental data. In general, by adjusting the strength parameter of the proton-neutron pairing interaction to one experimental half-life, the PN-RQRPA calculation reproduces the data for a chain of isotopes. In the region  $Z \approx 28$  very different values of the  $T = 0$  pairing strength reproduce the empirical lifetimes of the Fe and Zn isotopic chains, whereas a single value, adjusted to the half-life of  $^{130}\text{Cd}$ , qualitatively reproduces the data in the  $Z \approx 50$  region.  $T = 0$  pairing, however, does not help in the case of Ni isotopes and for  $^{132}\text{Sn}$ , and the model overestimates the half-lives on Ni nuclei and predicts a  $\beta$ -stable  $^{132}\text{Sn}$ . Therefore, it was not possible, as suggested in Ref. [53], to adjust the strength of the  $T = 0$  pairing on experimental data, and extend the calculation to other mass regions, or even to other isotopic chains in the same mass region. This problem could be, however, due to the deficient description of shell structure, related to the low effective mass of the  $ph$  interaction used. This is also the reason a calculation of  $\beta$ -decay rates in the region  $N \approx 126$  was not attempted, as there are not enough data to constrain the strength of the  $T = 0$  pairing interaction.

The calculations performed in this thesis have shown that the extension of the standard relativistic mean-field framework to include momentum-dependent (energy-dependent in stationary systems) nucleon self-energies naturally leads to an enhancement of the effective (Landau) nucleon mass, and thus to an improved PN-QRPA description of  $\beta^-$ -decay rates. However, even though the momentum-dependent RMF model with density-dependent meson-nucleon couplings, adjusted here to  $m^* = 0.79m$ , predicts half-lives of neutron-rich

medium-mass nuclei in qualitative agreement with data, the results are not as good as those obtained in the most advanced non-relativistic self-consistent density-functional plus continuum-QRPA calculations [100], or with the self-consistent HFB+QRPA model with Skyrme interactions of Ref. [53]. Namely, although it has been possible to increase the effective mass of the interaction used in the RHB calculations of nuclear ground states to  $m^* = 0.79 m$ , a value which is sufficient for the description of giant resonances, the detailed description of the low-energy Gamow-Teller strength necessitates an even higher value of  $m^*$ . In fact, the effective mass of the Skyrme SkO' interaction used in Ref. [53] is  $m^* = 0.9 m$ , whereas the continuum-QRPA calculations by Borzov are based on the Fayans phenomenological density functional with the bare nucleon mass, i.e.  $m^* = m$ . However, it would be very difficult to further increase the effective nucleon mass in the framework of the model used in this work, i.e. on the nuclear matter level, without destroying the good agreement with empirical ground-state properties of finite nuclei. On the other hand, this would not even be the correct procedure because the additional enhancement of the effective nucleon mass is due to the coupling of single-nucleon levels to low-energy collective vibrational states, an effect which goes entirely beyond the mean-field approximation and is not included in the present model. In principle, the effect of two- and three-phonon states on the weak-interaction rates could be taken into account by explicitly considering the coupling of single-quasiparticle states to phonons, and the resulting complex configurations would certainly lead to a redistribution of low-energy Gamow-Teller strength.

The RHB plus proton-neutron RQRPA model has been tested in the calculation of total muon capture rates on a large set of nuclei from  $^{12}\text{C}$  to  $^{244}\text{Pu}$ . The calculation is fully consistent, the same universal effective interactions are used both in the RHB equations that determine the quasiparticle basis, and in the matrix equations of the RQRPA. The calculated capture rates are sensitive to the in-medium quenching of the axial-vector coupling constant. By reducing this constant from its free-nucleon value  $g_A = 1.262$  to the effective value  $g_A = 1.135$  for all multipole transitions, i.e. with a quenching of approximately 10%, the experimental muon capture rates are reproduced with an accuracy better than 10%. This result can be compared to recent RPA-based calculations that reproduce the experimental values to better than 15%, using phenomenological potentials adjusted to individual nuclei and  $A$ -dependent residual interactions, but without applying any quenching to the operators responsible for the  $\mu^-$  capture process. The test has demonstrated that the RHB plus QRPA model provides a consistent and accurate description of semi-leptonic weak interaction processes at finite momentum transfer in medium-heavy and heavy nuclei over a large  $Z$ -range.

A number of illustrative test calculations have been performed for charged-current neutrino reactions on  $^{12}\text{C}$ ,  $^{16}\text{O}$ ,  $^{56}\text{Fe}$ , and  $^{208}\text{Pb}$ , in the low-energy range below 100 MeV neutrino energy. The results have been compared with



those obtained in previous theoretical studies based on the shell model and the non-relativistic random phase approximation, and with the available experimental values for flux-averaged cross sections. In addition to the total neutrino-nucleus cross sections, the evolution of the contributions of different multipole excitations has also been analyzed as a function of neutrino energy. It has been shown that except at relatively low neutrino energies  $E \leq 30$  MeV, for which the reactions are dominated by transitions to IAS and GTR states, at higher energies the inclusion of spin-dipole transitions, and also excitations of higher multipolarities, is essential for a quantitative description of neutrino-nucleus cross sections. Finally, the cross sections for reactions of supernova neutrinos on  $^{16}\text{O}$  and  $^{208}\text{Pb}$  target nuclei have been investigated as functions of the temperature and chemical potential.

The results for the test cases are in good agreement with the available data, and with the cross sections calculated in the shell model for reactions on light nuclei. The advantage of the RHB plus PN-RQRPA model over the shell model approach is, of course, the possibility of performing calculations for reactions on heavier nuclei and in regions of nuclei far from stability. The differences between the results of various RPA-based calculations, especially in heavier nuclei and at low neutrino energies, can most probably be attributed to the different effective interactions used in modeling the structure of target nuclei, but they also indicate that more detailed experimental and theoretical studies of the transitions that contribute to the neutrino reaction rates must be performed.

The relativistic Hartree-Bogoliubov and the proton-neutron relativistic quasi-particle RPA represent a powerful method of examination of all semi-leptonic weak-interaction processes. Enhancement of the effective nucleon mass has proven to be crucial for a good quantitative description of  $\beta$ -decay half-lives as they are very sensitive to low energy tail of the transition strength. Combined with a more general formulation of the weak interaction framework, relativistic models are an important quantitative tool able to provide precise predictions of all semi-leptonic weak-interaction processes in neutron-rich nuclei.

# Appendix A

## Relativistic model with momentum-dependent self-energies

The Lagrangian density is of the form

$$\mathcal{L} = \frac{1}{2} [\bar{\psi}\Gamma_\mu iD^\mu\psi + (i\bar{D}^\mu\psi)\Gamma_\mu\psi] - \bar{\psi}\Gamma M^*\psi + \mathcal{L}_m, \quad (\text{A.1})$$

with the nucleon field  $\psi$ , and the covariant derivative  $iD_\mu$  defined as

$$iD_\mu = i\partial_\mu - \gamma_\omega\omega_\mu - \gamma_\rho\vec{\tau} \cdot \vec{\rho}_\mu - e\frac{1+\tau_3}{2}A_\mu, \quad (\text{A.2})$$

and the mass operator  $M^*$

$$M^* = m - \gamma_\sigma\sigma. \quad (\text{A.3})$$

Meson degrees of freedom are included in the same way as in (2.3). The difference, when compared to the standard relativistic models, lies in quantities  $\Gamma_\mu$  and  $\Gamma$  which are usually equal to the Dirac matrices  $\gamma_\mu$  and unit matrix, respectively. In this approach they are given by

$$\Gamma_\mu = \gamma^\nu g_{\mu\nu} + \gamma^\nu Y_{\mu\nu} - \gamma_{\mu\nu} Z^\nu, \quad (\text{A.4})$$

and

$$\Gamma = 1 + \gamma_\mu u_\nu Y^{\mu\nu} - u_\mu Z^\nu. \quad (\text{A.5})$$

Here the  $g^{\mu\nu}$  denotes the metric tensor, and  $u_\mu = j_\mu/\rho_v$  the four-velocity depending on the vector current density  $j_\mu = \bar{\psi}\gamma_\mu\psi$  and the vector density  $\rho_v = \sqrt{j_\mu j^\mu}$ . The quantities  $Y^{\mu\nu}$  and  $Z^\mu$  are defined as

$$Y^{\mu\nu} = \frac{\Gamma_V}{m^4} m_\omega^2 \omega^\mu \omega^\nu \quad (\text{A.6})$$

and

$$Z^\mu = \frac{\Gamma_S}{m^2} \omega^\mu \sigma. \quad (\text{A.7})$$

The particular dependence on the meson fields is required to generate a linear energy dependence of the scalar and vector self-energies.  $\Gamma_S$  and  $\Gamma_V$  are new constants of the interaction requiring readjustment of all interaction parameters.

Variation of the Lagrangian density (A.1) provides the Dirac equation for the nucleons of the form

$$\gamma^\mu (i\partial_\mu - \Sigma_\mu) \psi - (m - \Sigma)\psi = 0. \quad (\text{A.8})$$

Quantities  $\Sigma_\mu$  and  $\Sigma$  denote the vector and scalar self-energies, respectively. They are functions of meson fields and nuclear densities and are given by

$$\Sigma_\mu = v_\mu - Y_{\mu\nu} (iD^\nu - M^* u^\nu) + \Sigma_\mu^R, \quad (\text{A.9})$$

$$\Sigma = s - Z^\mu (iD_\mu - M^* u_\mu), \quad (\text{A.10})$$

where vector and scalar potentials read

$$v_\mu = \Gamma_\omega \omega_\mu + \Gamma_\rho \vec{\tau} \cdot \vec{\rho}_\mu + \Gamma_\gamma \frac{1 + \tau_3}{2} A_\mu - \frac{i}{2} \partial^\lambda Y_{\mu\lambda}, \quad (\text{A.11})$$

$$s = \Gamma_\sigma \sigma - \frac{i}{2} \partial^\mu Z_\mu. \quad (\text{A.12})$$

In all expressions we neglect the contribution of the  $\delta$ -meson. In this model self-energies are differential operators acting on the nucleon fields. Momentum dependence enters through terms  $(iD^\nu - M^* u^\nu)$ , where the time-like component is equivalent to  $E - m$  when acting on a plane wave. The rearrangement term in the vector self-energy is equal to

$$\Sigma_\mu^R = u_\lambda \left[ \Gamma'_\omega \omega_\mu J^\mu + \Gamma'_\rho \vec{\rho}_\mu \cdot \vec{J}^\mu - \Gamma'_\sigma \sigma P_s \right] \quad (\text{A.13})$$

$$- (t_{\nu\mu}^D - u_\nu j_\mu^{M*}) \frac{\Gamma'_V}{\Gamma_V} Y^{\mu\nu} + (j_\mu^D - u_\mu \rho_s^{M*}) \frac{\Gamma'_S}{\Gamma_S} Z^\mu \quad (\text{A.14})$$

$$+ (j_\mu^{M*} Y^{\mu\nu} - \rho_s^{M*} Z^\nu) \frac{g_{\nu\lambda} - u_\lambda u_\nu}{\rho_v}, \quad (\text{A.15})$$

where  $\Gamma'_i$  are the derivatives  $d\Gamma/d\rho_v$  of meson fields over nucleon vector density. Densities and currents

$$J_\mu = \bar{\psi} \Gamma_\mu \psi, \quad \vec{J}_\mu = \bar{\psi} \Gamma_\mu \vec{\tau} \psi, \quad (\text{A.16})$$

$$P_s = \bar{\psi} \Gamma \psi, \quad \vec{P}_s = \bar{\psi} \Gamma \vec{\tau} \psi, \quad (\text{A.17})$$

replace the usual (iso)vector and (iso)scalar densities. With momentum dependence, additional terms appear

$$t_{\mu\nu}^D = \frac{1}{2} [\bar{\psi}\gamma_\mu iD_\nu\psi + (i\bar{D}_\nu\psi\gamma_\mu\psi)], \quad (\text{A.18})$$

$$j_\mu^D = \frac{1}{2} [\bar{\psi}iD_\mu\psi + (i\bar{D}_\mu\psi\psi)], \quad (\text{A.19})$$

$$j_\mu^{M^*} = \bar{\psi}\gamma_\mu M^*\psi, \quad \rho_s^{M^*} = \bar{\psi}M^*\psi. \quad (\text{A.20})$$

Continuity equations can be derived from the Dirac equation for extended currents and densities in (A.16) and (A.17).

Equations of motion for the meson fields read

$$\partial_\mu\partial^\mu\sigma + m_\sigma^2\sigma + \tilde{C}_\mu\omega^\mu = \Gamma_\sigma P_s, \quad (\text{A.21})$$

$$\partial^\nu G_{\nu\mu} + m_\omega^2\omega^\nu C_{\mu\nu} - \tilde{C}_\mu\sigma = \Gamma_\omega J_\mu, \quad (\text{A.22})$$

$$\partial^\nu \vec{H}_{\nu\mu} + m_\rho^2\vec{\rho}_\mu = \Gamma_\rho \vec{J}_\mu, \quad (\text{A.23})$$

where the terms coupling  $\sigma$ - and  $\omega$ -mesons are given by

$$C_{\mu\nu} = g_{\mu\nu} + \frac{\Gamma_V}{m^4} (t_{\mu\nu}^D + t_{\nu\mu}^D - u_\nu j_\mu^{M^*} - u_\mu j_\nu^{M^*}) \quad (\text{A.24})$$

and

$$\tilde{C} = \frac{\Gamma_S}{m^2} (j_\mu^D - u_\mu \rho_s^{M^*}). \quad (\text{A.25})$$

For a stationary system the conserved baryon density, i.e. the time-like component of the current  $J_\mu$  becomes

$$\rho = J_0 = j_0(1 + Y_{00}) - \rho_s Z_0, \quad (\text{A.26})$$

and the generalized scalar density is given by

$$P_s = \rho_s(1 - Z_0) + j_0 Y_{00}, \quad (\text{A.27})$$

where  $Y_{00}$  and  $Z_0$  are

$$Y_{00} = \frac{\Gamma_V}{m^4} m_\omega^2 \omega_0^2, \quad Z_0 = \frac{\Gamma_S}{m^2} \omega_0 \sigma. \quad (\text{A.28})$$

The vector and scalar self-energies become

$$\Sigma_0 = v_0 + Y_{00}(v_0 + m - s) + \Sigma_0^R - Y_{00}i\partial^0, \quad (\text{A.29})$$

and

$$\Sigma = s + Z_0(v_0 + m - s) - Z_0i\partial^0 \quad (\text{A.30})$$

respectively. The  $v_0$  and  $s$  terms are

$$v_0 = g_\omega\omega_0 + g_\rho\vec{\tau} \cdot \vec{\rho}_0 + e\frac{1 + \tau_3}{2}A_0 \quad (\text{A.31})$$

and

$$s = g_\sigma \sigma, \tag{A.32}$$

with the rearrangement contribution being

$$\Sigma_0^R = \left[ g'_\omega \omega_0 J^0 + g'_\rho \vec{\rho}_0 \cdot \vec{J}^0 - g'_\sigma \sigma P_s - (t_{00}^D - j_0^{M*}) \frac{\Gamma'_V}{\Gamma_V} Y_{00} + (j_0^D - \rho_s^{M*}) \frac{\Gamma'_S}{\Gamma_S} Z_0 \right]. \tag{A.33}$$

# Appendix B

## Finite element method

In order to obtain a precise form of the muon wave-function we solve the Dirac equation for the muon in the 1s bound state. We cannot, however, use the basis of spherical harmonic oscillator eigenstates that we use for the nuclear part of the problem. Because the Bohr radius of the muon is up to two order of magnitude larger than the nuclear radius, a very large configuration space would be necessary to correctly describe the wave function. Therefore, we approximate the solution with piecewise polynomials using B splines. This method has already been successfully applied to Coulomb interaction [101], relativistic  $\sigma - \omega$  model [65] and the relativistic Hartree-Bogoliubov problem [28, 29].

As a basis for our radial wave functions we use the  $B_{i,k}$ ,  $i = 1, 2, \dots, n$  splines, a set of  $n$  polynomials of order  $k$  defined over a finite region of the domain. Dividing the domain into  $N$  elements, we define  $N + 2k - 1$  knots  $t_i$  as [101]

$$t_i = \begin{cases} 0 & i = 1, 2, \dots, k - 1 \\ R_{max} \frac{i-k}{N} & k < i < N + k - 1 \\ R_{max} & N + k < i < N + 2k - 1 \end{cases} . \quad (\text{B.1})$$

Using this knot sequence, we can now define the B spline polynomials of order 1 with

$$B_{i,1}(x) = \begin{cases} 1 & t_i \leq x \leq t_{i+1} \\ 0 & \text{otherwise} \end{cases} , \quad (\text{B.2})$$

and polynomials of higher order recursively by

$$B_{i,k}(x) = \frac{x - t_i}{t_{i+k-1} - t_i} B_{i,k-1}(x) + \frac{t_{i+k} - x}{t_{i+k} - t_{i+1}} B_{i+1,k-1}(x). \quad (\text{B.3})$$

The set of B-splines of order  $k$  on a knot sequence  $\{t_i\}$  forms a complete basis for piecewise polynomials of degree  $k - 1$  on the intervals defined by the knot sequence. We represent the solution to the Dirac equation as a linear combinations of these B splines and we work with the representations rather

than with the functions themselves. Using the solution to the Dirac equation of the form

$$\psi(\mathbf{r}, s, t) = \frac{1}{r} \begin{pmatrix} f(r)\Phi_{j,l,m}(\theta, \varphi, s) \\ ig(r)\Phi_{j,\tilde{l},m}(\theta, \varphi, s) \end{pmatrix} \chi_t(t). \quad (\text{B.4})$$

we expand the radial functions in terms of B splines as

$$f(r) = \sum_{i=1}^n f_i B_{i,k}(r), \quad g(r) = \sum_{i=1}^n g_i B_{i,k}(r). \quad (\text{B.5})$$

Dirac equation can now be written down in terms of scalar products of B splines as

$$\begin{pmatrix} S_4 + S_5 - \lambda S_3 & S_1 - \kappa S_2 \\ -S_1 - \kappa S_2 & -S_4 + S_5 - \lambda S_3 \end{pmatrix} \begin{pmatrix} f_i \\ g_i \end{pmatrix} = E \begin{pmatrix} S_3 & 0 \\ 0 & S_3 \end{pmatrix} \begin{pmatrix} f_i \\ g_i \end{pmatrix}, \quad (\text{B.6})$$

with the matrix elements defined as

$$S_1 = \langle B_{i',k}(r) | \partial_r | B_{i,k}(r) \rangle, \quad (\text{B.7})$$

$$S_2 = \langle B_{i',k}(r) | 1/r | B_{i,k}(r) \rangle, \quad (\text{B.8})$$

$$S_3 = \langle B_{i',k}(r) | B_{i,k}(r) \rangle, \quad (\text{B.9})$$

$$S_4 = \langle B_{i',k}(r) | m^* | B_{i,k}(r) \rangle, \quad (\text{B.10})$$

$$S_5 = \langle B_{i',k}(r) | V(r) | B_{i,k}(r) \rangle, \quad (\text{B.11})$$

and  $\kappa = \pm (j + \frac{1}{2})$  with  $j = l \mp \frac{1}{2}$ . In this way the problem of solving the Dirac equation is reduced to a simple eigenvalue problem solved by diagonalization.

While solving the specific problem of a muon bound in a 1s state of an atom, we have used  $n = 300$  B splines of order  $k = 9$ , with the radial mesh extending to 300 fm. These values were sufficient to obtain the desired accuracy of the muon wave functions.

# Bibliography

- [1] D. Vretenar, A. Afanasjev, G. Lalazissis, and P. Ring, *Physics Reports* **409**, 101 (2005).
- [2] N. Paar, D. Vretenar, E. Khan, and G. Colo, *Reports on Progress in Physics* **70**, 691 (2007).
- [3] K. Langanke and G. Martinez-Pinedo, *Reviews of Modern Physics* **75**, 819 (2003).
- [4] I. N. Borzov, *Nuclear Physics A* **777**, 645 (2006).
- [5] J. D. Walecka, *Theoretical nuclear and subnuclear physics* (World Scientific : Imperial College Press, London, 2004).
- [6] D. Measday, *Physics Reports* **354**, 243 (2001).
- [7] A. Hayes, *Physics Reports* **315**, 257 (1999).
- [8] B. D. Serot and J. D. Walecka, *Advances in Nuclear Physics* **16**, 1 (1986).
- [9] P. Ring and P. Schuck, *The Nuclear Many-Body Problem* (Springer, Berlin, Heidelberg, New York, 1980).
- [10] S. Typel, *Physical Review C* **71**, 064301 (2005).
- [11] P. Ring, *Progress in Particle and Nuclear Physics* **37**, 193 (1996).
- [12] W. Kohn, *Reviews of Modern Physics* **71**, 1253 (1999).
- [13] G. A. Lalazissis, J. Konig, and P. Ring, *Physical Review C* **55**, 540 (1997).
- [14] F. Hofmann, C. M. Keil, and H. Lenske, *Physical Review C* **64**, 034314 (2001).
- [15] S. Typel and H. Wolter, *Nuclear Physics A* **656**, 331 (1999).
- [16] T. Nikšić, D. Vretenar, P. Finelli, and P. Ring, *Physical Review C* **66**, 024306 (2002).



- [17] G. A. Lalazissis, T. Nikšić, D. Vretenar, and P. Ring, *Physical Review C* **71**, 024312 (2005).
- [18] F. de Jong and H. Lenske, *Physical Review C* **57**, 3099 (1998).
- [19] C. J. Horowitz and B. D. Serot, *Physics Letters B* **141**, 181 (1984).
- [20] W. Kohn and L. J. Sham, *Physical Review* **140**, 1133 (1965).
- [21] R. Dreizler and E. Gross, *Density Functional Theory* (Springer, Berlin, Heidelberg, New York, 1990).
- [22] M. Bender, K. Rutz, P. Reinhard, and J. Maruhn, *European Physical Journal A* **7**, 467 (2000).
- [23] Y. Gambhir, P. Ring, and A. Thimet, *Annals of Physics* **198**, 132 (1990).
- [24] J. Dobaczewski, H. Flocard, and J. Treiner, *Nuclear Physics A* **422**, 103 (1984).
- [25] J. Dobaczewski *et al.*, *Physical Review C* **53**, 2809 (1996).
- [26] J. Valatin, *Physical Review* **122**, 1012 (1961).
- [27] T. Gonzalez-Llarena, J. Egido, G. Lalazissis, and P. Ring, *Physics Letters B* **379**, 13 (1996).
- [28] W. Pöschl, D. Vretenar, A. Rummel, and P. Ring, *Computer Physics Communications* **101**, 75 (1997).
- [29] W. Pöschl, D. Vretenar, and R. Ring, *Computer Physics Communications* **103**, 217 (1997).
- [30] H. Kucharek and P. Ring, *Zeitschrift für Physik A* **339**, 23 (1991).
- [31] J. Dechargé and D. Gogny, *Physical Review C* **21**, 1568 (1980).
- [32] H. Kucharek *et al.*, *Physics Letters B* **216**, 249 (1989).
- [33] J. Berger, M. Girod, and D. Gogny, *Nuclear Physics A* **428**, 23 (1984).
- [34] M. Serra and P. Ring, *Physical Review C* **65**, 064324 (2002).
- [35] C. Mahaux and R. Sartor, *Advances in Nuclear Physics* **20**, 1 (1986).
- [36] P.-G. Reinhard, *Nuclear Physics A* **649**, 305 (1999).
- [37] M. Jaminon and C. Mahaux, *Physical Review C* **40**, 354 (1989).
- [38] M. Jaminon and C. Mahaux, *Physical Review C* **41**, 697 (1990).

- [39] R. J. Furnstahl, J. J. Rusnak, and B. D. Serot, *Nuclear Physics A* **632**, 607 (1998).
- [40] N. Paar, T. Nikšić, D. Vretenar, and P. Ring, *Physical Review C* **69**, 054303 (2004).
- [41] *NUDAT database, available at <http://nndc.bnl.gov/nndc/nudat/>*, National Nuclear Data Center, Brookhaven National Laboratory.
- [42] V. I. Isakov *et al.*, *European Physical Journal A* **14**, 29 (2002).
- [43] S. Typel, T. v. Chossy, and H. H. Wolter, *Physical Review C* **67**, 034002 (2003).
- [44] E. Chabanat *et al.*, *Nuclear Physics A* **627**, 710 (1997).
- [45] E. Chabanat *et al.*, *Nuclear Physics A* **635**, 231 (1998).
- [46] T. Kohmura *et al.*, *Physics Letters B* **226**, 207 (1989).
- [47] D. J. Thouless, *Nuclear Physics* **22**, 78 (1961).
- [48] Z. Ma, N. V. Giai, H. Toki, and M. L’Huillier, *Physical Review C* **55**, 2385 (1997).
- [49] D. Vretenar, A. Wandelt, and P. Ring, *Physics Letters B* **487**, 334 (2000).
- [50] T. Nikšić, D. Vretenar, and P. Ring, *Physical Review C* **66**, 064302 (2002).
- [51] P. Ring *et al.*, *Nuclear Physics A* **694**, 249 (2001).
- [52] N. Paar, P. Ring, T. Nikšić, and D. Vretenar, *Physical Review C* **67**, 034312 (2003).
- [53] J. Engel *et al.*, *Physical Review C* **60**, 014302 (1999).
- [54] I. Borzov and S. Goriely, *Physical Review C* **62**, 035501 (2000).
- [55] A. Bohr and B. R. Mottelson, *Nuclear Structure* (Benjamin, New York, 1975), Vol. Vol. II.
- [56] E. J. Konopinski and M. E. Rose, in  *$\alpha$ -,  $\beta$ - and  $\gamma$ -ray spectroscopy*, edited by K. Siegbahn (North-Holland, Amsterdam, 1965).
- [57] J. N. Bahcall, *Nuclear Physics* **75**, 10 (1966).
- [58] P. T. Hosmer *et al.*, *Physical Review Letters* **94**, 112501 (2005).
- [59] I. N. Borzov, *Physical Review C* **67**, 025802 (2003).

- [60] G. Audi, O. Bersillon, J. Blachot, and A. Wapstra, *NUBASE database, available at <http://csnwww.in2p3.fr/amdc/>*, 2004.
- [61] J. D. Walecka, in *Muon Physics*, edited by V. M. Hughes and C. S. Wu (Academic Press, New York, 1975).
- [62] T. Kuramoto, M. Fukugita, Y. Kohyama, and K. Kubodera, *Nuclear Physics A* **512**, 711 (1990).
- [63] S. Weinberg, *Physical Review* **112**, 1375 (1958).
- [64] J. S. O'Connell, T. W. Donnelly, and J. D. Walecka, *Physical Review C* **6**, 719 (1972).
- [65] J. A. McNeil, R. J. Furnstahl, E. Rost, and J. R. Shepard, *Physical Review C* **40**, 399 (1989).
- [66] C. deBoor, *A Practical Guide to Splines* (Springer, New York, 1978).
- [67] C. Piller *et al.*, *Physical Review C* **42**, 182 (1990).
- [68] P. Bergem *et al.*, *Physical Review C* **37**, 2821 (1988).
- [69] N. T. Zinner, K. Langanke, and P. Vogel, *Physical Review C* **74**, 024326 (2006).
- [70] T. Marketin, D. Vretenar, and P. Ring, *Physical Review C* **75**, 024304 (2007).
- [71] T. Suzuki, D. F. Measday, and J. P. Roalsvig, *Physical Review C* **35**, 2212 (1987).
- [72] H. Fynbo *et al.*, *Nuclear Physics A* **724**, 493 (2003).
- [73] T. N. Mamedov *et al.*, *JETP Letters* **71**, 451 (2000).
- [74] H. Hanscheid *et al.*, *Zeitschrift fr Physik A* **335**, 1 (1990).
- [75] P. David *et al.*, *Zeitschrift fr Physik A* **330**, 397 (1988).
- [76] H. Primakoff, *Reviews of Modern Physics* **31**, 802 (1959).
- [77] C. Athanassopoulos *et al.*, *Physical Review C* **55**, 2078 (1997).
- [78] B. Bodmann *et al.*, *Physics Letters B* **280**, 298 (1992).
- [79] R. Maschuw, *Progress in Particle and Nuclear Physics* **40**, 183 (1998).
- [80] D. D. Koetke *et al.*, *Physical Review C* **46**, 2554 (1992).

- [81] D. A. Krakauer *et al.*, *Physical Review C* **45**, 2450 (1992).
- [82] C. Volpe *et al.*, *Physical Review C* **62**, 015501 (2000).
- [83] E. Kolbe, K. Langanke, G. Martínez-Pinedo, and P. Vogel, *Journal of Physics G: Nuclear and Particle Physics* **29**, 2569 (2003).
- [84] J. Engel, *Physical Review C* **57**, 2004 (1998).
- [85] A. Aste and D. Trautmann, *European Physical Journal A* **33**, 11 (2007).
- [86] C. Athanassopoulos *et al.*, *Physical Review Letters* **81**, 1774 (1998).
- [87] R. Lazauskas and C. Volpe, *Nuclear Physics A* **792**, 219 (2007).
- [88] E. Kolbe and K. Langanke, *Physical Review C* **63**, 025802 (2001).
- [89] N. Auerbach and B. A. Brown, *Physical Review C* **65**, 024322 (2002).
- [90] S. L. Mintz, *Journal of Physics G: Nuclear and Particle Physics* **28**, 451 (2002).
- [91] T. Suzuki and H. Sagawa, *Nuclear Physics A* **718**, 446 (2003).
- [92] T. Suzuki *et al.*, *Physical Review C* **79**, 061603R (2009).
- [93] M. S. Athar, S. Ahmad, and S. Singh, *Nuclear Physics A* **764**, 551 (2006).
- [94] N. Auerbach, N. Van Giai, and O. K. Vorov, *Physical Review C* **56**, R2368 (1997).
- [95] C. Volpe, N. Auerbach, G. Colo, and N. V. Giai, *Physical Review C* **65**, 044603 (2002).
- [96] E. Kolbe, K. Langanke, and G. Martínez-Pinedo, *Physical Review C* **60**, 052801 (1999).
- [97] E. Kolbe, K. Langanke, and K. Riisager, *European Physical Journal A* **11**, 39 (2001).
- [98] S. E. Woosley, D. H. Hartmann, R. D. Hoffman, and W. C. Haxton, *Astrophysical Journal* **356**, 272 (1990).
- [99] G. M. Fuller, W. C. Haxton, and G. C. McLaughlin, *Physical Review D* **59**, 085005 (1999).
- [100] I. N. Borzov, *Nuclear Physics A* **718**, 635 (2003).
- [101] W. Johnson, S. Blundell, and J. Sapirstein, *Physical Review A* **37**, 307 (1988).



# List of Figures

|     |   |    |
|-----|---|----|
| 2.1 | Radial dependence of the spin-orbit potential in the self-consistent solution for the ground-state of $^{132}\text{Sn}$ . Full line corresponds to the potential obtained with the DD-ME1 interaction, while others are obtained with the DD-ME1* interaction. First and second term correspond to the first and second term of the potential in (2.91). . . . .  | 37 |
| 2.2 | Neutron (left panel) and proton (right panel) single-particle energies for doubly-closed nucleus $^{132}\text{Sn}$ . Plotted in the first column denoted with (a) are states calculated with the DD-ME1 interaction, DD-ME1* (b) and compared to the experimental values in the last column (c). Experimental data is taken from [42]. . . . .  | 39 |
| 2.3 | Neutron (left panel) and proton (right panel) single-particle energies for doubly-closed nucleus $^{132}\text{Sn}$ . Plotted in the first column denoted with (a) are states calculated with the DD-ME1 interaction, D <sup>3</sup> C (b) and D <sup>3</sup> C* (c) and compared to the experimental values in the last column (d). Experimental data is taken from [42]. . . . .   | 41 |
| 3.1 | Half-lives of iron isotopes calculated with various interactions. Open symbols denote values obtained without $T = 0$ residual interaction, while full symbols denote values with additional interaction. Strength of the residual pairing is $V_0 = 115$ MeV for the DD-ME1* interaction, and $V_0 = 125$ MeV for the momentum-dependent D3C* interaction. Theoretical results are compared to experimental values taken from Ref. [60]. . . . . | 57 |
| 3.2 | Half-lives of nickel isotopes calculated with various interactions. Experimental values taken from Ref. [60], except for $^{78}\text{Ni}$ which is taken from Ref. [58]. . . . .  | 59 |

|     |   |    |
|-----|---|----|
| 3.3 | Half-lives of zinc isotopes calculated with various interactions. Open symbols denote values obtained without $T = 0$ residual interaction, while full symbols denote values with additional interaction. Strength of the residual pairing is $V_0 = 330$ MeV for the DD-ME1* interaction, and $V_0 = 300$ MeV for the momentum-dependent D3C* interaction. Experimental values taken from Ref. [60]. No experimental value is available for $^{82}\text{Zn}$ , so an empirical value was used. . . . . | 62 |
| 3.4 | Half-lives of cadmium isotopes calculated with various interactions. Open symbols denote values obtained without $T = 0$ residual interaction, while full symbols denote values with additional interaction. Strength of the residual pairing is $V_0 = 225$ MeV for the DD-ME1* interaction, and $V_0 = 235$ MeV for the momentum-dependent D3C* interaction. Experimental values taken from Ref. [60]. . . . .  | 63 |
| 3.5 | Half-lives of tin isotopes calculated with various interactions. Open symbols denote values obtained without $T = 0$ residual interaction, while full symbols denote values with additional interaction. Strength of the residual pairing is $V_0 = 225$ MeV for the DD-ME1* interaction, and $V_0 = 235$ MeV for the momentum-dependent D3C* interaction. Experimental values taken from Ref. [60]. . . . .  | 64 |
| 3.6 | Half-lives of tellurium isotopes calculated with various interactions. Open symbols denote values obtained without $T = 0$ residual interaction, while full symbols denote values with additional interaction. Strength of the residual pairing is $V_0 = 225$ MeV for the DD-ME1* interaction, and $V_0 = 235$ MeV for the momentum-dependent D3C* interaction. Experimental values taken from Ref. [60]. . . . .  | 65 |
| 4.1 | Square of the wave function of a muon in a $1s$ state for $^{16}\text{O}$ , $^{40}\text{Ca}$ , $^{120}\text{Sn}$ and $^{208}\text{Pb}$ . Dashed lines denote wave functions of a muon in a potential of pointlike charge $Z$ , while the full line denotes wave functions obtained by performing the full finite element method calculation for the self-consistent Coulomb potential. Shaded area indicates charge density distribution in a particular nucleus scaled by an arbitrary factor. . . . . | 76 |
| 4.2 | Ratio of the calculated and experimental total muon capture rates, as function of the proton number $Z$ . The theoretical values are calculated with muon $1s$ wave functions determined by self-consistent ground-state charge densities (filled circle symbols), and by the corresponding point-charge Coulomb potentials (squares). . . . .  | 78 |

|      |   |    |
|------|---|----|
| 4.3  | Ratio of the calculated and experimental total muon capture rates, as function of the proton number $Z$ . Circles correspond to rates calculated with the free-nucleon weak form factors [62], and diamonds denote values obtained by quenching the free-nucleon axial-vector coupling constant $g_A = 1.262$ to $g_A = 1.135$ for all operators, i.e. in all multipole channels. . . . .           | 79 |
| 4.4  | Relative contributions of different multipole transitions to the RHB plus RQRPA total muon capture rates in $^{16}\text{O}$ , $^{40}\text{Ca}$ , $^{120}\text{Sn}$ and $^{208}\text{Pb}$ . . . . .  | 80 |
| 4.5  | Total muon capture rates on Ca, Cr and Ni isotopes. Experimental rates (filled symbols) are compared to theoretical values (empty symbols), calculated using the fully consistent RHB plus RQRPA framework with the DD-ME2 universal effective interaction, and with the quenching of the axial-vector coupling constant $g_A = 1.262 \rightarrow g_A = 1.135$ for all multipole operators. . . . . | 83 |
| 4.6  | Inclusive cross sections for the $^{16}\text{O}(\nu_e, e^-)^{16}\text{F}$ , $^{56}\text{Fe}(\nu_e, e^-)^{56}\text{Co}$ , and $^{208}\text{Pb}(\nu_e, e^-)^{208}\text{Bi}$ reactions. The RHB plus PN-RQRPA(DD-ME2) results are compared with those obtained in the QRPA with the Skyrme interaction SIII [87] (full symbols) and with a hybrid model [88] (open symbols). . . . .                   | 85 |
| 4.7  | Inclusive cross sections for the $^{56}\text{Fe}(\nu_e, e^-)^{56}\text{Co}$ reaction. Positive parity multipoles are denoted by full lines, while negative parity transitions are denoted by dashed lines. . . . .  | 87 |
| 4.8  | Supernova neutrino fluxes for temperatures ranging from $T = 4$ MeV to $T = 10$ MeV, $\alpha = 0$ . . . . .   | 89 |
| 4.9  | Inclusive cross section for the $^{56}\text{Fe}(\nu_e, e^-)^{56}\text{Co}$ reaction, averaged over the supernova neutrino flux and plotted as a function of temperature. The pn-RQRPA results obtained with the DD-ME2 effective interaction are compared with the shell model cross sections from Refs. [88, 92, 98]. . . . .  | 90 |
| 4.10 | Inclusive cross section for the $^{56}\text{Fe}(\nu_e, e^-)^{56}\text{Co}$ reaction, averaged over the supernova neutrino flux and plotted as a function of temperature. The pn-RQRPA results obtained with the DD-ME2 effective interaction are compared with the shell model cross sections from Refs. [88, 95, 99]. . . . .  | 91 |





# List of Tables

|     |   |    |
|-----|---|----|
| 2.1 | Values of the parameters of the D1S Gogny pairing interaction.  | 33 |
| 2.2 | Energy separation (in MeV) between spin-orbit partner states in doubly closed-shell nuclei, calculated with the DD-ME1 and DD-ME1* interactions, and compared with experimental data [41].  | 38 |
| 2.3 | Properties of symmetric nuclear matter at saturation density calculated with the models DD-ME1, D <sup>3</sup> C, and D <sup>3</sup> C*. . . . .  | 40 |
| 3.1 | Occupation probabilities of neutron and proton single-particle states for the ground-states of <sup>76</sup> Fe and <sup>80</sup> Zn. . . . .   | 58 |
| 3.2 | $\beta^-$ -transitions in <sup>80</sup> Zn for three values of the $T = 0$ pairing strength. The contribution (in percent) of a particular configuration to the QRPA amplitude is included in parenthesis. . . . .  | 61 |
| 3.3 | Occupation probabilities of the $\nu 1h_{9/2}$ single-particle state for the ground-states of the Sn and Te isotopes. . . . .   | 64 |
| 4.1 | Lepton traces obtained from lepton matrix elements $l_\mu$ . . . . .  | 73 |
| 4.2 | Sign factors for weak processes used in Table 4.1. . . . .  | 73 |
| 4.3 | Calculated muon transition energies in tin isotopes (in units of keV), compared with available data [67]. . . . .   | 77 |
| 4.4 | Calculated muon transition energies in <sup>208</sup> Pb (in units of keV), in comparison with experimental values [68]. . . . .  | 77 |
| 4.5 | Experimental and calculated muon capture rates for natural elements and individual isotopes. The theoretical rates are calculated using the fully consistent RHB plus RQRPA framework with the DD-ME2 universal effective interaction, and with the quenching of the axial-vector coupling constant $g_A = 1.262 \rightarrow g_A = 1.135$ for all multipole operators. Values for naturally occurring elements (element symbol with no superscript) are weighted averages of capture rates on individual isotopes, using their natural abundances. Experimental values are from Ref. [71], unless otherwise stated. All rates are in units of $10^6 \text{ s}^{-1}$ . | 82 |

|     |  |    |
|-----|--|----|
| 4.6 | Flux-averaged cross sections for the $\nu_e$ reaction on $^{16}\text{O}$ , $^{56}\text{Fe}$ , and $^{208}\text{Pb}$ target nuclei. Values denoted with $^a$ were obtained without any quenching of the axial-vector coupling constant ( $g_A = -1.262$ ), while values denoted with $^b$ were obtained using a quenching factor of $Q = 0.8$ ( $g_A = -1.0$ ). . . . . | 86 |
| 4.7 | Flux-averaged cross sections of each multipole transition for the $^{56}\text{Fe} (\nu_e, e^-) ^{56}\text{Co}$ reaction compared to a hybrid shell model + CRPA calculation. Averaged cross sections were obtained using a quenching factor of $Q = 0.8$ ( $g_A = -1.0$ ). All cross sections given in units of $10^{-42} \text{ cm}^2$ . . . . .                      | 88 |

# Curriculum Vitae

**Date of birth:** 21. 7. 1980., Zagreb

**Address:** Department of Physics, Faculty of Science, University of Zagreb

**Tel.:** ++385 1 460 5663

**E-mail:** marketin@phy.hr

## Education:

**March 2005.** - PhD student, Physics department, Faculty of Science, University of Zagreb

**September 2004.** B. Sc. in physics with the thesis  *$\beta^-$ -decay in exotic nuclei in the relativistic quasiparticle random phase approximation*, supervised by Prof. Dario Vretenar

**1998.-2004.** Faculty of Science, University of Zagreb

**1994.-1998.** XV. Gymnasium, Zagreb

**1986.-1994.** Elementary school Vladimir Nazor, Zagreb

## International experience:

**June 2010.** participant of the Second EMMI-EFES workshop on neutron-rich exotic nuclei, Tokyo, Japan

**April - June 2010.** participant of the Doctoral Training Programme at the European centre for theoretical studies in nuclear physics and related areas, Trento, Italy

**May 2009.** participant of the Nuclear structure and dynamics conference, Dubrovnik, Croatia

**March 2009.** participant of the Joint Spring Meeting of the DPG division Hadronic and Nuclear Physics and the Nuclear Physics Board of the European Physical Society (EPS), Bochum, Germany

**October 2007.** participant of Exotic Modes of Excitation: from Nuclear Structure to Astrophysics conference at ECT\*, Trento, Italy

**August 2007.** participant of JINR summer school, Dubna, Russia

**March - June 2007.** participant of the Doctoral Training Programme at the European centre for theoretical studies in nuclear physics and related areas, Trento, Italy

**May - September 2006.** visiting researcher at the Technische Universität München

## Publications

1. P. Ring, T. Marketin, N. Paar and D. Vretenar, *Covariant density functional theory: inclusive charged current neutrino-nucleus reactions*, Acta Phys. Pol. B 40, 2537 (2009).
2. T. Marketin, N. Paar, T. Nikšić and D. Vretenar, *Relativistic quasiparticle random-phase approximation calculation of total muon capture rates*, Phys. Rev. C 79, 054323 (2009).
3. N. Paar, D. Vretenar, T. Marketin and P. Ring, *Inclusive charged-current neutrino-nucleus reactions calculated with the relativistic quasiparticle random-phase approximation*, Phys. Rev. C 77, 024608 (2008)
4. D. Vretenar, N. Paar, T. Marketin and P. Ring, *Relativistic QRPA description of nuclear excitations*, J. Phys. G: Nucl. Part. Phys 35, 014039 (2008)
5. T. Marketin, D. Vretenar and P. Ring, *Calculation of  $\beta$ -decay rates in a relativistic model with momentum-dependent self-energies*, Phys. Rev. C 75, 024304 (2007)
6. N. Paar, T. Nikšić, T. Marketin, D. Vretenar and P. Ring, *Self-consistent relativistic QRPA studies of soft modes and spin-isospin resonances in unstable nuclei*, Eur. Phys. J. A25, 531 (2005)
7. T. Nikšić, T. Marketin, D. Vretenar, N. Paar and P. Ring, *Beta-decay rates of  $r$ -process nuclei in the relativistic quasiparticle random phase approximation*, Phys. Rev. C 71, 014308 (2005)

## Conference Proceedings

1. T. Marketin, N. Paar, T. Nikšić, D. Vretenar and P. Ring, *Relativistic QRPA calculation of beta-decay rates of  $r$ -process nuclei*, AIP Conference Proceedings 1165, 433 (2009).
2. D. Vretenar, N. Paar and T. Marketin, *Relativistic energy density functionals: exotic modes of excitation*, AIP Conference Proceedings 1072, 70 (2008).

3. N. Paar, T. Marketin, D. Vretenar and P. Ring, *Consistent approach to weak interaction rates based on the relativistic QRPA*, Proceedings of Science(NICX), 030 (2008).
4. N. Paar, D. Vretenar, T. Marketin and P. Ring, *Neutrino-nucleus reaction rates based on the relativistic quasiparticle random phase approximation*, FRONTIERS IN NUCLEAR STRUCTURE, ASTROPHYSICS, AND REACTIONS: FINUSTAR 2, AIP Conference Proceedings 1012, 46 (2008).